MULTIPHOTON IONISATION SPECTROSCOPY OF Cl_2 AND I_2 VIA REPULSIVE INTERMEDIATE STATES

By
Mohamed S. H. N. Al-Kahali

DOCTOR OF PHILOSOPHY
THE UNIVERSITY OF EDINBURGH
March 1996

Declaration

I declare that this thesis has been composed by me and that the work described in it is my own, except where due acknowledgement is made, and was carried out whilst a member of the laser group at the University of Edinburgh.

Signed: [redacted]

Date: 6 - 5 - 1996

Here comes the light

To Mona,

the most precious

Acknowlegements

Firstly, I would like to thank my two supervisors Professor Robert Donovan and Dr Trevor Ridley for their advice and encouragement throughout the three and half years that I have spent studying and researching at Edinburgh. I am greatly indebted to Trevor for his assistance in the lab and the valuable discussions in analysing the results. I also would like to thank Dr Kenneth Lawley for his advice and for the computer programmes used in analying the results in this work. Also I would like to thank Robert Maier for any assistance that he provided in the lab.

I would like to thank my parents, who supported me financially throughout the years that I have spent in this country. I would like to thank the Ministry of Higher Education and Scientific Research, Republic of Yemen, for awarding me the two years scholarship.

The laser group has been an excellent enviroment to work with, and I have enjoyed working with them all, my sincere thanks to them all past and present, especially A.J.Yarwood, P.Wilson, J.Goode, I.Borthwick, I.Mowat, Z.Min, S.Flexen, J.Hennessy. I would like to thank the coffee break mates Sandy, Martin, Mike, Paul and John.

I have enjoyed my stay in Edinburgh and I have made many friends in the social events that I have been to. Thanks to all of them especially Bassam, Ahmed, La'aiche, Mariso, and Iymen. Also not to forget my flatmates, Hans and Chan.

Finally, I would like to thank the technical and secretarial staff, especially Margaret Stewart.

Abstract

The use of mass-resolved resonance enhanced multiphoton ionisation techniques, to study the ion-pair and Rydberg states of jet-cooled I_2 and Cl_2, is described. Repulsive intermediate states are used to access the ion-pair states and this is shown to enlarge the Franck-Condon window from the ground state. It was found that when the Mulliken difference potential exhibits a maximum, known as the red extremum, excitation at or near the extremum greatly enhances the transition probability.

Large bond extensions $\sim$ 1 Å are reported in one-colour two-photon optical excitation of I_2, *via* the continuum of the intermediate $B0_u^+$ state, in the energy region 45147-47733 cm^{-1}. The $E0_g^+$ state is accessed in the sequence $E0_{g\,(v'=40-70)}^+ \leftarrow B0_u^+ \leftarrow X0_g^+$, with the laser wavelength scanned near the prominent red extremum of the E$\rightarrow$B emission system. The relatively short spectrum was attributed to the limitation of the B$\leftarrow$X absorption cross section, at shorter wavelengths, and the limit of the red extremum, at longer wavelengths.

Similarly, one-colour, three-photon (1+2) excitation *via* the continuum of the $B0_u^+$ state of Cl_2 is used to access the low vibrational levels of the $D0_u^+(^3P_2)$, and $F0_u^+(^3P_0)$ ion-pair states, in the energy region 59000-72000 cm^{-1}. The $F'0_u^+(^1D_2)$ ion-pair state is seen only when interacting with the $F0_u^+(^3P_0)$ state, due to perturbations. Weak interactions between the $D0_u^+(^3P_2)$ and $F0_u^+(^3P_0)$ ion-pair states are also reported.

In the one-colour, two-photon, (1+1) excitation of Cl_2, *via* the repulsive $C1_u$ state, an extension of the $[^2\Pi_{1/2}]_c$ 4s;1_g Rydberg state (v'=0-19) was observed. Also, a long progression in the $\beta 1_g$ ion-pair state (v'=65-166) is reported. The vibrational envelope of the $\beta 1_g$ ion-pair state was attributed to the C$\leftarrow$X absorption limit, at shorter wavelengths, and the red extremum limit of the $\beta \rightarrow$C emission

system, at longer wavelengths. The lower vibrational levels of the $\beta 1_g$ ion-pair state were accessed, using two-colour excitation, *via* the $C1_u$ state.

In a one-colour (2+1) REMPI excitation spectrum of Cl_2, between 75000-90000 cm^{-1}, a total of twenty two Rydberg states were observed. These are based on the $[^2\Pi_{3/2}]_c$ and $[^2\Pi_{1/2}]_c$ cores of the ion, to which they converge. Vibrational levels up to $v' = 4$ were observed in each Rydberg state, which is typical of vertical excitation (i.e where no intermediate state is involved). Between 76500-80000 cm^{-1} homogeneous interactions between both the $[^2\Pi_{3/2}]_c$ 3d;1_g and $[^2\Pi_{1/2}]_c$ 3d;1_g Rydberg states, and the $\beta 1_g$ ion-pair state, have been observed.

Vibronic coupling between the $[^2\Pi_{3/2}]_c$ 7s;1_g Rydberg state and the $\beta 1_g$ ion-pair state of I_2, in the energy region 62500-64500 cm^{-1}, has also been investigated.

Table of Contents

List of Figures

List of Tables

Chapter 1

Introduction

1.1 Introduction

In optical spectroscopy, the observation and characterisation of electronic states in molecules generally depends on the feasibility of vertical transitions from the ground electronic state to the upper electronic states. The Franck-Condon factors dictate the regions of the upper electronic state potential that can be accessed from $v'' = 0$ of the ground state. In halogen and interhalogen molecules the ion-pair states have R_e values which are relatively large compared to the ground state: e.g. in molecular I_2, R_e values for the $E0_g^+$ ion-pair state, and $X0_g^+$ ground state, are 3.6 Å and 2.6 Å respectively. Therefore, vertical transitions from $v''= 0$ of the ground state can only access the inner wall of the ion-pair state potential a few thousand wavenumbers above T_e. To be able to access vibrational levels of the ion-pair states at or near their electronic minima, the well documented two-photon optical-optical double resonance (OODR) technique is used, in which one photon, $h\nu_1$, excites the molecule from the $v''= 0$ of the ground state to the inner wall of a bound intermediate valence state, and a second photon, $h\nu_2$, further excites the molecule from the outer wall of the intermediate state to the low vibrational levels of the ion-pair state.

In the work described in this thesis a novel technique was used, in which the intermediate state was a continuum state, (i.e. the repulsive wall of a bound intermediate state, or a purely repulsive intermediate valence state). In either case, the red extremum of the final $\rightarrow$ intermediate emission system was exploited. Thus, the laser wavelength was scanned, near or to the blue of the red extremum region. The use of continuum intermediate states will revolutionise the OODR technique, since most excited valence states of molecules are repulsive (in the Franck-Condon region spanned by $v'' = 0$) or, if bound, are predissociated.

To start with, a background on the electronic structure of halogens, together

with the electronic states of molecular I_2 and Cl_2, and the relevant principles and theories, which are of importance to the work done in this thesis, will be discussed.

1.2 The Electronic Structure in Diatomic Halogens

The electronically excited states of diatomic halogens can be described in terms of their molecular orbital (MO) configuration. The molecular orbitals are formed from the Linear Combination of Atomic Orbitals (LCAO approximation). In this case ten valence electrons, five from each halogen atom (outer p-orbitals), are distributed among the four highest molecular orbitals, $\sigma_g \pi_u \pi_g \sigma_u$. In homonuclear halogens, the orbitals from each atom are degenerate and contribute equally to the molecular orbitals (see Figure (1.1)). In heteronuclear halogens, atomic orbitals are no longer degenerate, hence the MO are dominated by one of the atomic orbital contributors, (the g/u symmetry does not apply in this case). Normally, the description of the electronic state configuration is based on how the valence electrons occupy the four highest molecular orbitals. For instance the ground state configuration can be written as $\sigma_g^2 \pi_u^4 \pi_g^4 \sigma_u^0$, or simply 2440 for abbreviation.

The lower excited states are arranged in accordance with the dissociation products with which they correlate. Valence states correlate to a dissociation with two ground state or spin-orbit excited $X(^2P_J)$ atoms, while the Rydberg states dissociate to one ground state atom and one excited atom $X+X^*$. Ion-pair states dissociate to an anion X^- and a cation X^+. This is illustrated in Figure (1.2), using the electronic states of I_2.

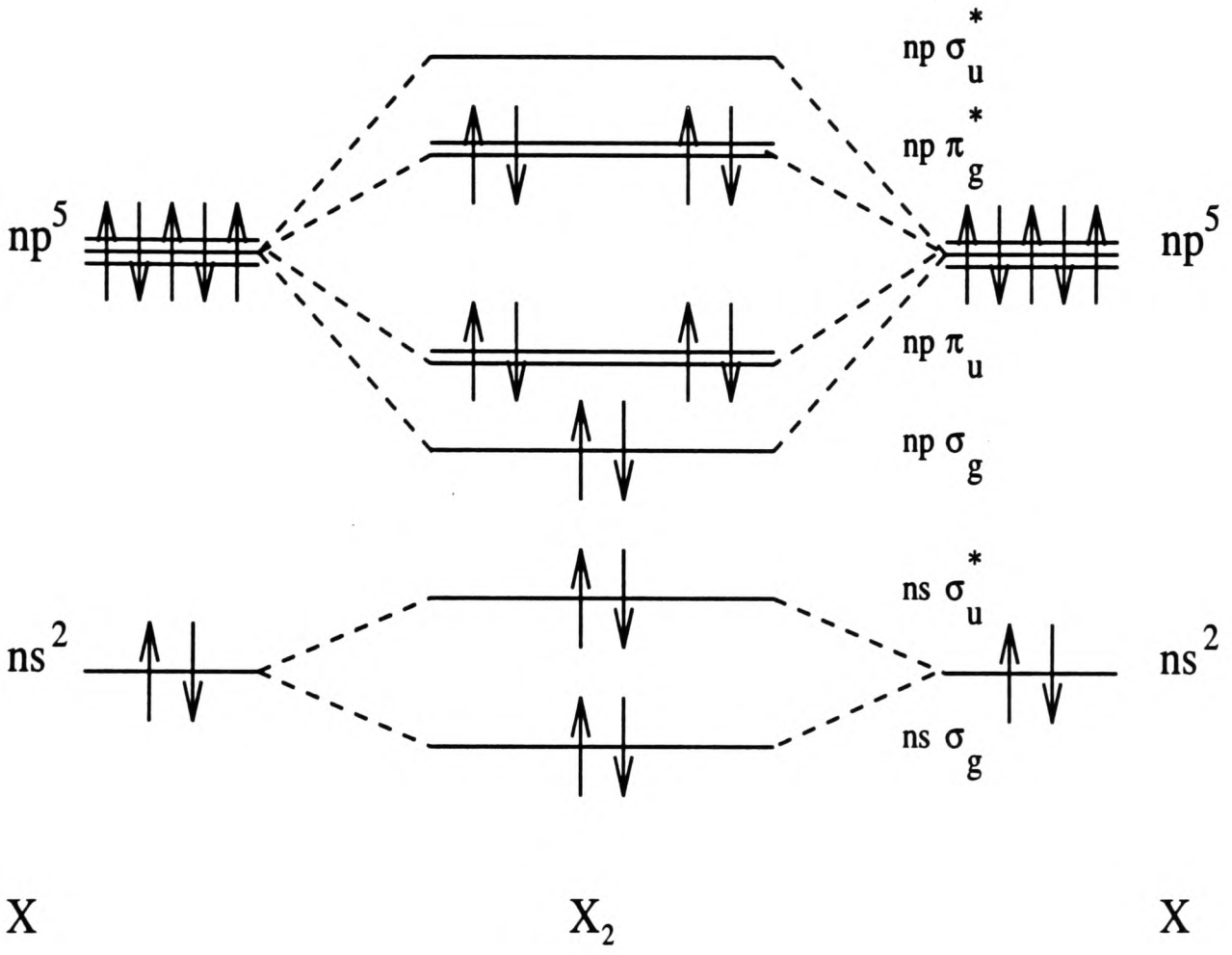

X = F : n = 2
X = Cl : n = 3
X = Br : n = 4
X = I : n = 5

Figure 1–1: Schematic LCAO-MO representation in halogens diatomics.

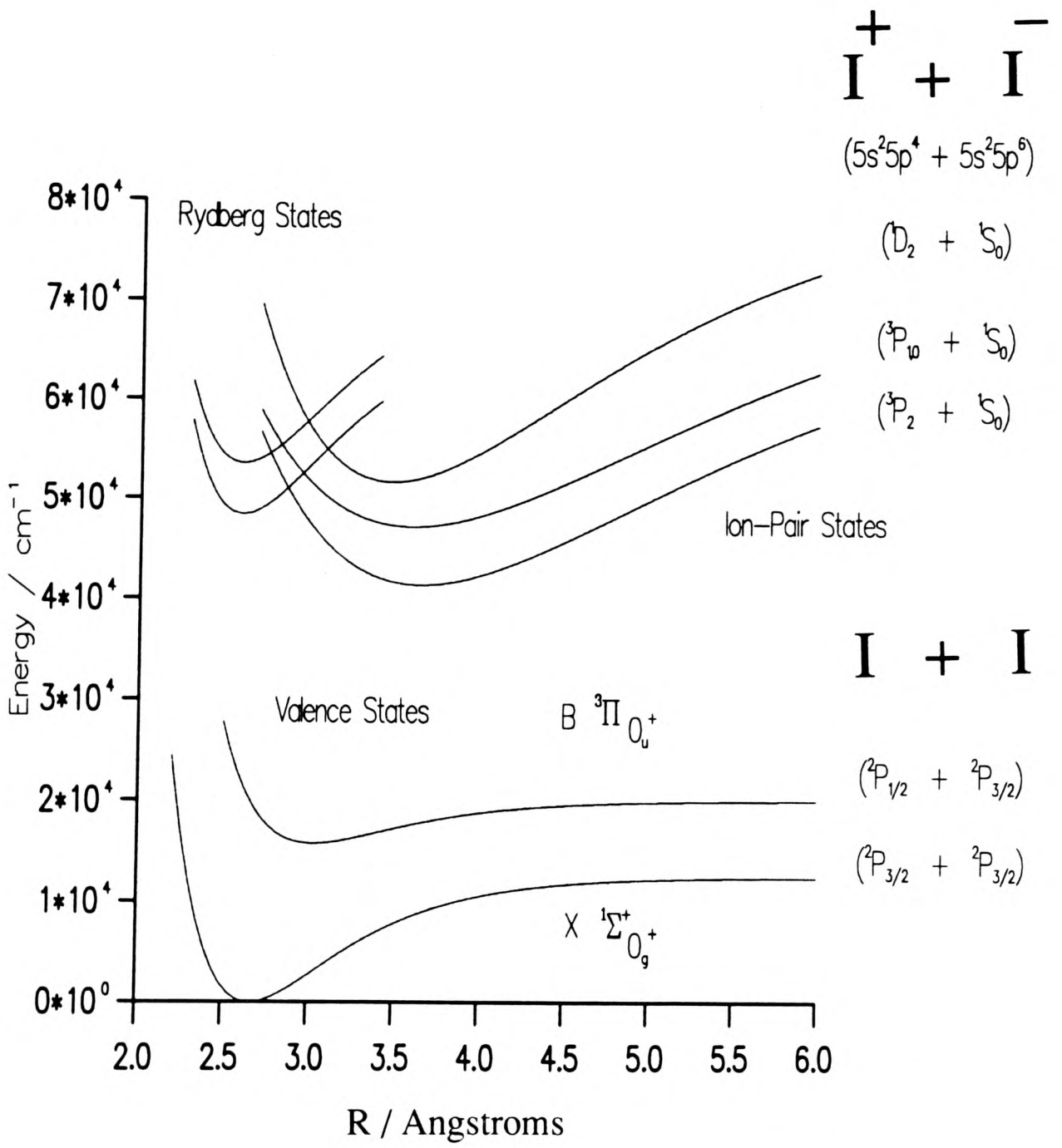

Figure 1–2: Schematic diagram of the electronic states of I_2.

1.3 Ion-Pair States

An ion-pair state of a molecule is one in which bond-breaking produces a pair of oppositely charged ions rather than two neutral fragments. The ion-pair states of the halogens are organised in clusters, or tiers, as predicted by Mulliken [1]. The energy separation of these tiers is approximately equal to the separation between the states of the p^4 configuration of the atomic positive ion. The ion-pair states are grouped into three tiers of six ion-pair states each correlating with $X^+(^3P_2)$, $X^+(^3P_{1,0})$ and $X^+(^1D_2)$. Two states lying in the fourth tier, at higher energies, correlate with $X^+(^1S_0)$, giving twenty ion-pair states in total.

The potential curves of the ion-pair states are dominated by the long range Coulombic attraction, $-e^2/r$(C_1, in equation 1.1), between the ions, resulting in deeply bound states with long range attractive branches and wide vibrational amplitudes. The truncated Rittner potential [2], equation 1.1, is used to model the interaction between the anion (X^-) and the cation (X^+);

$$V(R) = T_\infty + Aexp(-br) - C_1/R - C_4/R^4 - C_6/R^6 \qquad (1.1)$$

where R is the interionic distance, T_∞ is the ion-pair dissociation limit, and C_1, C_4 and C_6 are coefficients of charge-charge, charge-polarisation and induced dipole-induced dipole interactions, respectively . The A exp(-br) term describes the repulsive limb of the potential [3].

1.3.1 The Ion-Pair States of I_2

The ion-pair states of I_2 have been studied extensively and 13 ion-pair states have been identified, correlating with $I^-(^1S) + I^+(^3P_{2,0,1},^1D_2)$ dissociation products. A model of their electronic structure is as follows, the six states $D'2_g$, $\beta 1_g$, $E0_g^+$, $D0_u^+$,

$\gamma 1_u$ and $\delta 2_u$, which belong to the lowest group correlating with $I^-(^1S_0)$+$I^+(^3P_2)$ are located around 40000 cm^{-1} above the ground state. The six states, $f0_g^+$, $g0_g^-$, $F0_u^+$, $G1_g$, 0_u^-, and H_{1u}, correlating with $I^-(^1S_0) + I^+(^3P_1, ^3P_0)$ are located around 47000 cm^{-1}. The third cluster correlating with $I^-(^1S_0) + I^+(^1D_2)$, should lie about 7000 cm^{-1} higher up than the second cluster. Two ion-pair states were observed in this cluster, the $F'\ 0_u^+$ and $f'0_g^+$ states (see Table (1.1)). Typical R_e and ω_e (vibrational spacing) values are 3.6 Å and 100 ± 5 cm^{-1}, respectively, with the exception of the $F'0_u^+$ state which has an ω_e value of 131 cm^{-1} and R_e of 3.48 Å. Typical D_e values are around 30000 cm^{-1}.

1.3.2 The Ion-Pair States of Cl_2

In a diabatic approximation the ion-pair states of Cl_2 correlate at the dissociation limit with the ionic products Cl^- + Cl^+. The energies of Cl^+ in the lowest ionic asymptote $Cl^-(^1S_0)$ + $Cl^+(^3P)$ are in the order $^3P_2$(ground state), $^3P_1$(697 cm^{-1}) and $^3P_0$(996 cm^{-1}). On this basis, the $Cl^+(^3P_2)$ correlates to Ω=0^+,1 and 2 states, $Cl^+(^3P_1)$ correlates to Ω=0^- and 1, and $Cl^+(^3P_0)$ correlates to Ω=0^+ [23]. The $^3P_2$ - $^1D_2$ splitting is $\sim$ 11000 cm^{-1}, hence ion-pair states that dissociate to $Cl^-(^1S_0)$ + $Cl^+(^1D_2)$, should lie approximately 11000 cm^{-1} above the ion-pair states that dissociate to $Cl^-(^1S_0)$ + $Cl^+(^3P_2)$. Because the splitting energies between the $^3P_2$-$^3P_1$ and $^3P_1$-$^3P_0$ are significantly smaller compared to the splittings in the I_2 molecule, the 12 states correlating to the $^3P_2$, $^3P_1$ and $^3P_0$ ionic products are expected to be closely spaced in essentially one cluster. The known ion-pair states of Cl_2 are listed in table (1.2).

State	T_e/cm^{-1}	ω_e/cm^{-1}	R_e Å	Diss.Limit	Ref.
$f'0_g^+$	55409.9	97.1	3.825	$^1D_2+^1S_0$	7
$F'0_u^+$	51706.2	131.0	3.48	$^1D_2+^1S_0$	5 & 6
$H1_u$	48280.3	107.7	3.63	$^3P_1+^1S_0$	8
$G1_g$	47559.1	106.6	3.528	$^3P_1+^1S_0$	9
$F0_u^+$	47217.35	96.3	3.60	$^3P_0+^1S_0$	10 & 11
$g0_g^-$	(47070)	(105.7)	(3.55)	$^3P_1+^1S_0$	12
$f0_g^+$	47025.9	104.2	3.57	$^3P_0+^1S_0$	13 & 14
$\delta 2_u$	41689	100.2	(4.0)	$^3P_2+^1S_0$	15
$\gamma 1_u$	41621.3	95.0	3.67	$^3P_2+^1S_0$	15
$E0_g^+$	41411.8	101.4	3.65	$^3P_2+^1S_0$	16
$D0_u^+$	41028.6	95.0	3.58	$^3P_2+^1S_0$	17 & 18
$\beta 1_g$	40821.0	105.0	3.61	$^3P_2+^1S_0$	19
$D'2_g$	40388.2	103.9	3.59	$^3P_2+^1S_0$	20 & 21 & 22

Table 1–1: Known spectroscopic constants of ion-pair states of I_2.

T_e is the equilibrium term value.

ω_e is the vibrational frequency.

R_e is the equilibrium internuclear separation.

D_e is the dissociation energy.

State	$\mathbf{T_e/cm^{-1}}$	$\omega_e/\mathbf{cm^{-1}}$	$\mathbf{R_e}$ **Å**	**Diss.Limit**	**Ref.**
1_g	68446.3	256.7	2.85	$^1D_2+^1S_0$	24 & 25
$F'0_u^+$	(64631)	(261)	(2.57)	$^1D_2+^1S_0$	26
$F0_u^+$	59932.0	284.0	3.02	$^3P_0+^1S_0$	27
0_u^-	(59740.0)	-	-	$^3P_1+^1S_0$	28
$H1_u$	(59540.0)	-	-	$^3P_1+^1S_0$	28
$f0_g^+$	59356.1	257.0	2.90	$^3P_0+^1S_0$	29
$G1_g$	59295.7	256.6	2.90	$^3P_1+^1S_0$	30
$g0_g^-$	57978.8	252.4	2.87	$^3P_1+^1S_0$	32
$\delta 2_u$	59056.1	248.6	3.05	$^3P_2+^1S_0$	28
$\gamma 1_u$	58537.2	239.7	2.84	$^3P_2+^1S_0$	28
$D0_u^+$	58486.1	235.7	2.84	$^3P_2+^1S_0$	28
$E0_g^+$	57819.4	252.0	2.88	$^3P_2+^1S_0$	31
$\beta 1_g$	57572.2	252.0	2.88	$^3P_2+^1S_0$	33
$D'2_g$	57295.7	252.3	2.87	$^3P_2+^1S_0$	34 & 35

Table 1–2: Known spectroscopic constants of ion-pair states of Cl_2.

1.4 Rydberg States

Rydberg states can be best described as those which involve the promotion of an electron, usually of non-bonding or weakly antibonding/bonding character in molecular systems, to orbitals of higher principal quantum number, n. Excitation of the electron to progressively higher n constitutes a Rydberg series and as n$\rightarrow \infty$ the series converges to the limit of the molecular ion core, corresponding to the removal of the Rydberg electron. Rydberg states with different principal quantum numbers but the same l value belong to the same series. The Rydberg formula which describes a Rydberg state is as follows;

$$E_{obs} = IP - R/(n-\delta)^2 \tag{1.2}$$

Where IP is the ionisation potential to which the Rydberg series converge, n is the principal quantum number of the Rydberg orbital, R is the Rydberg constant (109737.1 cm^{-1}), and δ is the quantum defect associated with the Rydberg electron. The effective quantum number (n-δ) is normally used to describe the type of orbitals involved. The quantum defect δ, is in effect a shielding coefficient, because the Rydberg electron is shielded from the ionic core by the valence electrons.

The potential energy curve of a halogen Rydberg state is similar to that of the ground state. More precisely the removal of an electron from a weakly antibonding to a (non-bonding) Rydberg orbital, gives them more bonding character compared to the ground state. Hence their R_e values are slightly shorter than the ground state and the low lying Rydberg states show violet degraded vibrational structure. In a one-photon transition from the ground state the Rydberg electron is excited from a gerade antibonding π-orbital to a p or f Rydberg orbital abiding by the selection rule g$\leftrightarrow$u, whereas in a two-photon transition the Rydberg electron is promoted to an s or d orbital. As a result the use of resonant enhanced multiphoton ionisation techniques opens the way for a wider analysis of the Rydberg states.

1.4.1 Rydberg States of I_2

The lowest Rydberg state of I_2 $[^2\Pi_{3/2}]6s;2_g$ lies about 48000 cm^{-1} above the ground state, correlating with the dissociation products $I(^2P_{3/2})+ I^*(^4P_{5/2})$ at $\sim$ 67000 cm^{-1} [37]. Venkateswarlu [38] reported the high resolution VUV absorption spectrum of I_2, where many ungerade Rydberg series based on the $[^2\Pi_{3/2}]_g$ or $[^2\Pi_{1/2}]_g$ core of the molecule, were observed. Recently Donovan et al [39], using (2+1) REMPI spectroscopy, reported the observation of many gerade Rydberg states ($n\leq 11$), based on the $[^2\Pi_{3/2}]_g$ and $[^2\Pi_{1/2}]_g$ ionic cores. In addition three 5d Rydberg states based on each core were also observed.

1.4.2 Rydberg States of Cl_2

The lowest known gerade Rydberg state of Cl_2 is the $[^2\Pi_{1/2}]4s;1_g$ [42], which has a T_e value of 64027 cm^{-1} and ω_e of 650 cm^{-1}. Typically the Rydberg states of Cl_2 have a D_e value of $\sim$ 20000 cm^{-1} and an R_e value of 1.9 Å, close to that of the $X\ ^1\Sigma_g^+$ ground state [36]. The observation of twenty two gerade Rydberg states of Cl_2, based on both the $[^2\Pi_{3/2}]_g$ and $[^2\Pi_{3/2}]_g$ ionic cores (*s*- and *d-series*), will be discussed in chapter six.

1.5 Valence States

Twenty three valence states are predicted for diatomic halogen molecules, correlating with $^2P_{3/2}+^2P_{3/2}$, $^2P_{3/2}+^2P_{1/2}$ and $^2P_{1/2}+^2P_{1/2}$ dissociation products. In I_2 the best known valence states are the $X0_g^+$ (2440) ground state (D_e= 12547.2 cm^{-1}, R_e= 2.67 Å [43]) and the $B0_u^+$, $A1_u$ and $A'2_u$ (2431) excited states: they are bound with R_e $\sim$3.0 Å. The rest are either shallow or purely repulsive states.

Similarily in Cl_2 the $X0_g^+$ (2440) ground state (D_e=20876 cm^{-1}, R_e=1.99 Å) and the $B0_u^+$ (D_e=3943 cm^{-1}, R_e=2.43 Å [44]), A,A′, and B′ (2431) valence states

are bound, [33][34] . The $C1_u$ state is purely repulsive, and its use as an intermediate resonant state, to access final states will be discussed in chapter five.

1.6 The Use of Continuum Intermediate States to Access Bound Final States

Conventionally, in optical-optical double resonance (OODR) spectroscopy, a bound intermediate state is used. However, since most of the excited valence states of molecules are repulsive, or only weakly bound, this technique is somewhat limited. If repulsive intermediate states could be used to access the ion-pair states with thier large R_e values, it would open up many useful OODR routes.

One of the drawbacks of using an unbound intermediate state is, that the second photon must arrive within $\approx 10^{-13}$ - 10^{-14} s compared to $\approx 10^{-8}$ s for a bound intermediate state. To some extent this can be offset by tuning the second photon to around the red extremum of the second step f $\leftarrow$ i, if that limit corresponds to an extremum in the Mulliken difference potential $V_f(R)$ - $V_i(R)$. The absorption cross section for the second photon at this stationary point is thereby greatly enhanced. This can be seen from the reverse final $\rightarrow$ intermediate fluorescence, where the red extremum is marked by a very prominent maximum in the fluorescence intensity.

If the gradient of the repulsive intermediate state potential at the turning point of the unbound motion is less than the gradient of the inner wall of the upper bound state at this same point, then the Mulliken difference potential must exhibit a maximum, even if $V_i(R)$ is purely repulsive. If this condition is not fulfilled, the existence of a turning point in the potential depends on the precise form of the two potentials being compared.

For one-colour experiments, the conditions required to access an ion-pair state via a continuum intermediate state, near the red extremum of the second transition, are (i) a strongly allowed transition at the first step leading to a large cross-section for accessing the intermediate state, $\sigma_{i \leftarrow X}\ (\nu)$, and (ii) good overlap between the cross-section for accessing the intermediate state and the cross-section for accessing the final state, $\sigma_{f \leftarrow i}\ (\nu)$, in the frequency region around the red extremum. If these conditions are met, many OODR routes can be exploited in both diatomic and polyatomic molecules. In chapters three, four, and five, excitation of I_2 and Cl_2 molecules, via repulsive intermediate states, will be discussed.

1.7 The Role of Kinetic Energy in The Franck-Condon Principle

The Franck-Condon principle states that the positions and velocities of the nuclei are essentially unchanged during a transition between two electronic states. This is the classical description of the Franck-Condon principle.

The role of kinetic energy in the Franck-Condon principle was discussed by Mulliken in 1971 [45]. He considered the intensity structure in bound-free, and bound-bound transitions. The Mulliken difference potential is defined as:

$$X(R) = U''(R) + E_{\nu'} - U'(R) \tag{1.3}$$

where U″(R) and U′(R) are the potential energy functions for the lower and upper states, respectively, and $E_{\nu'}$ is the upper state vibrational energy [46], (see figure (1.3)). X(R) represents the locus of points which classically conserve nuclear position and momentum. The Mulliken difference potential represent all of the classical transition points, or semiclassically, points of stationary phase. At the point R^* the Mulliken difference potential is equal to the lower-state vibrational energy:

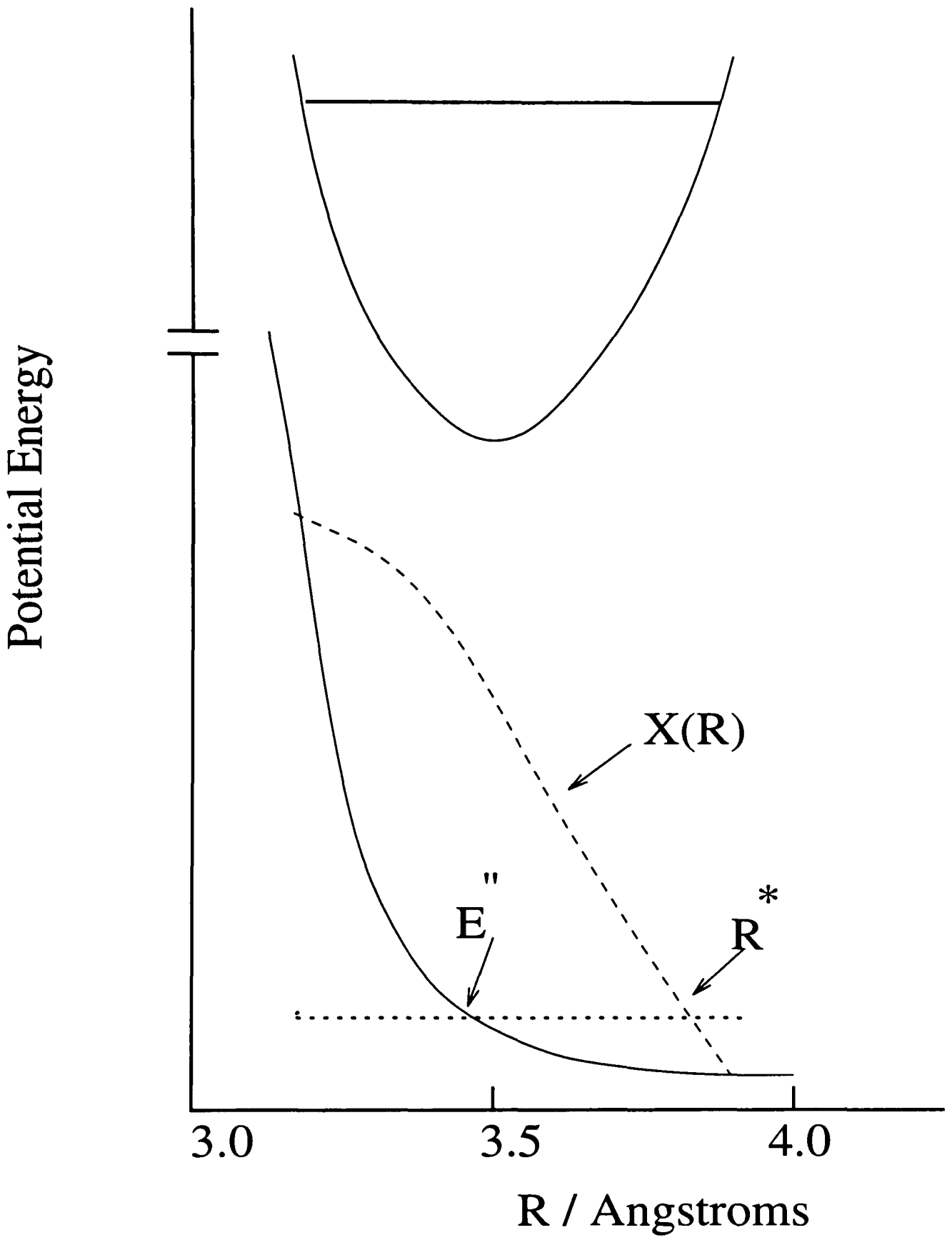

Figure 1–3: Diagram illustrating the Mulliken difference potential (dashed curve). In this case no extremum in the difference potential is seen.

$$E_{\nu''} = X(R^*) = U''(R^*) + E_{\nu'} - U'(R^*) \tag{1.4}$$

it follows that

$$E_{\nu''} - U''(R^*) = E_{\nu'} - U'(R^*) \tag{1.5}$$

Equation (1.5) confirms that the kinetic energy E - U(R) is the same for the upper and lower states at R=R*. Classically vertical transitions occur at R=R*, where R* is the 'classical transition point'. Using the R-centroid approximation, $\bar{R}$, is calculated as the weighted average value of internuclear distance during the transition. In the classical limit, when $\bar{R}$=R*, $E_{\nu'}$-U'(R*)=$E_{\nu''}$- U''(R*) is equal to the kinetic energy to be conserved during the transition [47].

When there is a single point of stationary phase for all accessible R, the function X(R) increases or decreases monotonically with R, and the spectrum displays reflection structure (one spectral peak for each peak in the radial probability density for the initial level v').

Figure (1.4) illustrates transitions to a bound lower state. For transitions to the unbound region there are two points of stationary phase, R_1^* and R_2^*, and the difference potential has an extremum at B, known as the red extremum. This is the region where the spectral density (transition probability per unit frequency interval) reaches a maximum [45]. The spectral density reaches another maximum in the region of the blue extrema at A and C, but these do not concern us here. The contributions to the overlap integral at R_1^* and R_2^* can add constructively or destructively, to yield further structure on the oscillatory continuum [46]. The use of the red extremum to access upper ion-pair states was discussed in the previous section, and will be further discussed in chapters three, four and five.

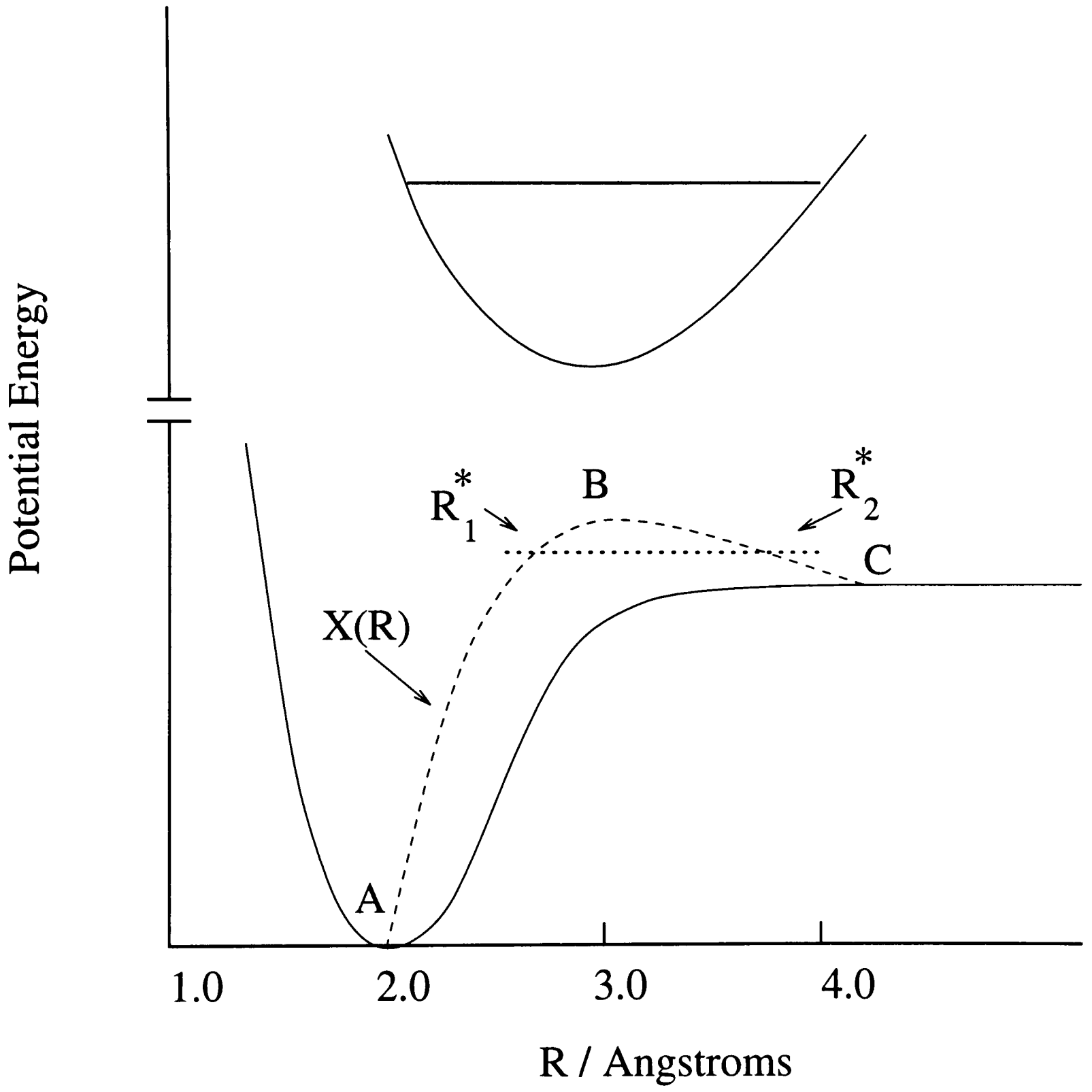

Figure 1–4: A diagram illustrating the Mulliken difference potential for a bound lower state. In this case there is an extremum in the difference potential.

1.8 The Born-Oppenheimer Approximation

The Schrödinger wave equation is expressed as;

$$\hat{H}\psi_i = E_i\psi_i \tag{1.6}$$

where $\hat{H}$ is the total Hamiltonian for a diatomic molecule, with electronic coordinates expressed in the molecule-fixed frame and, E is the total energy. The nonrelativistic Hamiltonian can be approximated by the sum of three operators;

$$H = T^N(R,\theta,\phi) + T^e(r) + V(r,R) \tag{1.7}$$

T^N the nuclear kinetic energy can be divided into vibrational and rotational terms, $T^N(R)+H^{ROT}(R,\theta,\phi)$. T^e is the electron kinetic energy, and V is the electrostatic potential energy for the nuclei and electrons [49].

The Born-Oppenheimer (BO) approximation considers the relative masses of the electrons and nuclei, and that electrons therefore move much faster than nuclei. Thus, the nuclei are regarded as fixed on the time scale for electronic transitions. In general, the separation between the electronic and nuclear motions, which constitutes the BO approximation, is very convenient. However, the observed levels are not exact eigenvalues of a given potential curve. The eigenvalues and eigenfunctions, which can be compared to observed energy levels, are expressed in terms of the BO representation.

The off-diagonal matrix elements of the Hamiltonian are as follows:

$$H = H^{el} + T^N(R) + H^{ROT} \tag{1.8}$$

The off-diagonal matrix elements of H^{el} give rise to electronic perturbations, $T^N(R)$ give rise to nonadiabatic interactions, and H^{ROT} give rise to rotational perturbations. In order to evalute perturbations which result from neglected terms

in the H^{el}+T^N(R) part of the Hamiltonian two kinds of BO representation are considered, (i) a crossing (diabatic) potential curve representation, where the off-diagonal matrix elements of H^{el} appear between the states of this representation, and (ii) a noncrossing (adiabatic) potential curve representation, where the T^N operator becomes responsible for perturbations [49].

Two types of off-diagonal matrix element determine how two states can interact.

$$\langle \psi_1^{el} \mid H^{el} \mid \psi_2^{el} \rangle \tag{1.9}$$

and

$$\langle \psi_1^{el} \mid T^N \mid \psi_2^{el} \rangle \tag{1.10}$$

The diabatic (crossing) potential curve representation arises from electronic wavefunctions ψ_d^{el}, for which expression (1.9) is non-zero, and expression (1.10) is zero. This gives rise to electrostatic perturbations, and the potential curves cross each other. The adiabatic (non-crossing) potential curve representation arise from electronic wavefunctions ψ_{ad}^{el}, for which expression (1.10) is non-zero, and expression (1.9) is zero, this gives rise to homogeneous interactions between states of the same symmetry [4] [50].

1.8.1 Homogeneous Interaction

Consider two electronic states of a diatomic molecule, (e.g. a Rydberg state with a potential curve M(R), and an ion-pair state with a potential curve N(R)), crossing each other at R_c, (solid curves in figure (1.5)). If the two states have the same symmetry, then homogeneous interaction occurs, forming an avoided crossing at R_c, (dotted curves). Irregular vibrational levels in the region of the avoided crossing

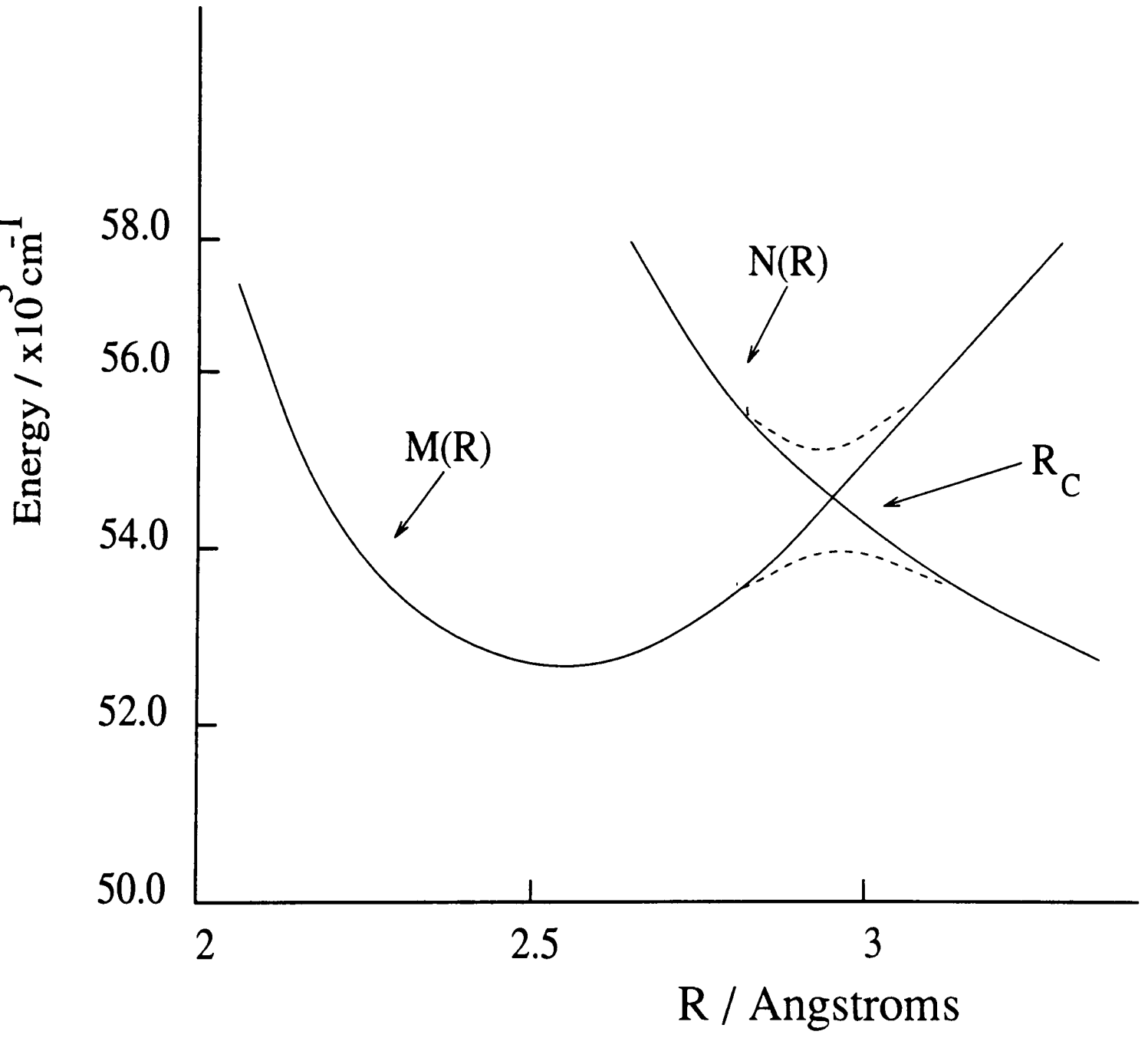

Figure 1–5: The diabatic curves (solid) cross at R_c, whereas the adiabatic curves (dotted) form an avoided crossing at R_c.

are observed, due to perturbations. When the two crossing states differ by $\Delta\Omega=\pm 1$, then heterogeneous interaction occurs, which leads to irregular rotational structure in the crossing region, but there is no avoided crossing (see solid curves in Figure (1.5)). Homogenous interactions between Rydberg states and ion-pair states in both I_2 and Cl_2 molecules, will be discussed in chapters six and seven.

1.9 Multiphoton Ionisation

For a one photon transition to ionise a halogen molecule (e.g. I_2) a photon of 130 nm wavelength would be required. To obtain such a short wavelength, a synchrotron radiation source, or four-wave mixing methods would have to be used. Also, the beam path would need to be evacuated, to remove strongly absorbing gases such as O_2. Standard quartz optics do not transmit short wavelengths and thus LiF or MgF_2 optics would need to be used. In a one-photon transition from the ground state selection rules restrict the number and symmetry of excited states that can be accessed. However, these restrictions can be overcome by multiphoton excitation, where two or more photons are used to access an eigen state. The absorption cross-sections for MPI are relatively small, and hence the transition probability is reduced. Tight focusing of the output laser beam is required.

The transition probability (W_n) of an n-photon process is given by [51]

$$W_n = \sigma_n \times I^n \tag{1.11}$$

where σ_n is the cross-section and I is the laser intensity. To obtain a relationship between the transition probability (ion yield) and the laser intensity, we may express equation (1.11) as follows,

$$lnW_n = ln\sigma_n + nlnI \tag{1.12}$$

Thus, a plot of $\ln W_n$ vs lnI, gives a straight line with a slope n, which is the number of photons involved in the transition. Thus an n-photon excitation is proportional to the n^{th} power of the laser intensity.

In non-resonant multiphoton ionisation the excited state is accessed via virtual states. The excitation photon is not resonant with a real state (eigenstate), and hence the process is referred to as non-resonant multiphoton ionisation. The cross-section for a non-resonant processes is much less than a resonant MPI process, (see Figure (1.6)).

Resonance enhanced multiphoton ionisation is achieved when the excitation process is via a real state, large enhancement of the ionisation is observed, hence known as (n+m) REMPI, where n is the number of photons for accessing a real state, and m is the number of photons to reach the ionisation continuum, (see Figure (1.6)).

The REMPI excitation technique can be combined with mass selective detection and the free-jet expansion technique. Under such conditions, the precooled molecules undergo selective ionisation, and can be detected by time-of-flight mass spectrometer. The congestion in the spectrum is greatly reduced when the jet-cooling method in used.

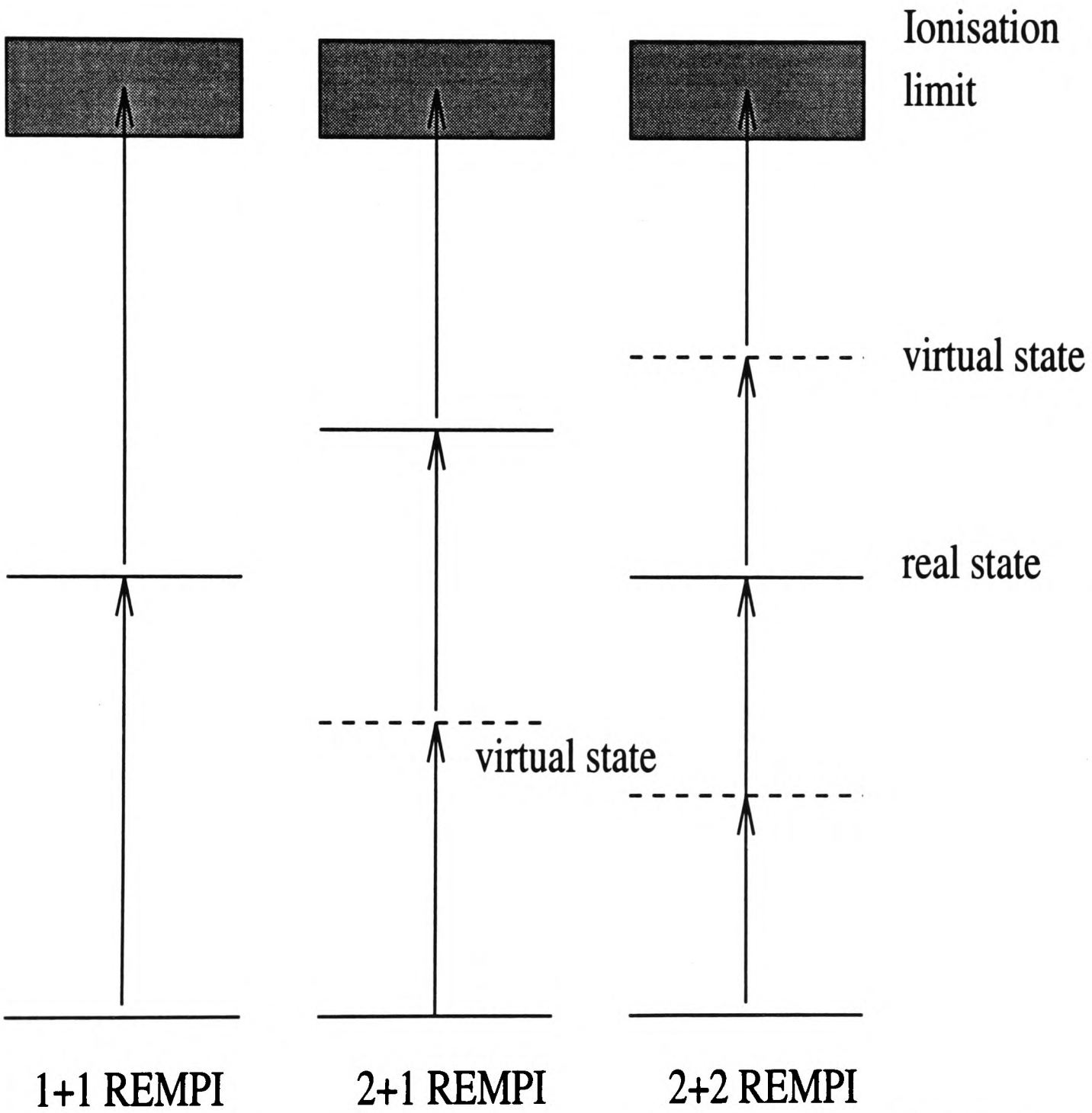

Figure 1–6: A schematic diagram showing three different REMPI schemes.

1.10 References

(1) R.S. Mulliken, J. Chem. Phys., 55 (1971) 288.

(2) E.S. Rittner, J. Chem. Phys., 19 (1951) 1030.

(3) J. Tellinghuisen, Can. J. Phys., 62 (1984) 1933.

(4) D.I. Austin, Ph.D. thesis, Edinburgh 1987.

(5) T. Ishiwata, A. Tokunaga, T. Shinzawa, and I. Tanaka, J. Mol. Spec., 117 (1986) 89.

(6) G.W. King, and T.D Mclean, J. Mol. Spec., 135 (1989) 207.

(7) T. Ishiwata, J. Yamada, and K. Obi, J. Mol. Spec., 158 (1993) 237.

(8) P. Jewsbury, T. Ridley, K.P.Lawley, and R.J. Donovan, J. Mol. Spec., 157 (1993) 33.

(9) K.S. Viswanathan, A. Sur, and J. Tellinghuisen, J. Mol. Spec., 86 (1981) 393.

(10) T. Ishiwata, T. Kusayanagi, T. Hara, and I. Tanaka., J. Mol. Spec., 119 (1986) 337.

(11) A.R. Hoy, and J.C.D. Brand, Chem. Phys., 109 (1986) 109.

(12) K.S. Viswanathan, and J. Tellinghuisen., J. Mol. Spec., 101 (1983) 285.

(13) J.S. Hickmann, C.R.M. De oliveira, and R.E. Francke, J. Mol. Spec., 127 (1988) 556.

(14) J.P.Perrot, A.J. Bouvier, A. Bouvier, B. Femelat, and J. Chevaleyre, J. Mol. Spect., 114 (1985) 60.

(15) G.W. King, I.M. Littlewood, and J.R. Robins, Chem. Phys., 56 (1981) 145.

(16) J.C.D. Brand, A.R. Hoy, A.K. Kalkar, and A.B. Yamashita, J. Mol. Spec., 95 (1982) 350.

(17) T. Ishiwata, I .Tanaka, Laser. Chem., 7 (1987) 79.

(18) A.R. Hoy, and R.H. Lipson, Chem. Phys., 140 (1990) 187.

(19) J.P. Perrot, B. Femelat, M. Broyer and J. Chevaleyre, Mol. Phys., 61 (1987) 97.

(20) J. Tellinghuisen, J. Mol. Spec., 94 (1982) 231.

(21) X. Zheng, S. Fei, M.C. Heaven, and J. Tellinghuisen, J. Chem. Phys., 96 (1992) 4877.

(22) J. Tellinghuisen, S. Fei, X. Zheng, and M.C. Heaven, Chem. Phys. Letts., 176 (1991) 373.

(23) T. Ishiwata, J. Si, and K. Obi, J. Chem. Phys., 96 (1992) 5678.

(24) T. Ishiwata, Y. Kasai, and K. Obi, J. Chem. Phys., 98 (1993) 3620.

(25) M.S.N. Al-Kahali, R.J. Donovan, K.P. Lawley, Z. Min, and T. Ridley, to be published in Chem. Phys.

(26) J. Wörmer, T. Möller, J. Stapelfeldt, G. Zimmerer, D. Haaks, S. Kampf, J. Le Calve, and M.C. Catex, Z. Phys. D-Atoms, Molecules and clusters. 7 (1988) 383.

(27) M.S.N. Al-Kahali, R.J. Donovan, K.P. Lawley, T. Ridley, and A.J. Yarwood, J. Phys. Chem. 99 (1994) 525.

(28) T. Ishiwata, T. Shinzawa, J. Si, K. Obi, and I. Tanaka, J. Mol. Spec., 166 (1994) 321.

(29) T. Ishiwata, T.Shinzawa, T. Kusayanagi, and I. Tanaka, J. Chem. Phys., 82 (1985) 1788.

(30) T. Ishiwata, J.H. Si, and K. Obi, J. Chem. Phys., 96 (1992) 5678.

(31) T. Shinzawa, A. Tokunaga, T. Ishiwata, and I. Tanaka, J. Chem. Phys., 83 (1985) 5407.

(32) T. Ishiwata, Y. Kasai, and K. Obi, J. Chem. Phys., 95 (1991) 60.

(33) T. Ishiwata, A. Ishiguro, and K. Obi, J. Mol. Spec., 147 (1991) 321.

(34) P.C. Tellinghuisen, B. Guo, D.K. Chakraborty, and J. Tellinghuisen, J. Mol. Spec., 128 (1988) 268.

(35) J.H. Si, T. Ishiwata, and K. Obi, J.Mol.Spec., 147 (1991) 334.

(36) T.Möller, B. Jordan, P. Gürtler, G. Zimmerer, D. Haaks, J. Le Calve, M.C. Castex, Chem. Phys., 76 (1983) 295.

(37) C.E. Moore, Atomic Energy Levels, Vol.III Natl.Bur.Std.1971.

(38) P. Venkateswarlu, Can. J. Phys., 48 (1970) 105.

(39) R.J. Donovan, R.V. Flood, K.P. Lawley, A.J. Yencha and T. Ridley, Chem. Phys., 164 (1992) 439.

(40) S.D. Peyerimhoff, and R.J. Buenker, Chem. Phys., 57 (1981) 279.

(41) A.E. Douglas, Can. J. Phys., 59 (1981) 835.

(42) L. Li, R.J. Lipert, H. Park, W.A. Chupka, and S.D. Colson, J. Chem. Phys.,

88 (1988) 4608.

(43) R.J. Leroy, J. Chem. Phys., 52 (1970) 2683.

(44) J.A. Coxon, J. Mol. Spec., 82 (1980) 264.

(45) R.S. Mulliken, J. Chem. Phys., 55 (1971) 309.

(46) J. Tellinghuisen, Adv. in Chem. Phys.,Vol LX, (1985) p299.

(47) C. Noda, and R.N. Zare, J. Mol. Spec., 95 (1982) 254.

(48) K. Tamagake and D.W. Setser, J.Chem.Phys., 67 (1977) 4370.

(49) H. Lefebvre-Brion and R.W. Field, Perturbations in The Spectra of Diatomic Molecules, Academic Press 1986.

(50) P.J. Wilson, Ph.D. thesis, Edinburgh, 1994.

(51) P. Lambropoulas, Appl. Opt, 19 (1976) 87.

Chapter 2

Experimental

2.1 Introduction

This chapter describes the various techniques and experimental details used in obtaining the results in this thesis. Where appropriate additional experimental details are discussed in the relevant chapters. The main technique used in this thesis was jet-cooled resonance enhanced multiphoton ionisation spectroscopy, with the ions being detected using time-of-flight mass spectrometry. The experimental arrangement is illustrated in Figure (2.1).

Multiphoton Ionisation

Multiphoton ionisation is an n-photon absorption process leading to ionisation and obeys the condition

$$nh\nu \geq IP \tag{2.1}$$

where hν is the photon energy and IP is the molecular ionisation potential. This process is non-selective, as both atoms and molecules will be ionised providing that equation (2.1) is satisfied. The absorption probability for any molecule or atom is greatly enhanced when the energy of an integral number of photons (nhν) is equal to the energy difference between two states in the absorbing species, an enhancement of the ion signal is obtained in such case. In a one-colour experiment a single photon may excite an eigen state S_1 followed by ionisation by a second photon of the same energy.

$$IP \leq 2h\nu_{S_1} \tag{2.2}$$

The ion-yield enhancement will be equal to the ratio of the absorption cross-section for a real state relative to the cross-section through virtual states. This

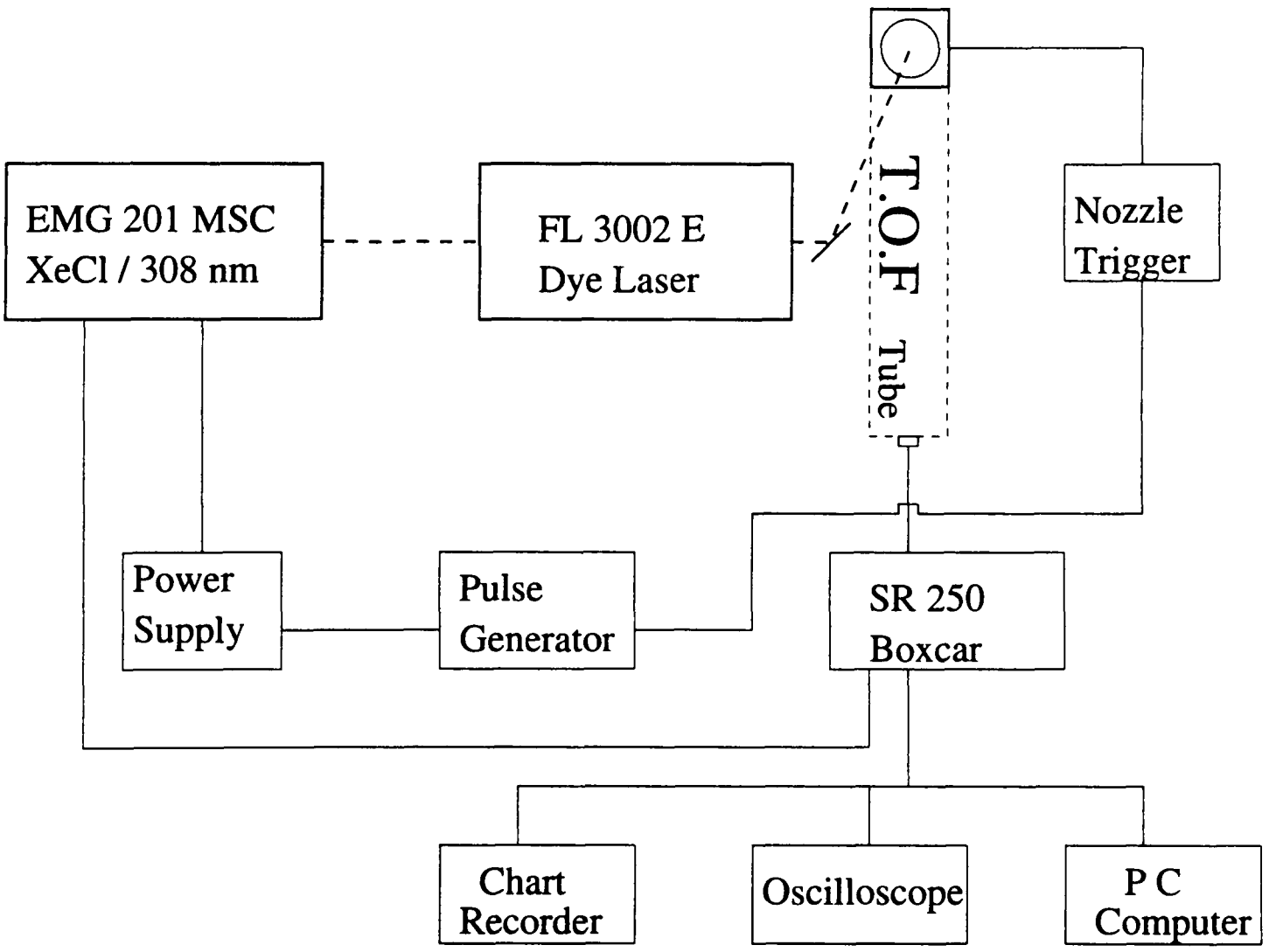

Figure 2–1: Schematic block diagram of the experimental setup used in one-colour excitation.

process is known as one-colour resonance-enhanced, two-photon ionisation or R2PI. If equation (2.2) is not satisfied, resonantly enhanced ionisation can be effective with a two-colour process provided the energy of the second photon exceeds IP-$h\nu_{S_1}$. Three photon or higher order process can be used, bearing in mind that in a (n+m) REMPI scheme, processes that have m > 1 are low in efficiency. The two-colour process although efficient, demands exacting spatial and temporal coincidence of the two laser beams [1].

To produce a laser field of sufficiently high intensity to induce simultaneous absorption of two or more photons, the pulsed lasers are tightly focussed. For one-photon transitions the cross-section is typically, $\sigma_1 \simeq 10^{-18}$ cm^2, for a two-photon transition $\sigma_2 \simeq 10^{-50}$ cm^{4}s, and for a three-photon transition $\sigma_3 \simeq 10^{-82}$ cm^{6}s^2, which indicates that the laser flux must be of the order of 10^{28} photons cm^{-2}s^{-1} to give a two-photon absorption process as high a rate as a single photon absorption process. For instance for a 300 μJ pulse, a laser intensity of 100 MW cm^{-2} is obtained. In the wavelength region 200-300 nm, this is equivalent to 10^{28} photons cm^{-2}s^{-1} [2][3].

Jet-Cooling

When the REMPI technique is combined with supersonic jet-cooling, the spectrum is very much simplified. The pressure broadening of spectral lines is removed, also the Doppler broadening is considerably reduced when observations are made perpendicular to the molecular beam. Another important outcome of jet-cooling is rotational cooling, as a result the rotational temperature, which is the temperature that describes the Boltzmann population distribution among rotational levels, is significantly reduced. Vibrational cooling also occurs but not as efficiently as the rotational cooling. All these conditions assist in the analysis and interpretation of the spectra.

Basically, the amount of cooling increases when atoms or molecules are pumped from a higher pressure side to a vacuum, through a narrow slit or nozzle, with a typical diameter of 200 μm. Supersonic jet-cooling is obtained when the slit or nozzle diameter d is greater than the mean free path λ_0 for collisions between the atoms or molecules, passing through it.

In the expansion, random thermal motion is converted into directional flow, and the range of velocities is very much reduced. Collisions are still occuring in the region just beyond the nozzle and the flow of the gas is said to be a hydrodynamic flow, whereas beyond this region the gas flow is molecular (in the molecular flow region no collisions occur).

The conditions that are needed to obtain the lowest temperatures, are high backing pressures and supersonic speeds, normally quoted in terms of the Mach number M. For a supersonic jet, M the Mach number has to be greater than 1. In a jet of atoms or molecules with mass flow velocity u,

$$M = u/a \tag{2.3}$$

where

$$a = (\gamma kT/m)^{1/2} \tag{2.4}$$

$\gamma = C_P/C_V$ is the ratio of the heat capacities of the monoatomic gas at constant pressure and volume. An atomic gas, such as helium or argon, which has no rotational or vibrational degrees of freedom, and hence has low heat capacity, is ideal for producing a large temperature decrease. Molecules injected into the supersonic jet undergo relative cooling, in relationship to their translational and rotational degrees of freedom due to two-body collisions with the atomic carrier gas. Vibrational cooling also occurs to a lesser extent [3].

Better rotational and vibrational cooling and lesser tendency for condensation is obtained when a pulsed supersonic jet is used. When a pulsed dye laser is used for the excitation of the molecules, the pulsed jet and the laser pulses can be synchronized.

One disadvantage is that the rotational constants obtained in supersonic jet experiments are less accurate than those obtained at room temperature. This is because rotational term values depend on the second power of the quantum numbers (J), or higher powers if centrifugal distortion is included, and only low J levels are populated in the expansion.

Laser Mass Spectrometry

Laser mass spectrometry involves the ionisation of a molecule, using a tunable laser rather than the traditional electrical methods. In most cases laser ionisation has to involve a multiphoton excitation process. An advantage of using laser mass spectrometry is that different types of ions produced by multiphoton excitation can be distinguished.

A typical laser mass spectrometer is based on a pulsed dye laser pumped by an excimer laser, as in our case. Generally samples are introduced into the system in the gas phase, through the pulsed nozzle into the evacuated ionisation chamber.

A well known method in laser mass spectrometry, is the time-of-flight (TOF) analysis. Here the ions produced by the laser action are electrically accelerated, and pass into a field free drift tube about a metre long. Because all ions entering the tube have the same kinetic energy, their velocities in the drift tube must vary inversily with their masses, the lighter ions arriving at the detector earlier than the heavier ions. The flight times are typically 1 to 30 μsec, depending on the molecule to be analysed. The detector in the time-of-flight mass spectrometer used was a microchannel plate detector: high electron gains can be achieved using

this kind of electron multiplier.

Since nanosecond laser pulses are used to produce ionisation, the mass spectrum is obtained by measuring the ion current as a function of the time elapsed since the laser pulse [4]. In a time-of-flight (TOF) mass spectrometer, the ions are separated by their time-of-flight (t) along a T.O.F tube of length l [5];

$$t = l\sqrt{\frac{1}{2U}\frac{m}{e}} \tag{2.5}$$

Where U is the voltage and e is the electronic charge. $2Ue$ can be taken as constant and the velocity v of an ion is expressed as;

$$v \propto \sqrt{1/m} \tag{2.6}$$

Hence the flight-time t of an ion of mass m for a flight length l is given by

$$t \propto l\sqrt{m} \tag{2.7}$$

Therefore the time taken for the ion to reach the detector is proportional to the square root of its mass.

In laser mass spectrometry, the mass spectrum may change with the laser wavelength. The multiphoton ionisation process is known to be efficient when resonance conditions exist and a different mass fragmentation pattern may be recorded at different resonances, hence providing more information on the structure of the molecule. This process is known as resonance enhanced multiphoton ionisation mass spectrometry.

2.2 The Excimer-Pumped Dye Laser System

The basic experimental arrangement for one-colour excitation is shown in Figure (2.1). A Lambda Physik EMG 201 MSC excimer laser operating at 308 nm, delivered short pulses, of 25 ns duration, with an energy output of 400 mJ/pulse and a repetition rate of 3-6 Hz. The Lambda Physik FL3002E dye laser was pumped using the output UV radiation from the excimer laser. The fundamental output of the FL3002E dye laser was of 15 ns duration with an energy of 30-50 mJ/pulse and a bandwidth of 0.2 cm^{-1}. Laser pulse energies were recorded using a Gentec ED-200 Joulemeter. The wavelength range of the available Lambda Physik laser dyes covering the region down to 335 nm, used in the experimental work in this thesis are listed in Table (2.1).

Since the exciting radiation is 308 nm, non-linear optical methods were used to obtain continuously tunable radiation for wavelengths below 335nm. Second Harmonic Generation (SHG) techniques were used to obtain a coherent laser beam of frequency-doubled radiation from the dye laser. The non-linear optical crystals used were potassium dihydrogen phosphate (KDP), and barium beta borate (BBO), supplied by Lambda Physik (KDP : FL30;31, BBO : FL37), see Table (2.2).

Second harmonic efficiency depends on the angle between the incident beam and the surfaces of the crystal. Simultaneous scanning of the grating and the tilt of the crystal was controlled by a microcomputer in the FL3002E dye laser. A Lambda Physik FL301 compensating prism was used to reduce displacement (beam walk) induced by angle tuning. A UG5 filter was used to separate the frequency- doubled radiation from the fundamental beam (this was employed only when using the KDP crystal). A Lambda Physik FL35 device was used for the BBO crystal, it consists of four quartz Pellin-Broca prisms. The use of the

Dye	**Range(nm)**	**Peak(nm)**	**Efficiency %**
Rhodamine 101	614–672	623	12
Rhodamine B	588–644	600	12
Rhodamine 6G	569–608	581	16
Coumarin 153	522–600	540	15
Coumarin 307	479–553	500	16
Coumarin 102	460–510	480	18
Coumarin 47	440–484	456	18
Coumarin 120	423–462	441	15
Stilbene 3	412–443	425	9

Table 2–1: Dyes used in this thesis, all dyes were supplied by Lambda Physik.

Crystal	**Material**	**Range(nm)**
FL30,31	KDP	260–345
FL37-1	BBO	215–315

Table 2–2: Second Harmonic Generation Crystals.

frequency-doubling technique reduced the output energy of the dye laser by $\sim 90\%$.

The experimental setup for two-colour excitation will be described in detail in chapter five.

2.3 Molecular Beam and Jet-Cooling System

The molecular beam was produced by passing a backing pressure of $\sim$ 0.5-1 atm of argon gas over solid I_2 at room temperature (or Cl_2 at a pressure of $\sim$1 atm, in a 5% mixture of Cl_2 in He), then through a commercial pulse valve (General Valve Corporation Series 9). This was driven by a solenoid with a teflon tip, and had an orifice diameter of 250 μm. The open/close time of the orifice was controlled by a driver unit (General Valve), which triggered a pulse generator (Farnell PG 102). The output from the pulse generator triggered the excimer laser. The open-time of the orifice varied between 250-350 μs.

The nozzle was placed in a cubic (7×7×7cm) ionisation chamber pumped to a pressure of 2×10^{-7} mbar by a 6 inch diffusion pump, with liq. N_2 trap. The pressure was monitored using Pirani and Penning gauges (Edwards model 1102). Rotational cooling to $\sim$ 10 K was obtained in the molecular beam.

The ionisation chamber contains two conical electrodes, one positioned above the molecular beam, with a potential of $\sim$ +2 kV (supplied by a Brandenburg photomultiplier power supply, model 472R), and the other positioned beneath the molecular beam, at ground potential (see Figure (2.2)). The latter had a 2 mm hole, through which the ions were extracted into the T.O.F. tube. A 4 inch diffusion pump took the pressure in the time-of-flight tube below 1×10^{-6} mbar with the valve closed. A background pressure below 1×10^{-4} mbar was obtained with the nozzle running. Both diffusion pumps were backed by a rotary pump.

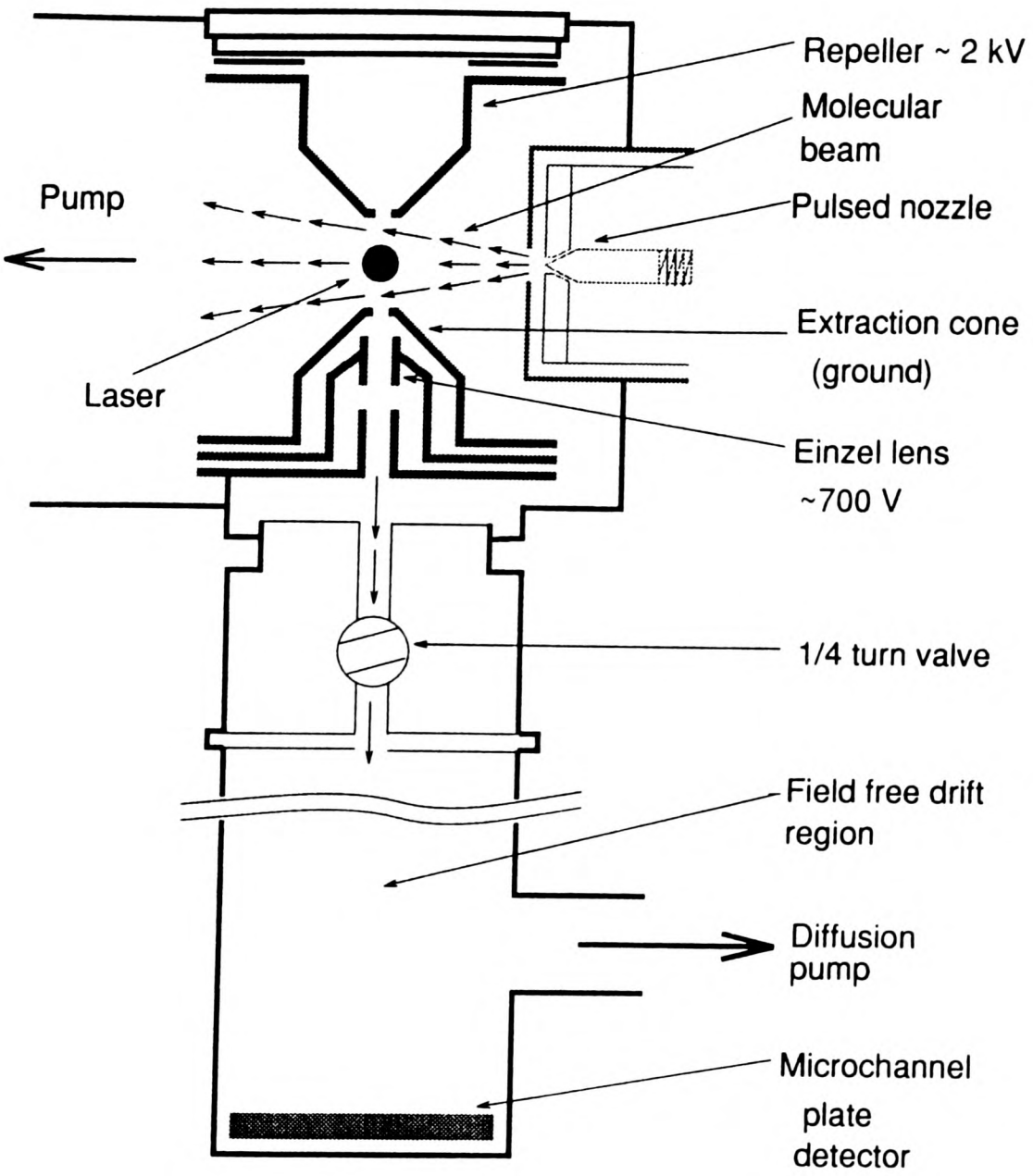

Figure 2–2: An expansion of the Time-Of-Flight tube and the pulsed jet.

2.4 Signal Detection and Data Collection

Time Of Flight Tube

The rotationally cooled molecules from the molecular beam were excited and then ionised by the UV radiation from the laser beam in the ionisation chamber. The positive ions formed were repelled by the upper conical electrode due to the applied voltage $\sim$ +2 kV, and were then accelerated towards the 2 mm hole in the ground potential conical electrode. The ions were collimated by an Einzel lens(6 mm diameter, 500-600 V potential) towards the field free drift region in the time-of-flight tube ($\sim$ 70 cm long). The circuit diagram for the ionisation chamber is illustrated in Figure (2.3).

The positive ions were collected by the microchannel plate detector, negatively charged to $\sim$ - 4.1 kV supplied by a Brandenburg high voltage generator type S.0530/10. The current was produced by ion packets arriving at the detector at different times, after passing through the field free drift region. The ions experienced a strong acceleration towards the first microchannel plate (at high negative potential), where a 'shower' of electrons was produced. These were accelerated towards the second plate where the signal was amplified by two to three orders of magnitude. These electrons then hit the anode and the current produced was converted to a voltage, which was then diplayed on a digital oscilloscope (Lecroy 9400A). Figure (2.4) shows the voltage supply and voltage dividers for the microchannel plate detector.

Boxcar Gated Integrator

The SR250 Gated Integrator and Boxcar Averager(Stanford Research Systems), consists of a gate generator, a fast gated integrator and an exponential averaging facility. The microchannel plate signal was sampled after a fixed time delay by

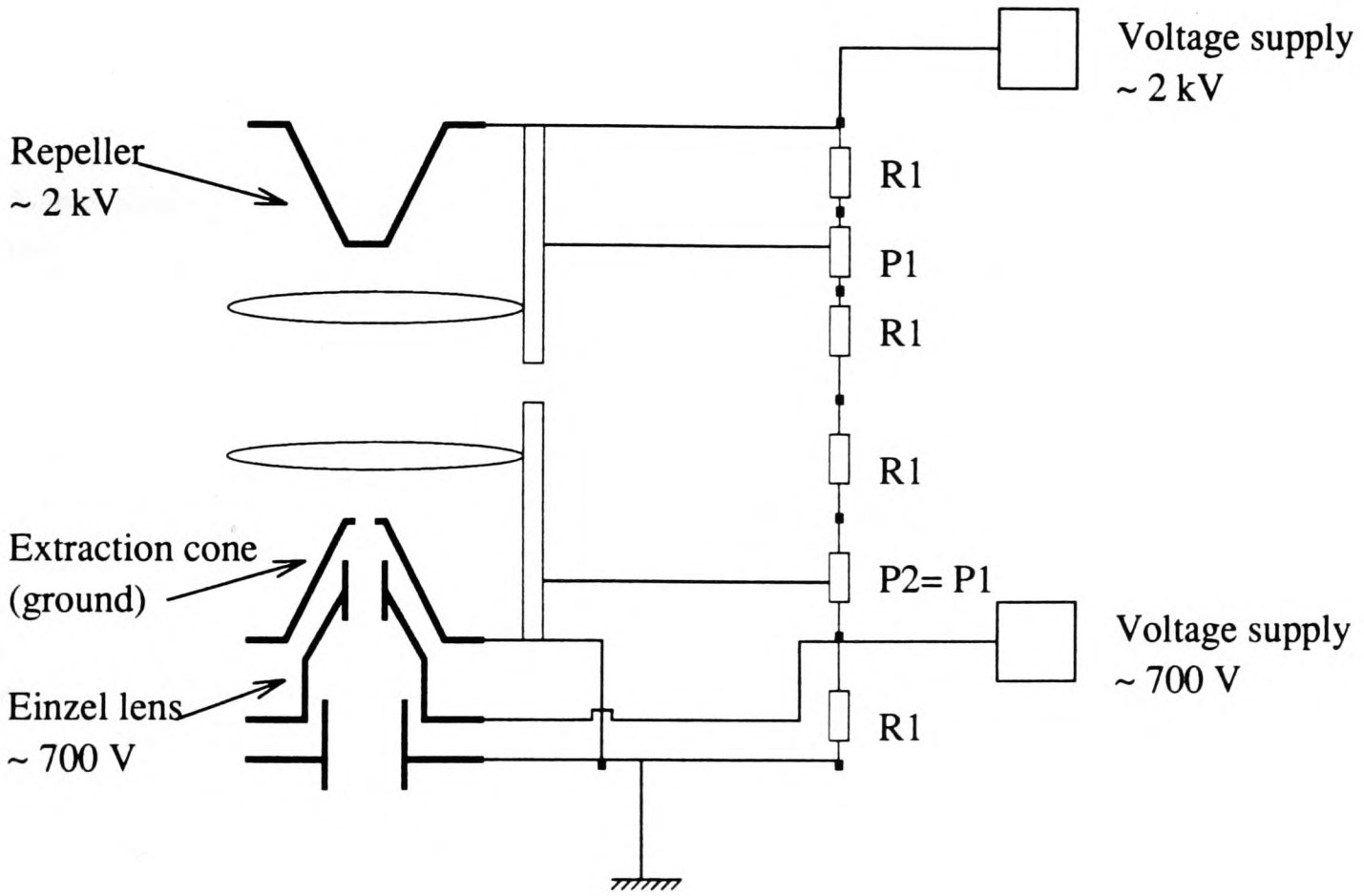

Figure 2–3: The circuit diagram for the ionisation chamber, showing the relevant voltage dividers and power supplies.

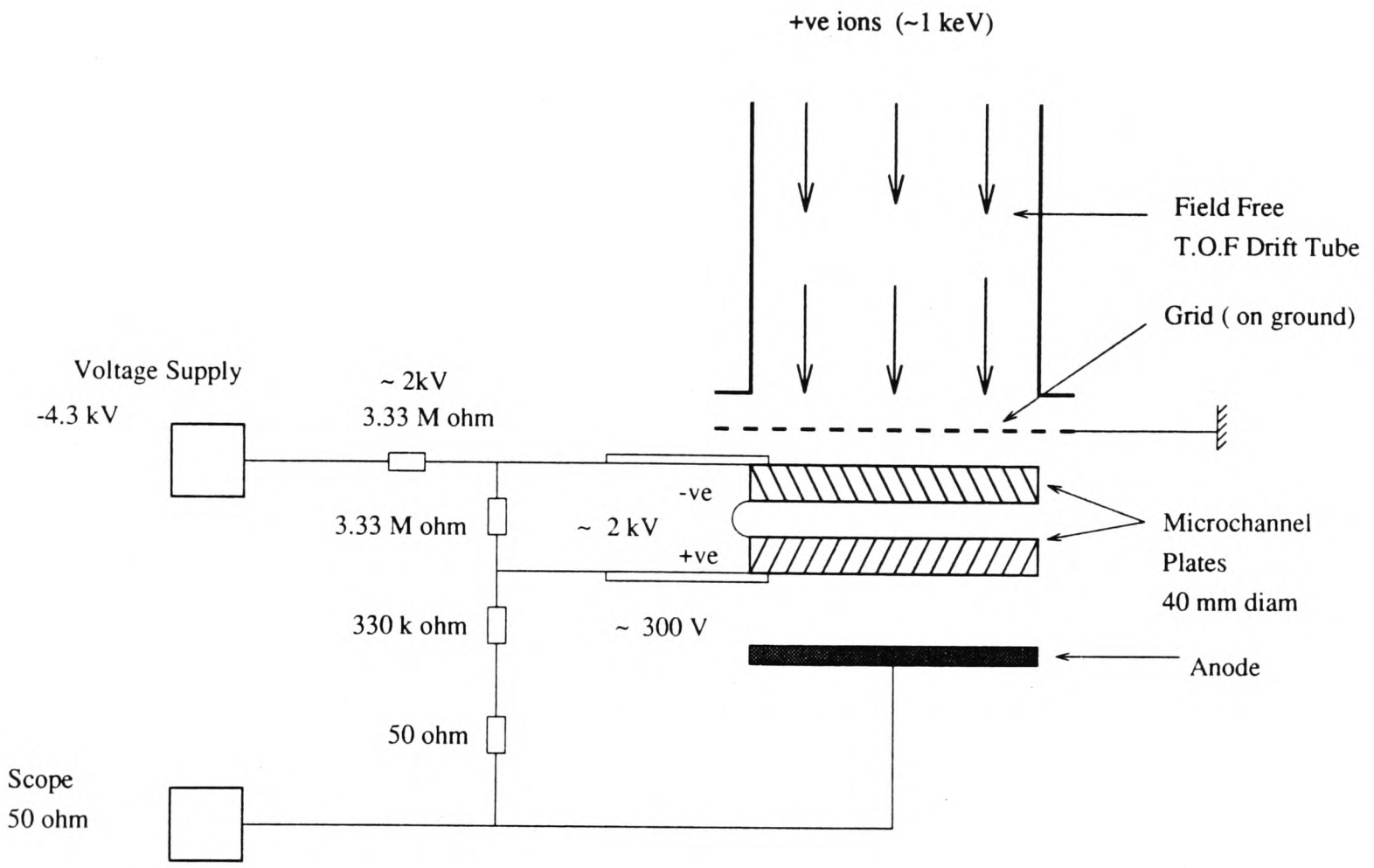

Figure 2–4: The circuit diagram for the microchannel plate detector, illustrating the voltage applied between the microchannel plate and the anode.

the SR250 boxcar, which was triggered by the excimer laser. The gate delay and width were set by displaying the microchannel plate output signal and the boxcar gate simultenously on the digital oscilloscope (Lecroy 9400A), and adjusting the SR250 boxcar to ensure optimum sampling. See Figure (2.5).

The signal was integrated over the opening time of the gate by the fast gated integrator. The gate width normalised the output from the integrator. A voltage proportional to the average of the input microchannel plate signal during sampling time was obtained. Moving exponential averaging of this normalised signal was then done over a pre-selected number of laser shots in order to smooth the microchannel plate signal , ensuring that the resolution was not affected by excess smoothing. The mass resolution Δm was calculated and found to be within 0.5%. The output from the SR250 boxcar was sent to a chart recorder (Kipp and Zonen BD8) and to a computer interface (Stanford Research Systems SR245), to be digitised. The information was then sent to an IBM PC-XT microcomputer.

Data Storage

Data collection and storage was controlled by a software package (Stanford Research Systems SR265), implemented on an IBM PC-XT microcomputer. Before recording the spectrum, the number of data collection bins was selected (i.e 5000), and input into the IBM PC-XT microcomputer. The laser wavelength was scanned using the dye-laser microcomputer and the wavelength range covered was input into the IBM PC-XT microcomputer. Hence the stored sampled data from start to finish, corresponds to the wavelength range scanned by the dye-laser microcomputer. The data collection interface was triggered from the boxcar, which was initially triggered by the firing of the excimer laser.

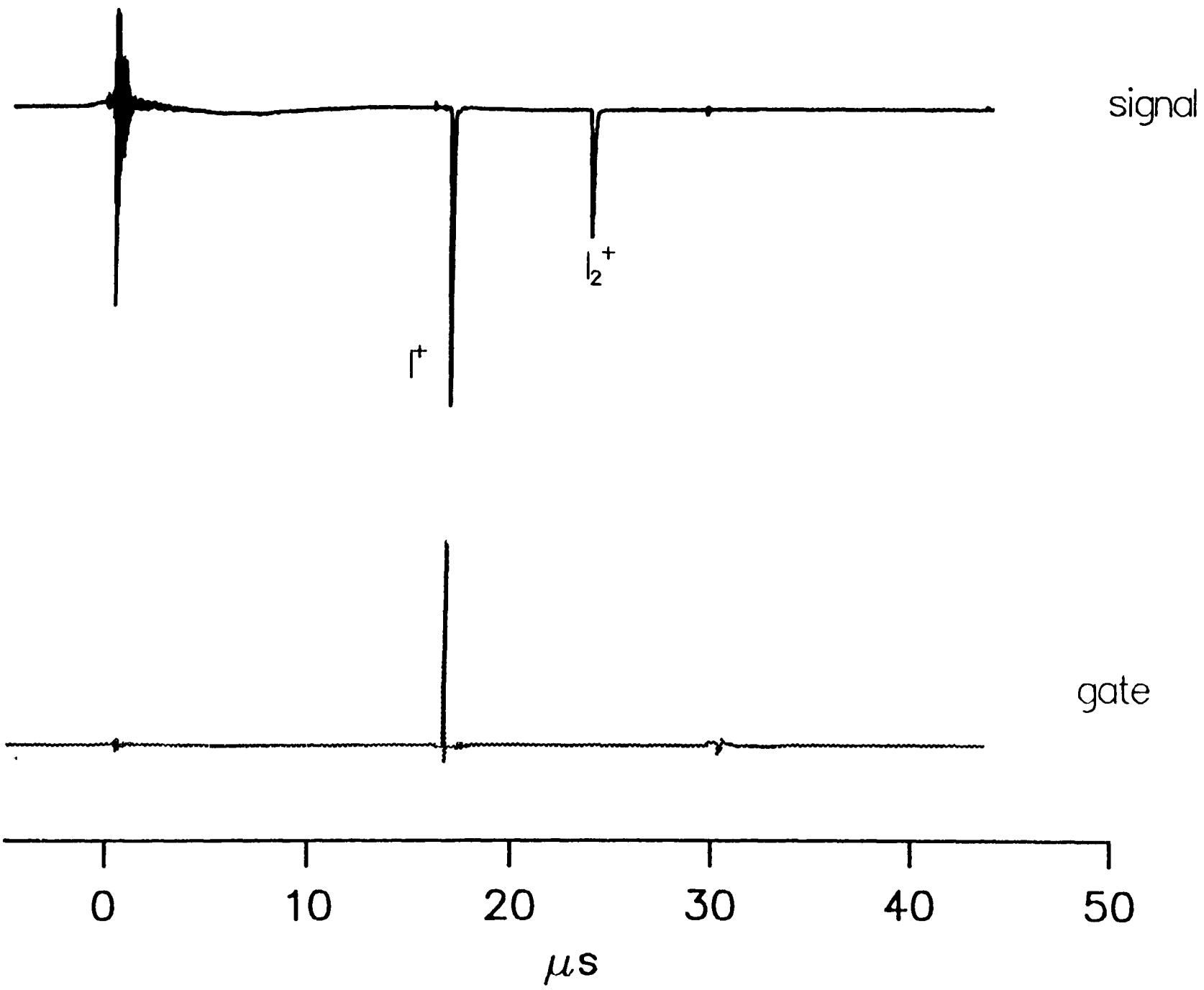

Figure 2–5: The signal from the MCP detector for Iodine molecule, the gate in this case is fixed on the I^+.

2.5 Data Handling

Laser Power Normalisation

The spectra were normalised to the power of the laser radiation. This was done by recording the relative power of the laser output as a function of wavelength. A beam splitter was used to split the output of the FL3002E dye laser beam in the ratio 9:1. The smaller fraction was directed to a photodiode, the output of which was sent to the boxcar and then to the computer to be recorded. The photodiode was covered by filters to avoid saturation.

For two-photon excitation the spectrum was divided by the square of the laser power. In a three-photon excitation the spectrum was divided by the cube of the laser power to obtain a normalised spectrum and so on.

Polarisation

The output of the fundamental Fl3002E dye laser is linearly (vertically) polarised. However the frequency-doubled output is horizontally polarised. A polariser (Lambda Physik FL50) was placed in the frequency-doubled beam during polarisation studies to obtain a ratio of 10:1, horizontal to vertical polarisation.

A soleil-Babinet polariser (Melles-Griot, cat no:045BC 001) was placed in the path of the polarised output of the FL3002E dye laser, to obtain circularly polarised light. The polariser was placed in the beam path before the focusing lens.

Calibration

The optogalvanic signal from a neon filled Hollow Cathode Lamp was used [8]. The voltage to the hollow cathode lamp was supplied by a Cathodeon Hollow

Cathode Lamp supply (C610). The optogalvanic signal was recorded as a function of wavelength, the sharp peaks, which were due to atomic transitions of Ne, were then compared to the values quoted in an Atlas of Neon Spectra [9].

Below 335 nm, the optogalvanic spectrum is sparse. Here the fundamental output of the FL3002E dye laser, was passed into a small cell containing Solid I_2, where the total fluorescence of the B→X transition was recorded using a Hamamatsu R 928 photomultiplier tube. The band positions were compared to those in the Iodine Atlas [10]. The laser beam was passed through the cell before being passed through the device that separates the frequency doubled radiation from the fundamental beam.

2.6 Reference

(1) John.M. Hayes, Chemical Reviews, 87(1987) 745-760.

(2) G.G. McFadyen, Ph.D. thesis, University of Edinburgh 1991.

(3) P.M. Johnson and C.E. Otis, Ann. Rev. Phys. Chem., 32 (1981) 139-157.

(4) J.M. Hollas, High Resolution Spectroscopy, Butterworth & Co Ltd, 1989.

(5) D.L. Andrews, Lasers in Chemistry, 2nd ed, Springer-Verlag, 1990.

(6) L. Moenke-Blankenburg, Laser Microanalysis, N.Y. John Wiley & Sons, 1989.

(7) 'Lambda Physik FL3002/2 Instruction Manual' (Gottingen,March, 1986)

(8) 'Lambda Physik EMG 201-204 MSC Instruction Manual' (Gottingen, April, 1985).

(9) S.H. Ashworth and J.M. Brown, An Atlas of Optogalvanic Transition in Neon. SERC Rutherford Appleton Lab,1991.

(10) S. Gerstenkorn, and P. Luc, Atlas du Spectre d'Absorption de la molecule Iodide Partie II. Editions du Centre National de la Rechereche Scientifique, Paris, 1978.

Chapter 3

One-colour Excitation of the $E0_g^+$ Ion-pair State of I_2 *Via* the Continuum of the $B0_u^+$ State

3.1 Introduction

In previous studies on repulsive intermediate states, Kasatani et al. [1] recorded the dispersed fluorescence from I_2 following two-photon one-colour excitation via a repulsive intermediate state. It was shown that when the excitation wavelength was less than 500 nm a strong new feature was observed in the spectrum. This new feature was attributed to excitation to the $D'2_g$ ion-pair state, via the repulsive $B''1_u$ state. In further studies on diatomic molecules, Koch et al.[2], and Young [3], in (1+1) two-photon transitions, reported the excitation of Li_2 and HI, respectively, via repulsive intermediate states. Both reported that the spectra were enhanced due to resonance with continuum intermediate states, but the overall transitions were essentially vertical.

By contrast, in a mass-resolved, two-photon resonant, three-photon ionisation study of jet-cooled Cl_2, Li et al.[4], observed extensive ion-pair and Rydberg levels, most of which could not be populated by a vertical two-photon transition from the ground state. It was proposed that the excitation went via the purely repulsive C 1_u state. The work carried out by Li et al. has been re-examined, and this will be discussed later in chapter five. Similar effects have been observed in polyatomic molecules. Bigio and Grant [5], reported a two-photon excitation of NO_2 from the bent $^2A_1$ ground state, via a dissociative continuum intermediate, to the $^2\Sigma_u^+$ linear Rydberg state. Strobel et al.[6], using the zero kinetic energy (ZEKE) photoelectron technique, reported two-photon ionisation of methyl iodide, resulting in the CH_3I^+ and CD_3I^+ ions in the $\bar{X}\ ^2E_{3/2}$ and $^2E_{1/2}$ electronic states. The two-photon spectra were resonantly enhanced via the dissociative A-state continuum and exhibit extensive vibrational structure in ν_3, the C-I stretching vibration. In contrast, the conventional one-photon photoelectron spectrum of methyl iodide showed almost no vibrational structure. In both cases a modest stretching of the N-O and C-I bonds was observed resulting in extended vibrational progressions in the final state. In this chapter the excitation of some low vibrational levels of the $E0_g^+$ ion-pair state of I_2, in a one-colour double resonance process via the

repulsive wall of the $B0_u^+$ state, above its dissociation limit, will be discussed. This is illustrated in Figure (3.1). Bond stretching of the order of 1 Å is observed.

3.2 Experimental

The basic experimental arrangement has been described in detail in chapter two. The only species recorded in these studies was I^+. The output of the dyes Coumarin 120 and Stilbene 3, with typical energies of 20 mJ per pulse, were used to excite the molecular beam, formed by passing $\approx$ 0.5 atm of argon over I_2 at room temperature. Calibration was achieved by the simultaneous recording of the optogalvanic signal from a neon filled hollow cathode lamp.

3.3 Results

Figure (3.2) shows the resonance ionisation spectrum of I_2 in the one-photon wavelength region 419 - 450 nm (corresponds to a two-photon energy range of 47732 – 44444 cm^{-1}). In analyzing this spectrum all possible (n+m) REMPI excitation schemes were considered. The only consistent scheme involves (2+2) REMPI via the $E0_g^+$ ion-pair state following the excitation scheme

$$E0_{g\,(v'=40-71)}^+ \leftarrow B0_u^+\text{:continuum} \leftarrow X0g^+$$

Using the known molecular constants [7] in the region 45100 - 47700 cm^{-1}, the bands can be unambiguously assigned as shown, see Table (4.1). Most of the strong bands originate from $v'' = 0$ of the X state although some hot bands from $v'' = 1$ and 2 are also observed. The expected experimental error was ± 2 cm^{-1}. However, there were additional errors because the bands are broad and there are sequence bands from $v'' = 0$ and $v'' = 1$ of the ground state, together with bands that overlap with atomic lines. At the highest E state vibrational level populated

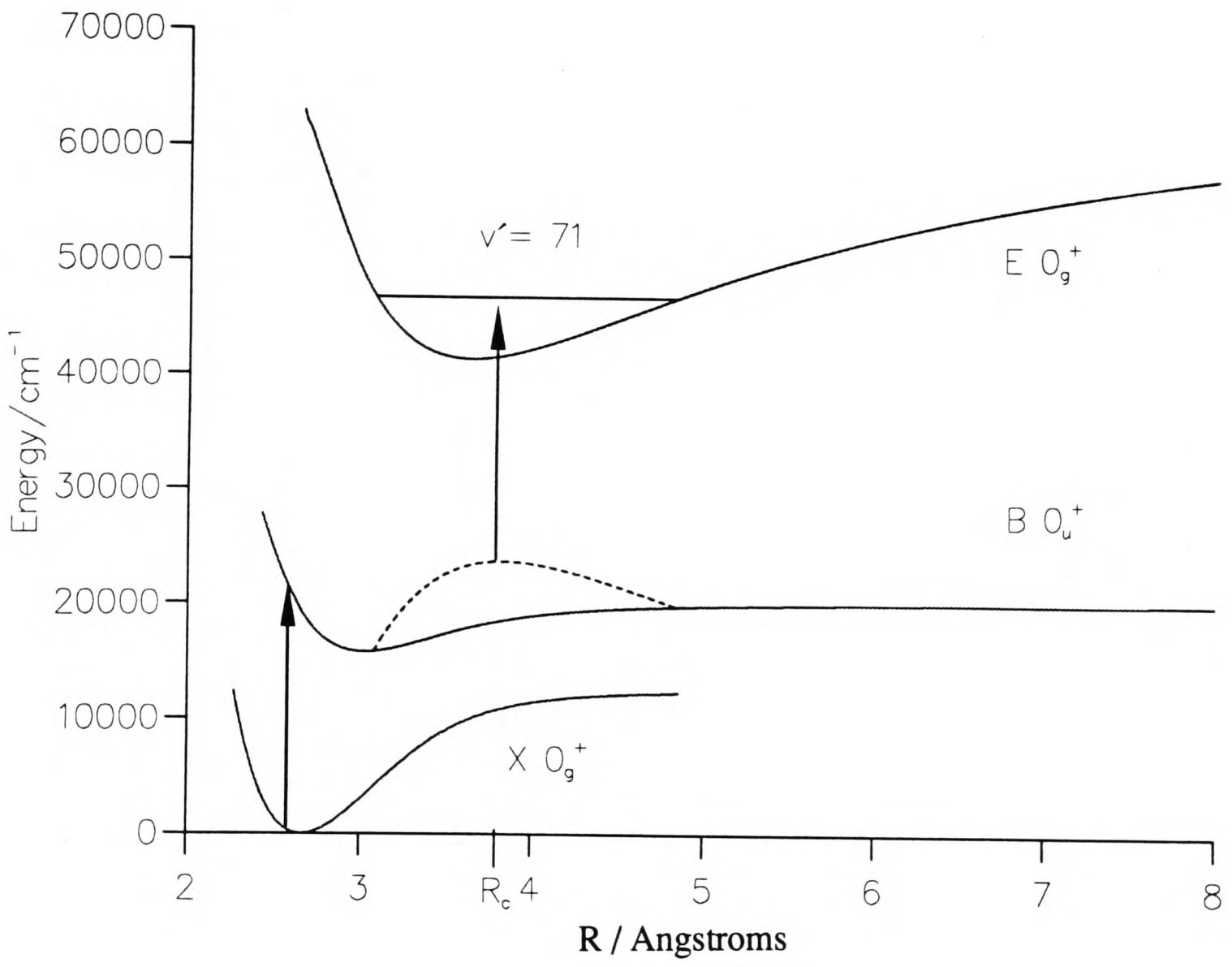

Figure 3–1: A diagram showing the potentials of $X0_g^+$, $B0_u^+$ and $E0_g^+$ states, with the Mulliken difference potential (...), $T_e(E)$ - $T_e(B)$ + $V_E(R)$ - $V_B(R)$ + $h\nu$ for the value of ν that just reaches the red extremum at R_c in a one-colour, two-photon experiment.

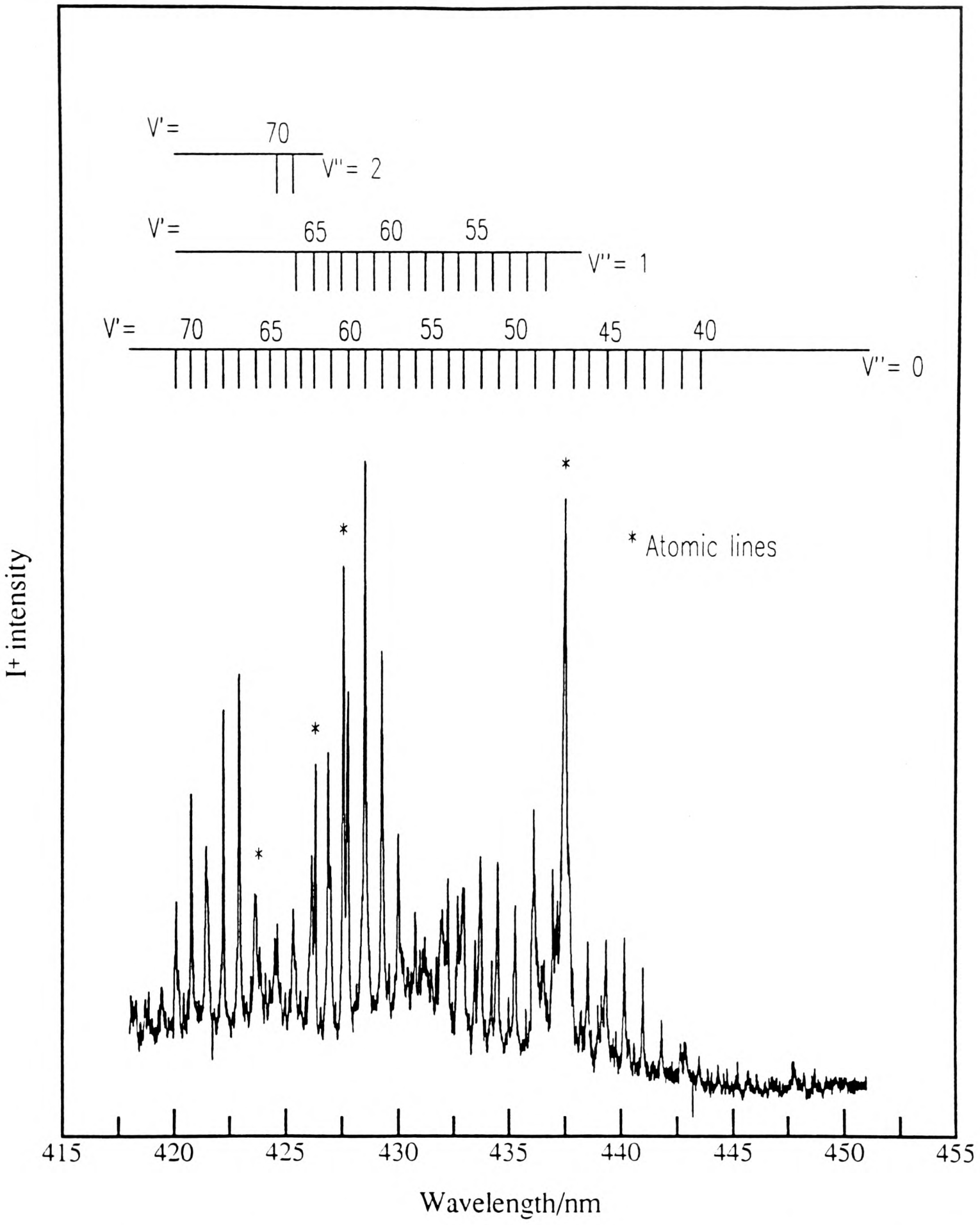

Figure 3–2: The (2+2) REMPI spectrum of I_2 as a function of a single photon wavelength. Atomic lines are starred. Vibrational levels of the $E0_g^+$ ion-pair state are assigned up to v′= 71.

v'',v'	$\bar{\nu}_{Obs}/cm^{-1}$	$\bar{\nu}_{Obs-Lit^{(a)}}/cm^{-1}$	v'',v'	$\bar{\nu}_{Obs}/cm^{-1}$	$\bar{\nu}_{Obs-Lit^{(a)}}/cm^{-1}$
40,0	45199.5	-2.4	60,0	46854.8	+2.1
41,0	45285.1	-1.9	63,1	46877.7	+3.7
42,0	45370.9	-2.5	61,0	46939.8	+8.1
43,0	45454.9	-3.5	64,1	46952.5	+0.6
44,0	45540.5	-2.8	62,0‡	47019.0	+8.8
45,0	45624.0	-3.8	65,1	47022.4	+7.1
46,0	45708.6	-3.3	66,1	47110.9	+4.2
47,0	45796.9	+1.2	69,2	47124.2	-0.3
48,0	45877.8	-1.2	70,2	47201.3	+0.8
49,0	45961.8	-0.3	66,0‡	47319.3	-1.9
52,1	45994.6	+0.1	67,0	47398.7	+0.5
50,0	46045.2	+0.4	68,0	47472.9	-1.9
53,1	46077.0	+0.7	69,0†	47559.1	+8.1
51,0	46127.2	+0.1	70,0†	47636.7	+9.7
54,1	46157.5	-0.1	71,0†	47711.9	+9.3
52,0	46212.6	+3.5			
55,1	46238.9	+0.3			
53,0	46291.8	+1.0			
56,1	46322.9	+3.7			
54,0	46371.4	-0.7			
55,0	46453.6	+0.5			
56,0	46531.8	-1.9			
57,0	46612.2	-1.7			
58,0	46692.2	-1.7			
59,0	46773.3	-0.2			

Table 3–1: Observed transition energies of the $E0_g^+$ ion-pair state of I_2.

(a) from Ref (7)

(‡) levels overlaped by atomic lines

(†) combination from v''= 0 and v''= 1 of the ground state.

($v' = 71$), where the turning points are 3.05 Å and 5.00 Å there is no Franck-Condon overlap, even with $v'' = 2$ of the $X0_g^+$ ground state, for which the corresponding turning points [8] are 2.56 and 2.79 Å. Thus vertical two-photon excitation is not possible and the two-photon sequential excitation steps must be considered.

3.4 Discussion

One of the features to be noticed in Figure (3.2), is the relatively short spectral region occupied by the progression, which covers the region 443 — 420 nm. The reason for this can be understood by consideration of the two-photon absorption steps involved. Firstly, the one-photon absorption spectrum of I_2 between 400 and 500 nm shows an onset at 420 nm and rises steadily to a maximum at 500 nm, where the dissociation limit of the $B0_u^+$ state lies. This system has been assigned by Tellinghuisen [9] to two components, $B''\,1_u \leftarrow X0_g^+$ and $B0_u^+ \leftarrow X0_g^+$. Secondly, by looking at the emission from the $E0_g^+$ state and locating the red extremum[1], it is possible to deduce which one of the two valence states acts as the resonant intermediate state. Emission from $v' = 0$ of the $E0_g^+$ state to the $B''1_u$ valence state appears at 347 nm with approximately 2% of the intensity of the emission to the B state [10]. The range of the $E0_g^+ \rightarrow B''1_u$ fluorescence is expected to extend both above and below 347 nm as the vibrational level of the $E0_g^+$ state increases. However, emission from $v' = 53$ of the $E0_g^+$ state shows only the $E0_g^+ \rightarrow B0_u^+$ system with its extremum at 440 nm [11]. A simulation of the $E0_g^+ \rightarrow B0_u^+$ emission from $v' = 71$ of the E 0_g^+ state is shown in Figure (3.3). From the simulation the red extremum is around 440 nm, in agreement with the value obtained experimentally by Rousseau and Williams [11]. The potential curves used in the simulation were

---

[1]The red extremum corresponds to the maximum in the $E0_g^+ \rightarrow$ (repulsive) intermediate emission system and thus to an extremum in the Mulliken difference potential (see Figure (3.3)).

obtained from References [12] and [13], for the $E0_g^+$ and $B0_u^+$ states, respectively. Hence it is the $B0_u^+$ state that must be acting as the intermediate state in this case.

The oscillatory appearance of the spectrum is expected to be a common feature if a continuum state is used in a sequential excitation scheme. The overall two-photon cross section is the product of the one-photon cross section for accessing the intermediate state, $\sigma_{B\leftarrow X}(\nu)$ and that for the second step, $\sigma_{E\leftarrow B}(\nu)$. In the scheme $E0_g^+ \leftarrow B0_u^+ \leftarrow X0_g^+$, there is relatively little overlap in the frequency domain between these two cross sections. The first oscillation of the Airy-like envelope of the $E0_g^+ \rightarrow B0_u^+$ fluorescence lies between 417 and 438 nm as shown in Figure (3.3). The $B0_u^+ \leftarrow X0_g^+$ absorption starts at $\sim$ 420 nm and peaks at $\sim$ 500 nm [9], therefore the limited region of sequential two-photon excitation that we have observed is accounted for.

Another way in which the REMPI spectrum in Figure (3.2) differs from the dispersed fluorescence spectrum of the reverse bound $\rightarrow$ free transition is in the interference structure beneath the broader oscillations of the envelope. In the REMPI spectrum (Figure (3.2)) three broad oscillations can be seen, with minima between them at 424.5 and 431.5 nm. In the same wavelength range in the $E_{(v'=71)}$ $\rightarrow$ B fluorescence, six such ocillations are observed in the simulation shown in Figure (3.3). The reason for this change in structure is simply that in the present experiment both $B0_u^+$ and $E0_g^+$ state energies increase with the photon energy, the latter at twice the rate of the former. A simple semi-classical analysis shows the overall intensity is proportional to $\sqrt{\mu}$ at constant ν, reflecting the transit time in the dissociating state through the Franck-Condon region of the red extremum. From these points of view, the $E0_g^+ \leftarrow B0_u^+ \leftarrow X0_g^+$ system in iodine is not ideal and only the large reduced mass criterion is favourable. The $B0_u^+ \leftarrow X0_g^+$

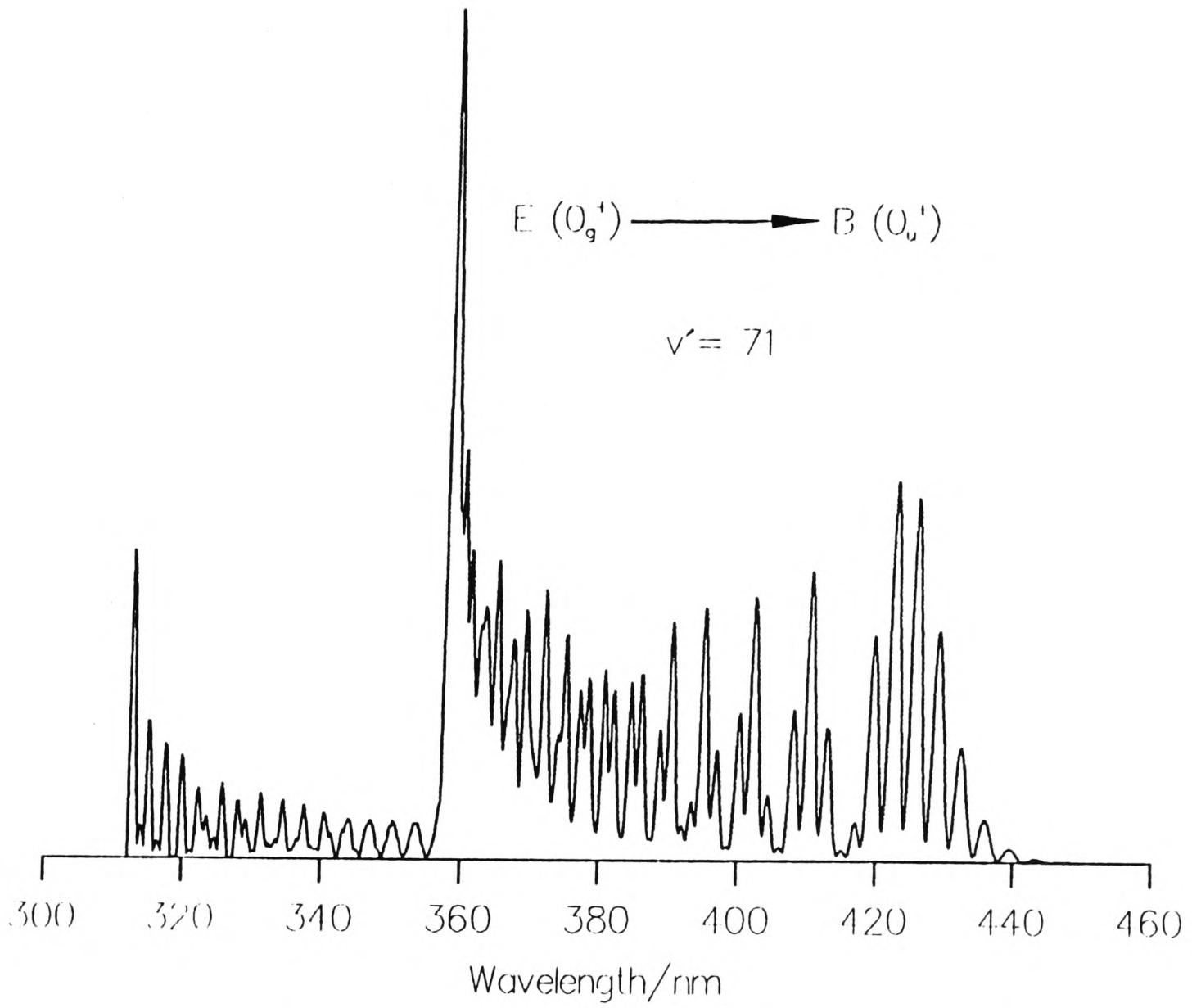

Figure 3–3: A simulation of the emission of the $E(0_g^+) \rightarrow B(0_u^+)$, from v′= 71 of the E state. Showing the red extremum at 440 nm.

transition is inherently weak, being essentially spin forbidden and there is overlap between $\sigma_{E\leftarrow B}(\nu)$ and $\sigma_{B\leftarrow X}(\nu)$ only in the tail of the $B0_u^+ \leftarrow X0_g^+$ absorption. It is therefore encouraging that the spectrum can be detected fairly easily and leads us to suggest that dissociative intermediate states might be generally useful near the red extremum of a particular final transition. The overlap between the two absorption cross sections is much improved, for instance, in ICl and IBr.

It is now interesting to re-examine the work carried out by Kasatani et al.[1]. They have shown in their work on repulsive intermediate states of I_2, that when the excitation wavelength is above the dissociation limit of the $B0_u^+$ $\lambda_{ex}\langle$ 498.9 nm, three emission bands are observed, at 342 nm, 325 nm, and 287 nm. They interpreted the 342 nmn emission band as due to the $D'2_g$ state in the excitation scheme $D'2_g \leftarrow B''1_u \leftarrow X0_g^+$. The $D'2_g$ state lies in the first cluster of the ion-pair states of I_2, and can be energetically accessed at an excitation wavelength of 460 nm for a two-photon process. Having considered the selection rules, three possible ion-pair states could be accessed via either the $B''1_u$ or $B0_u^+$ state, i.e the $E0_g^+$, $\beta 1_g$, and the $D'2_g$ states from the first cluster. However, in a vertical two-photon transition, with a photon wavelength of 460 nm, no ion-pair states could be accessed, due to the limitation of the Franck-Condon factors from the $v'' = 0$ of the ground state. No strong emission has been seen from those three states to the $B''1_u$ state, only the weak $E0_g^+ \rightarrow B''1_u$ emission at 347 nm [10]. Hence the reverse process is unlikely. In the present work no ion-pair levels were observed above 450 nm. Therefore the above three states can not be accessed via the $B''1_u$ state. As a result this process can not be a (1+1) two-photon transition process. The most likely explanation is three-photon (1+2) excitation. The second two-photon step, via a virtual intermediate state, can explain their square power dependency. A possible interpretation of the three emission bands, that Kasatani et al.[1] have observed is that the 342 nm band was due to the $\delta 2_u \rightarrow 2_g$ and $\gamma 1_u \rightarrow$ a 1_g emission systems. The 325 nm and 287 nm emission bands were due to the $D0_u^+ \rightarrow X0_g^+$ and $H1_u \rightarrow$ a 1_g emission systems, respectively. All the above emission systems have been re-examined recently [10].

3.5 Conclusion

It has been shown that in a one-colour experiment the low levels of the $E0_g^+$ ion-pair state can be accessed via the repulsive wall of the $B0_u^+$ state. However, the method is restricted in one-colour experiments. To be able to access higher vibrational levels, the laser wavelength needed to be scanned to shorter wavelengths, which inevitably would lead to a region outside the prominent red extremum. A two-colour experiment would be more effective: the first photon wavelength could then be tuned to optimise the first transition by working near the maximum of $\sigma_{i\leftarrow X}(\nu)$ and the second colour selected to lie in the region of the red extremum of the conjugate bound $\rightarrow$ free emission. Provided that the second step has a reasonably strong transition dipole and exhibits a red extremum, this might prove to be an almost universal approach to accessing states with large equilibrium separations, thereby expanding the scope of the optical double resonance technique.

3.6 References

(1) K. Kasatani, Y. Tanaka, K. Shibuya, M. Kawasaki, K. Obi, H. Sato and I. Tanaka, J. Chem. Phys., 74 (1981) 895.

(2) M.E. Koch, W.C. Stwalley, and C.B. Collins, Phys. Rev. Letts., 42 (1979) 1052.

(3) M.A. Young, J. Phys. Chem., 97 (1993) 13508.

(4) L. Li, R.J. Lipert, H. Park, W.A. Chupka and S.D. Colson, J. Chem. Phys., 88 (1988) 4608.

(5) L. Bigio and E.R. Grant, J. Chem. Phys., 83 (1985) 5361.

(6) A. Strobel, A. Lochschmidt, I. Fischer, G. Niedner-Schatteburg and V.E. Bondybey, J. Chem. Phys., 99 (1993) 733.

(7) J.C.D. Brand, A.R. Hoy, A.K. Kalkar and A.B. Yamashita, J. Mol. Spect., 95 (1982) 350;

(8) F. Martin, R. Bacis, S. Churassi and J. Verges, J. Mol. Spect., 116 (1986) 71.

(9) J. Tellinghuisen, J. Chem. Phys. 58 (1973) 2821.

(10) K.P. Lawley, P.J. Jewsbury, T. Ridley, P.R.R. Langridge-Smith and R.J. Donovan, Mol. Phys., 75 (1992) 811.

(11) D.L. Rousseau and P.F. Williams, Phys. Rev. Letts., 33 (1974) 1368.

(12) P.J. Wilson, Ph.D. thesis, University of Edinburgh, 1994.

(13) P.J. Jewsbury, Ph.D thesis, University of Edinburgh, 1991.

Chapter 4

One-colour Sequential Excitation of the $D0_u^+(^3P_2)$, $F0_u^+(^3P_0)$ and $F'0_u^+(^1D_2)$ Ion-pair States of Cl_2 *Via* the Continuum of the $B0_u^+$ State

4.1 Introduction

Although the electronic states of Cl_2 have been studied extensively, relatively little is known about the *ungerade* ion-pair states. Ishiwata et al.[1], using a sequential optical optical double resonance (OODR) technique, have carried out extensive work on Cl_2, particularly on the ion-pair states of *gerade* symmetry. However, one of their earliest works, using the OODR technique *via* the bound levels of the $B0_u^+$ state, was the characterisation of three *ungerade* ion-pair states, with T_e values around 59000 cm^{-1} and R_e values of $\sim$ 2.9 Å. The three states, labeled α, β and γ were assigned as the 0_u^+ components of the $^3\Sigma_u^+(^3P_2)$, $^3\Pi_u(^3P_0)$, and $^1\Sigma_u^+(^1D_2)$ configurations, respectively [2]. Peyerimhoff and Buenker [3], in their *ab initio* calculations of the electronically excited, and ionised states of Cl_2, predicted that the $^1\Sigma_u^+(^1D_2)$ state should have an avoided crossing around 14000 cm^{-1} above T_e, with a $4p$ Rydberg state at an internuclear distance of $\sim$ 2.0 Å. One-photon absorption studies using a variety of excitation sources and experimental techniques [4-7], confirmed this avoided crossing. Wörmer et al.[6], obtained a simulation of the dispersed fluorescence from the $^1\Sigma_u^+(^1D_2)$ double-minimum potential, which suggested that the previous assignment of the γ progression by Ishiwata et al.[2], was no longer valid. Recently, Ishiwata et al.[8], have reassigned the β and γ states and this will be discussed in the results section of this chapter. Throughout this chapter the α $^3\Sigma_{0_u^+}^-$, β $^3H_{0_u^+}$ and the γ $^1\Sigma_{0_u^+}^+$ ion-pair states, will be designated as $D0_u^+(^3P_2)$, $F0_u^+$ $(^3P_0)$ and $F'0_u^+(^1D_2)$, respectively, correlating with the labels given to the equivalent states of I_2.

In the previous chapter, the (1+1) two-photon excitation of the $E0_g^+$ ion-pair state of I_2, via the continuum of the intermediate $B0_u^+$ state was discussed. Here in this chapter, in a (1+2) three-photon excitation, the same method was applied, whereby, the 0_u^+ components of the $D(^3P_2)$, $F(^3P_0)$ and the $F'(^1D_2)$ ion-pair states of Cl_2 were accessed, *via* the continuum of the intermediate $B0_u^+$ state. Also the

strong interaction between the $F0_u^+(^3P_0)$ and $F'0_u^+(^1D_2)$ ion-pair states, and the weak interaction between the $D0_u^+(^3P_2)$ and $F0_u^+(^3P_0)$ states are discussed.

4.2 Experimental

The experimental setup is described in detail in chapter two. In this work, the output radiation between 480 and 410 nm was obtained, using the dyes Coumarin 47, Coumarin 120, and Stilbene 3. The molecular beam of Cl_2 in He was generated by pulsing $\sim$ 760 Torr of 5% Cl_2 in He through the nozzle.

All spectra were recorded by collecting the signal in either the $^{35}Cl^+$ or $^{37}Cl^+$ mass channels, no $^{35}Cl_2^+$ signal was observed. Thus the $^{35}Cl^+$ spectrum included bands from $^{35}Cl_2$ and $^{35}Cl\,^{37}Cl$, while the $^{37}Cl^+$ spectrum included those from $^{35}Cl\,^{37}Cl$ and $^{37}Cl_2$. The two spectra were recorded simultaneously with separate boxcars, and by subsequent subtraction of the $^{37}Cl^+$ signal from the $^{35}Cl^+$ signal, the pure $^{35}Cl_2$ spectrum was obtained. The small negative dips in the resulting spectrum are due to $^{37}Cl_2$. The laser wavelength was calibrated from the optogalvanic signal of a neon-filled hollow cathode lamp.

4.3 Results

4.3.1 General Considerations

The one-photon absorption spectrum of Cl_2 is attributed to the $B0_u^+ \leftarrow X0_u^+$ and $C1_u \leftarrow X0_u^+$ absorption systems [9]. Absorption to the $C1_u$ state covers the region 250 - 420 nm, with a maximum at 330 nm. Absorption to the $A1_u$ state, above its dissociation limit, has not been reported but the bound region of this state was analysed by Ishiwata et al.[10]. The dissociation limit of the $A1_u$ state can be estimated to be around $\sim$ 500 nm. The very weak $A1_u \leftarrow X0_u^+$ absorption system should start at longer wavelengths and extend down to 350 nm, overlaping with

the much stronger $B0_u^+ \leftarrow X0_u^+$ absorption system. The dissociation limit of the B state ocurrs around 480 nm (20800 cm^{-1}) and the $B0_u^+ \leftarrow X0_g^+$ absorption system covers the region 350-480 nm, with a maximum at 450 nm [9], corresponding to three-photon energies of 62500 - 85700 cm^{-1}. In this energy range the ion-pair states that dissociate to $Cl^+(^3P_{2,1,0}) + Cl^-(^1S_0)$ and $Cl^+(^1D_2) + Cl^-(^1S_0)$ are energetically accessible. Although the two-photon $0_u^+ \leftarrow\leftarrow 0_u^+$ transition from the continuum of the $B0_u^+$ state to the final state may have a large two-photon cross-section, single photon emission from the final state back to the $B0_u^+$ state is parity forbidden. However, a good estimate of the emission frequency can be obtained by considering the allowed $E0_g^+ \rightarrow B0_u^+$ emission, which has a red extremum around 260 nm [11]. This suggests that it should be possible to excite the $0_u^+ \leftarrow\leftarrow B0_u^+$ step with two photons of less than 520 nm, see Figure (4.1). The wavelength range actually used is below the red extremum since photons of 520 nm would result in the bound levels of the $B0_u^+$ state, which has a dissociation limit around 480 nm, being excited which could complicate the spectra.

4.3.2 General Features

The (1+2) excitation spectrum of jet-cooled $^{35}Cl_2$ in the three-photon energy range of 62500 - 72800 cm^{-1} (corresponding to one-photon laser wavelengths of 480 - 412 nm) is shown in Figure (4.2). Despite using a repulsive intermediate state which has a short lifetime and the inherent weakness of the coherent two-photon probe transition, strong ion signals with a good signal-to-noise ratio are observed, especially at the low energy end of the spectrum. From Figure (4.2) the spectrum shows a general trend, with the signals becoming weaker to shorter wavelength. Although the spectrum is not power normalised, the intensities of the bands around 72000 cm^{-1} are less than a tenth of those around 63000 cm^{-1}. One explanation for the fall in intensity with increasing energy is partly due to absorption by

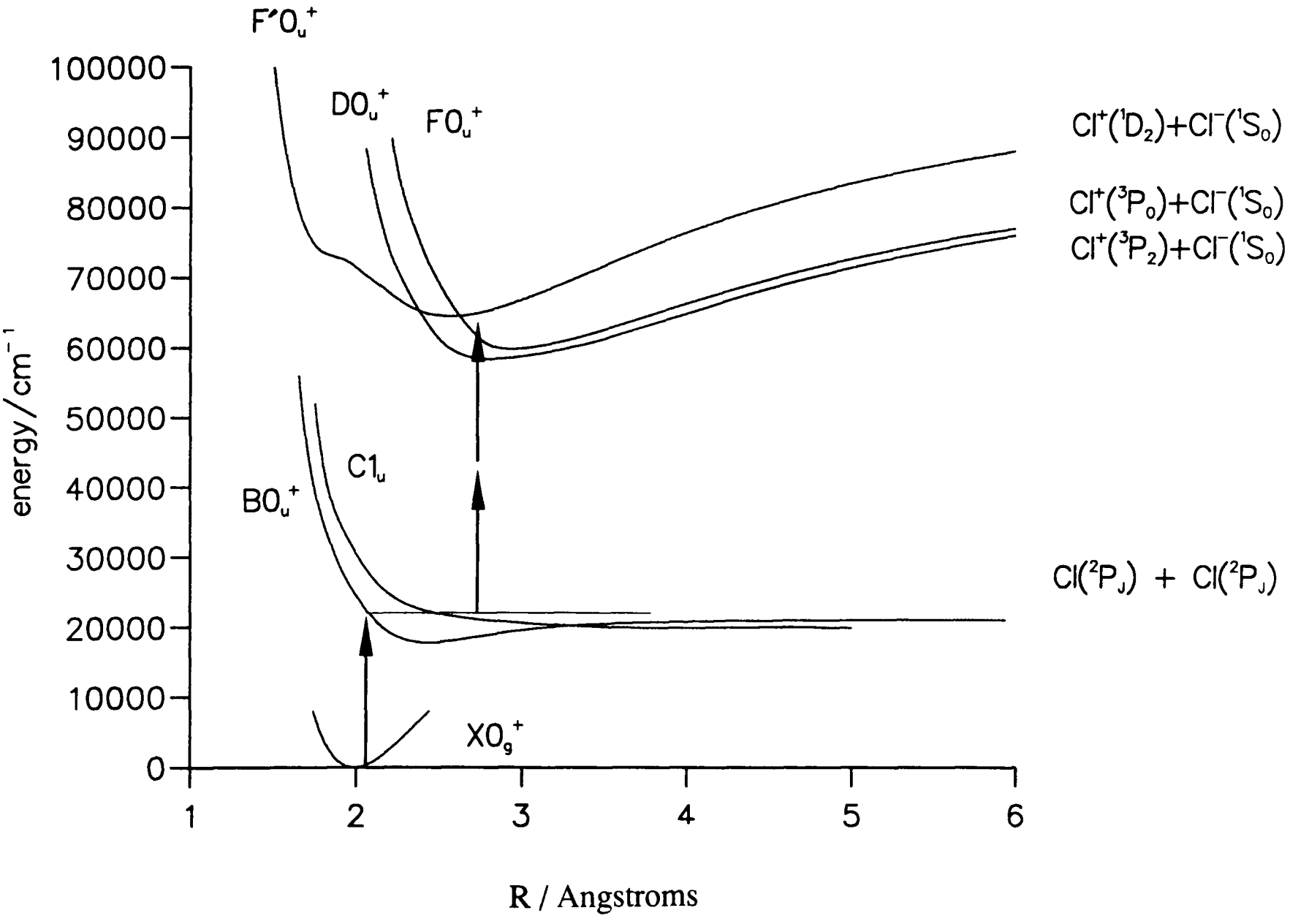

Figure 4–1: Potential energy curves for Cl_2 showing the (1+2) excitation scheme used in this work.

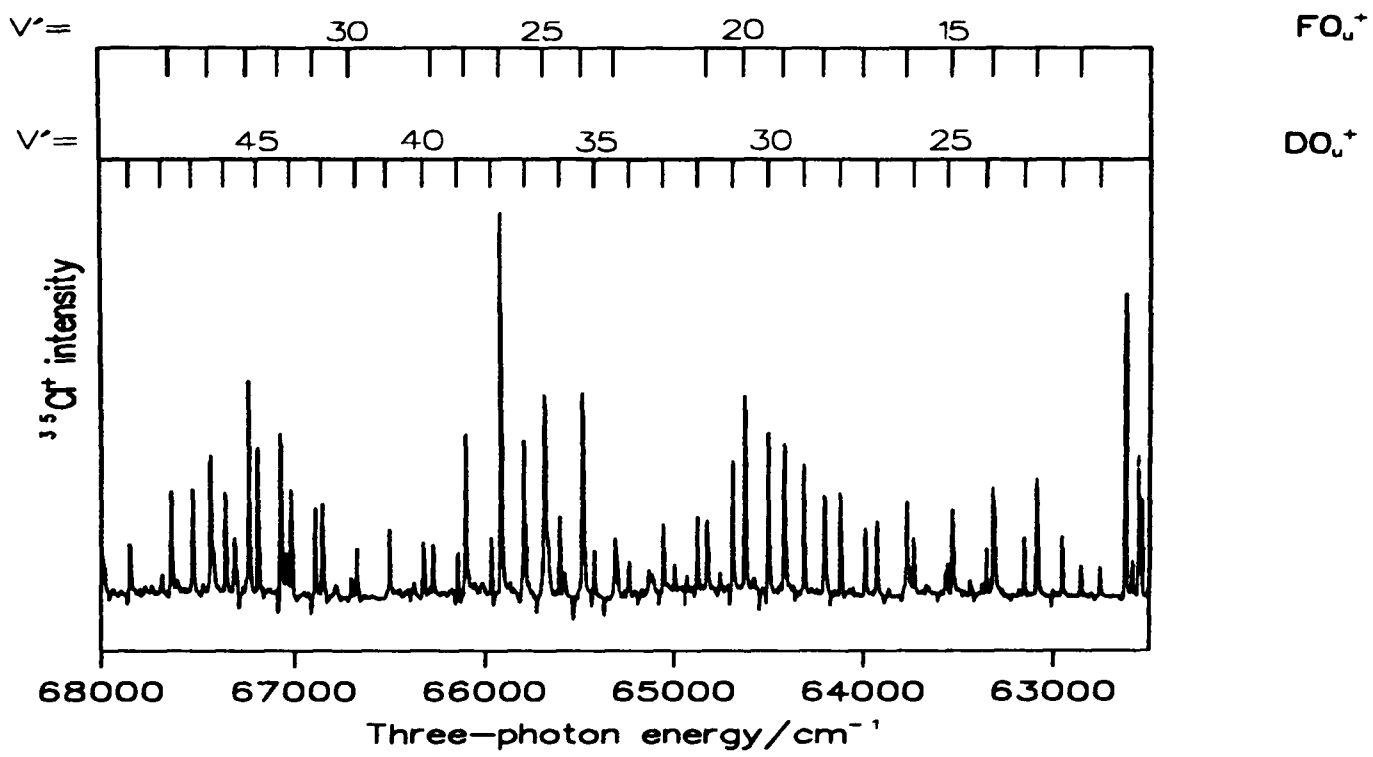

Figure 4–2: One-colour (1+2) excitation spectrum of $^{35}Cl_2$ covering the region 62500 - 72500 cm^{-1}, showing the $D0_u^+(^3P_2)$ and the $F0_u^+(^3P_0)$ ion-pair state progressions.

B $\leftarrow$ X being replaced by absorption to a second state becoming significant at the one-photon level. Maric et al.[9]. determined that absorption to the purely repulsive $C1_u$ state begins at 450 nm, which is equivalent to 66700 cm^{-1} at the three-photon level. This absorption becomes equal to that of the B state at 420 nm, corresponding to 71400 cm^{-1} at the three-photon level, and dominates the spectrum at shorter wavelengths. At the wavelengths studied here the $C1_u$ state does not appear to act as an intermediate to any ion-pair states, as will be discussed later. Rather, absorption to it removes a significant fraction of the ground state molecules which would otherwise have taken the *ion-pair* $\leftarrow B0_u^+ \leftarrow X0_g^+$ pathway, resulting in a loss of ion signal. Another reason for the fall in intensity is that in the probe step, as the exciting photon moves to shorter wavelength, away from the red extremum region, a drop in intensity is expected. Furthermore the ion signal decreases more sharply, as the spectrum moves to shorter wavelengths, because the 'lifetime' of the continuum intermediate state, which in the present experiments can be taken as the transit time through the region of the stationary phase in the overlap of the continuum and final state wave functions, becomes shorter. Below 62700 cm^{-1} strong signals were observed due to transition to the bound levels of the $B0_u^+$ state.

Three transitions due to power broadened (3+2) resonances in atomic chlorine are starred in Figure (4.2).

4.3.3 Vibrational Analysis

The spectrum in Figure (4.2) is dominated by two progressions of ion-pair state vibrational levels having spacings of ≤ 200 and ≤ 232 cm^{-1}. Although the 0_u^+, 1_u and 2_u states can be accessed *via* two-photon absorption from the $B0_u^+$ state, the parallel $0_u^+ \leftarrow\leftarrow 0_u^+$ transition, with no change in spin orientation, would be expected to have the greatest transition strength. Using polarisation data, Ishiwata et al.[2]. have confirmed this by showing, the states accessed *via* the bound levels of the $B0_u^+$ state, have 0_u^+ symmetry. In their work they observed three progressions which they labelled α, β and γ, and assigned them as $^3\Sigma^-_{0_u^+}$, $^3\Pi_{0_u^+}$ and

$^1\Sigma^+_{0^+_u}$, respectively, the α and γ states having ω_e and $\omega_e x_e$ values of 234 cm^{-1}, 2.2 cm^{-1} and 283 cm^{-1}, 2.2 cm^{-1}, respectively. The β state appeared to be perturbed, having a very low ω_e value for an ion-pair state of Cl_2 of 206 cm^{-1} and a negative $\omega_e x_e$ of -0.7 cm^{-1}. In Figure (4.2) the two progressions observed were correlated with the α and γ states obtained by Ishiwata et al.[2], starting from $v' = 21$ and $v' = 12$, respectively.

Although the Rydberg/ion-pair interactions, predicted by Peyerimhoff and Buenker [3], are expected at smaller R, the form of the ion-pair potentials at large R is still expected to be largely defined by the ion-pair dissociation products. In Cl_2 the energies of the Cl^+ cation are in the order $^3P_2$ (ground state), $^3P_1$ (697 cm^{-1}) and $^3P_0$ (996 cm^{-1}), and the splitting energy ΔE ($^3P_2$ - $^1D_2$) is $\sim$ 11000 cm^{-1} [1]. Therefore the ion-pair states should have T_e values approximately separated by the energies of the dissociation products.

The spectrum in Figure (4.2) is divided into two parts, above and below 64500 cm^{-1}. Figure (4.3) covers an energy region 62500 - 64500 cm^{-1}. As shown the vibrational spacings of the two states are quite different in this region, however occasional near coincidence is expected, for instance between $v' = 25$ of the $D0^+_u(^3P_2)$ state and $v' = 15$ of the $F0^+_u(^3P_0)$ state, an interaction takes place, resulting in both bands being shifted by upto 10 cm^{-1}.

Vibrational levels above 64500 cm^{-1} for the the $D0^+_u(^3P_2)$ state are assigned upto $v'= 60$ (69500 cm^{-1}) with no shift more than 10 cm^{-1}, the only interaction

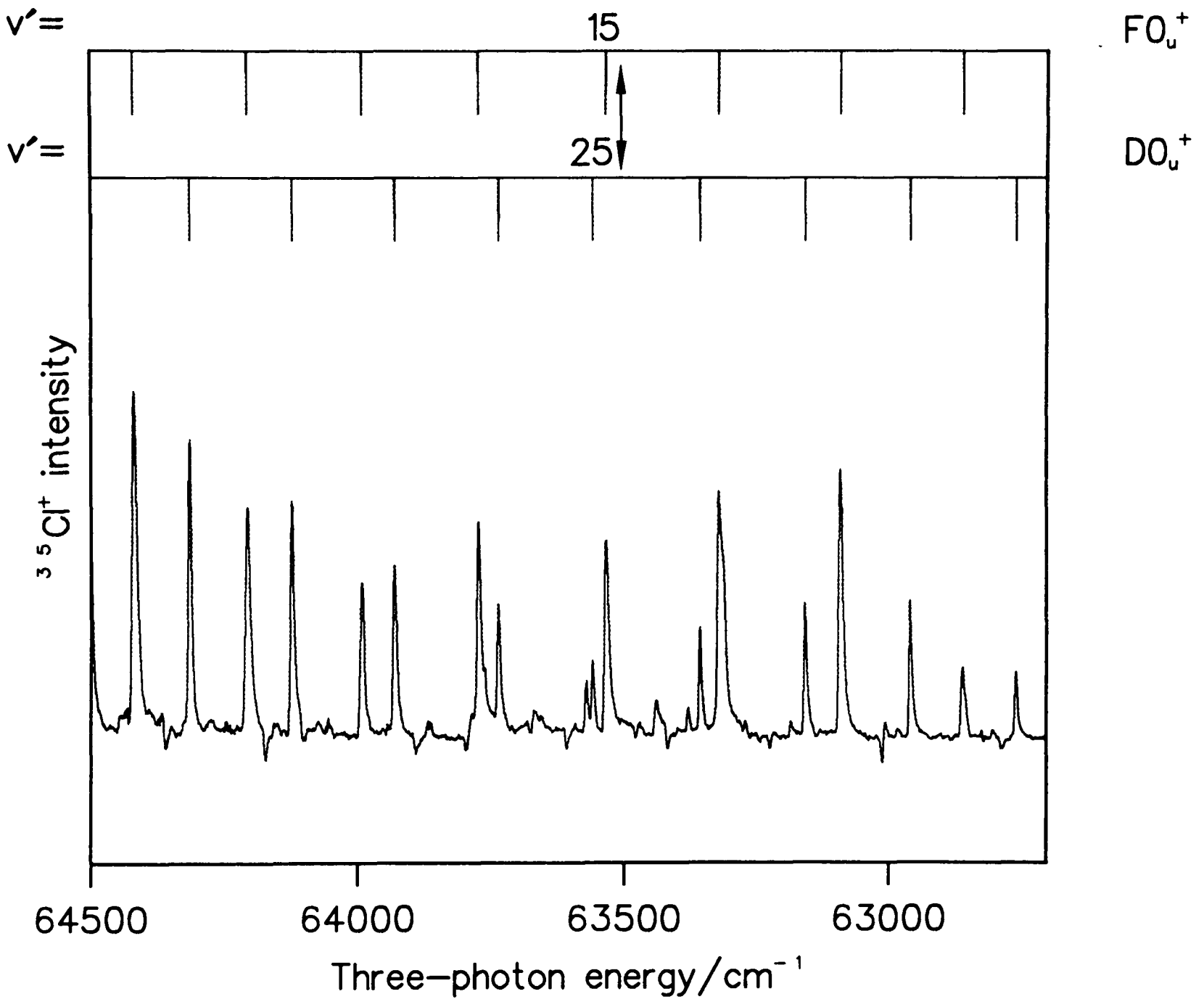

Figure 4–3: One-colour (1+2) excitation spectrum of $^{35}Cl_2$, between 62800 - 64500 cm^{-1}, showing the interaction bteween v′ = 25 of the $D0_u^+(^3P_2)$ state and v′ = 15 of the $F0_u^+(^3P_0)$ state.

appears to be with the $F0_u^+(^3P_0)$. Nevertheless, above 69000 cm^{-1}, shifts in the observed band positions are larger, indicating strong interaction with either the same state or the ion-pair state is interacting with a $4p$ Rydberg state. However, quantum defect calculations predict that the lowest $4p$ Rydberg will occur around 73000 cm^{-1}; therefore, the latter explanation can be excluded. Tables (4.1) and (4.2) show transition energies of the $^{35}Cl_2$ and $^{35}Cl^{37}Cl$ isotopes, for the $D0_u^+(^3P_2)$ state. The $F0_u^+(^3P_0)$ ion-pair state vibrational levels show irregular spacings above 65000 cm^{-1}. However, extra bands are seen which do not fit into the assignments for either the $F0_u^+(^3P_0)$ or the $D0_u^+(^3P_2)$ states. It is concluded that these extra bands are due to a crossing of the $F0_u^+(^3P_0)$ potential curve with that of the $F'0_u^+(^1D_2)$ potential near its minimum, as predicted by Peyerimhoff and Buenker [3], and shown in Figure (4.1). The T_e for the $F'0_u^+(^1D_2)$ state was estimated by Wörmer et al.[6]. from a simulation of the dispersed fluorescence, and showed that the $F'0_u^+(^1D_2)$ potential will cross both triplet states, rather than being nested with them as is the usual case. The interactions show two main features. Firstly, the three $F0_u^+(^3P_0)$ vibrational levels immediately below the crossing, v′ = 20, 21, and 22, are pushed down in energy. Secondly, the position of some of the levels, v′ = 23-63, are shifted by upto 30 cm^{-1}. Close to most of the heavily perturbed levels there is a band of medium to weak intensity which is not due to the $D0_u^+(^3P_2)$ state. These are assigned to $F'0_u^+(^1D_2)$ vibrational levels which borrow intensity through homogeneous interaction with the $F0_u^+(^3P_0)$ state. This is illustrated in Figure (4.4). Tables (4.3) and (4.4) give the transition energies of the $F0_u^+(^3P_0)$ state, for both isotopes $^{35}Cl_2$ and $^{35}Cl^{37}Cl$, respectively. In the high resolution one-photon vacuum-UV absorption spectrum obtained by Douglas [4], strong transitions were observed to the $F'0_u^+(^1D_2)$ state. Some of these bands were doublets and showed perturbed rotational contours. Wörmer et al.[6], attributed these features to an interaction with one of the triplet ion-pair states. Here in this work no unperturbed $F'0_u^+(^1D_2)$ vibrational levels were seen.

Using the vibrational numbering obtained by Wörmer et al.[6], observed in one-photon absorption, in the energy region of overlap of the two sets of data, three perturbed levels, v′ = 22, 29, and 31 are seen. They appear as doublets at

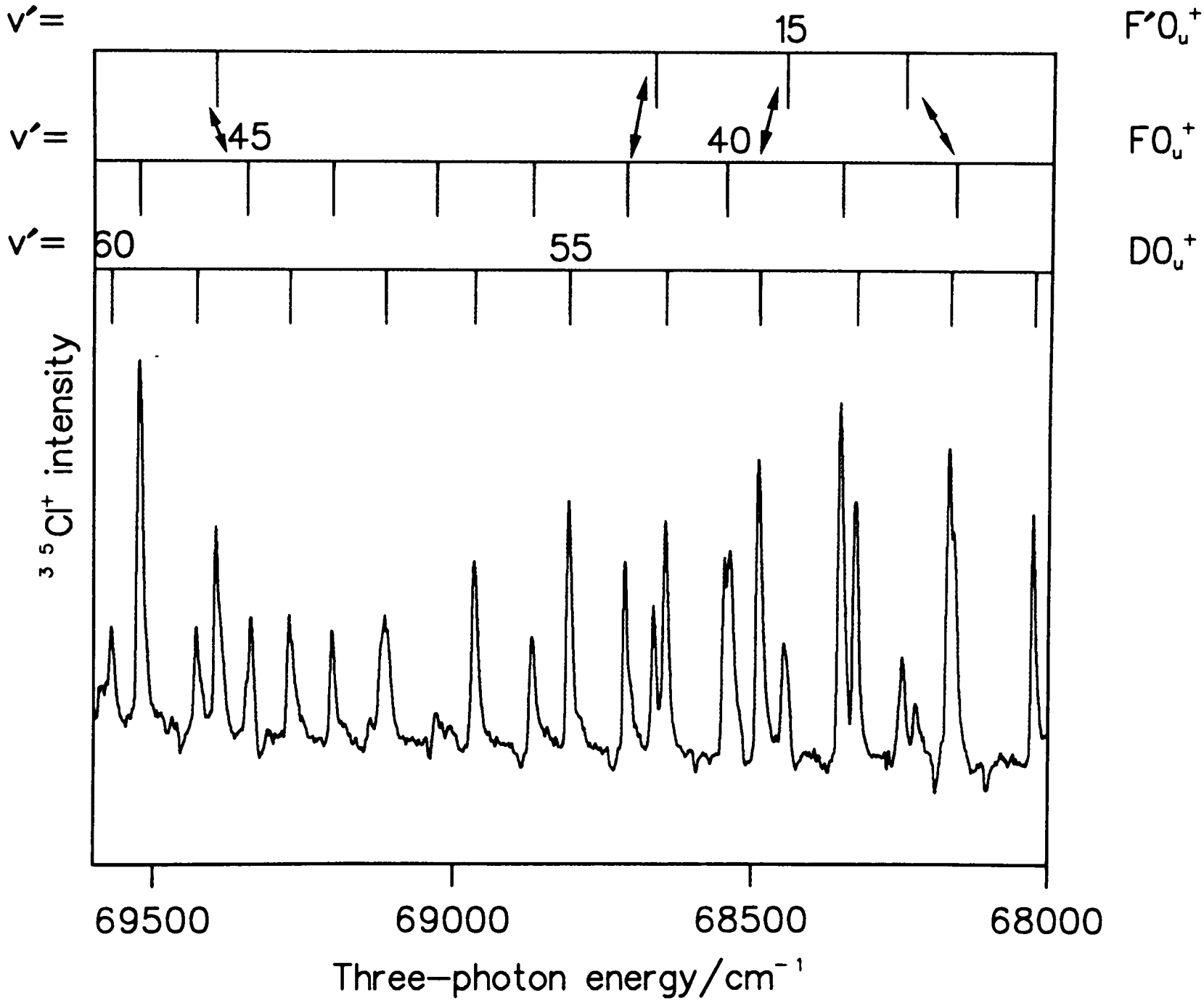

Figure 4–4: One-colour (1+2) excitation spectrum of $^{35}Cl_2$ between 68000 - 69600 cm^{-1}, showing the assignments of the vibrational levels of the $F'0_u^+(^1D_2)$ state, the arrows showing the interaction with the $F0_u^+(^3P_0)$ state.

v′	$\bar{\nu}_{obs}/\mathrm{cm}^{-1}$	$\bar{\nu}_{o-c}/\mathrm{cm}^{-1}$	v′	$\bar{\nu}_{obs}/\mathrm{cm}^{-1}$	$\bar{\nu}_{o-c}/\ \mathrm{cm}^{-1}$	v′	$\bar{\nu}_{obs}/\mathrm{cm}^{-1}$	$\bar{\nu}_{o-c}/\mathrm{cm}^{-1}$
1†	58555	-1	38	65964	-1	65	70310	6
2†	58780	0	39	66144	1	67	70584	-7
3†	59000	0	40	66321	3	68	70734	2
4†	59219	2	41	66498	5	69	70864	-7
5†	59429	-3	42	66662	-4	71	71148	2
6†	59649	3	43	66841	3	72	71283	2
7†	59857	-1	44	67003	-5	74	71549	0
8†	60070	0	45	67177	0	75	71686	3
21	62755	0	46	67344	-1	76	71814	-3
22	62953	-1	47	67514	3			
23	63153	1	48	67674	-2			
24	63352	3	49	67840	0			
25	63554*	10	50	68015*	12			
26	63734	-4	51	68158	-6			
27	63929	-2	52	68315	-9			
28	64121	-1	53	68478	-5			
29	64312	0	54	68635	-6			
30	64502	1	55	68797	-1			
31	64691	2	56	68955	2			
32	64877	2	57	69106	-2			
33	65057	-3	58	69265	4			
34	65235	-9	59	69417	3			
35	65424	-2	60	69560	-5			
36	65605	-2	62	69881*	13			
37	65785	-2	63	70027*	15			

Table 4–1: Observed and observed - calculated transition energies of the $D0_u^+(^3P_2)$ ion-pair state of $^{35}Cl_2$.

(†) from Reference (2).

Asterisks are values omitted from the fit.

v′	$\bar{\nu}_{obs}/\mathrm{cm}^{-1}$	$\bar{\nu}_{o-c}/\mathrm{cm}^{-1}$	v′	$\bar{\nu}_{obs}/\mathrm{cm}^{-1}$	$\bar{\nu}_{o-c}/\ \mathrm{cm}^{-1}$
2†	58777	0	43	66738	-2
3†	58994	1	44	66911	2
4†	59210	2	45	67079	2
5†	59414	-2	47	67404	-4
6†	59631	-1	48	67575	3
21	62699	-1	49	67741	7
22	62897	0	50	67900	5
23	63095	2	51	68048	-7
24	63293	6	52	68211	-3
25	63476	-4	53	68380	9
26	63670	-2	54	68526	-2
27	63862	-1	55	68686	3
28	64052	0	56	68836	-2
29	64240	0	57	68992	1
30	64429	2	58	69151	8
31	64618	6	59	69299	4
32	64803	6	61	69610*	16
33	64981	1	62	69765*	23
34	65157	-5	66	70309*	-13
35	65338	-4	67	70464	0
36	65519	-2	68	70621*	16
37	65697	-2	69	70743	0
39	66056	4			
40	66233	7			
42	660574	4			

Table 4–2: Observed and observed - calculated transition energies of the $D0_u^+(^3P_2)$ ion-pair state of $^{35}Cl^{37}Cl$.

(†) from Reference (2).

Asterisks are values omitted from the fit.

v′	$\bar{\nu}_{obs}/\mathrm{cm}^{-1}$	$\bar{\nu}_{o-c}/\mathrm{cm}^{-1}$	v′	$\bar{\nu}_{obs}/\mathrm{cm}^{-1}$	$\bar{\nu}_{o-c}/\ \mathrm{cm}^{-1}$	v′	$\bar{\nu}_{obs}/\mathrm{cm}^{-1}$	$\bar{\nu}_{o-c}/\mathrm{cm}^{-1}$
0†	59789	1	32	67057	-6	60	71725*	31
1†	60065	-3	33	67223*	-27	61	71848*	11
2†	60340	-1	34	67421*	-15	63	72115	0
3†	60611	1	35	67626	7	64	72247	-2
5†	61134	0	38	68149	-9			
6†	61387	-2	39	68340	6			
7†	61642	1	40	68536*	27			
12	62855	4	41	68703*	22			
13	63087	3	42	68857	5			
14	63315	1	43	69019	-3			
15	63530*	-12	44	69193	3			
16	63771	3	45	69335*	-21			
17	63990	-1	46	69513	-9			
18	64205	-7	47	69689	4			
19	64418*	-12	48	69837*	-11			
20	64626*	-20	49	69984*	-25			
21	64825*	-34	50	70186*	17			
23	65309*	29	51	70336	8			
24	65485	-2	53	70645	3			
25	65684	-8	54	70802	5			
26	65916*	22	55	70951	1			
27	66101	7	56	71092*	-10			
28	66272*	-20	57	71245	-8			
30	66688	6	58	71399	-3			
31	66879	6	59	71570*	21			

Table 4–3: Observed and observed - calculated transition energies of the $F0_u^+(^3P_0)$ ion-pair state of $^{35}Cl_2$.

(†) from Reference (2).

Asterisks are values omitted from the fit.

v′	$\bar{\nu}_{obs}/\mathrm{cm}^{-1}$	$\bar{\nu}_{o-c}/\mathrm{cm}^{-1}$	v′	$\bar{\nu}_{obs}/\mathrm{cm}^{-1}$	$\bar{\nu}_{o-c}/\ \mathrm{cm}^{-1}$
0†	59792	1	33	67151*	-18
1†	60064	-1	34	67350	-3
2†	60337	-1	35	67552*	17
3†	60603	-2	37	67884	-9
5†	61116	-2	38	68068	-1
12	62816	1	39	68257*	13
13	63046	1	40	68445*	28
14	63269	-4	41	68587	-1
15	63504	5	42	68762	4
16	63721	-1	43	6868922	-4
17	63939	-3	44	69111*	19
18	64152	-8	45	69244*	-13
19	64360*	-16	46	69417	-4
20	64569*	-21	47	69578	-6
21	64766*	-35	48	69727*	-18
22	64950*	-60	49	69917*	12
24	65426	4	50	70073	10
25	65628	3	53	70537	5
26	65861*	36	54	70686	0
27	66026	2	55	70830	-8
28	66205*	-15			
29	66412	-2			
30	66618*	12			
31	66806	10			
32	66977	-6			

Table 4–4: Observed and observed - calculated transition energies of the $F0_u^+(^3P_0)$ ion-pair state of $^{35}Cl^{37}Cl$.

(†) from Reference (2).

Asterisks are values omitted from the fit.

69990 and 70039 cm^{-1}, 71519 and 71569 cm^{-1}, and 71942 and 71984 cm^{-1}, respectively, for the $^{35}Cl_2$ isotopomer, see Table (4.6). Unperturbed $F0_u^+(^3P_0)$ ion-pair levels are predicted for v′ = 49, 59, and 62 at 70009, 71549, and 71947 cm^{-1}. Perturbed $F0_u^+(^3P_0)$ levels are observed at 69984 and 71570 cm^{-1}, i.e. one of each of the doublets, presumably that with the largest percentage of $F0_u^+$ character, although v′ = 62 is absent. It is concluded that the interacting triplet state is the $F0_u^+(^3P_0)$ ion-pair state. Ishiwata et al.[8], observed similar perturbations, the homogenous interaction between the $0_u^+(^3P_2)$ and $0_u^+(^3P_0)$ ion-pair states, and also strong heterogenous coupling between the $0_u^+(^3P_2)$ and $1_u^+(^3P_2)$ ion-pair states were reported. In a paper published recently, Ishiwata et al.[12], have reassigned the $F0_u^+(^3P_0)$ ion-pair state and concluded that the peaks observed in our work [13], should be shifted to higher energies by $3 \sim 5$ cm^{-1} to give the true band origins.

So far only the $^{70}Cl_2$ isotopomer was involved in the analysis of the results, however, a complete analysis has also been carried out on the $^{35}Cl^{37}Cl$ species. The $D0_u^+(^3P_2)$ and $F0_u^+(^3P_0)$ states band positions are included in Tables (4.2) and (4.4), respectively. The spectrum recorded on the $^{37}Cl^+$ channel is shown in Figure (4.5). Analysis of the $^{37}Cl^+$ data agrees with the conclusions derived from the $^{35}Cl_2$ data. The $^{37}Cl_2$ species was not involved in the analysis, because of the weakness of the bands. Some of the stronger transitions are shown in Figure (4.5).

Ishiwata et al.[2], reported v′ = 1-6 and 0-7, of the observed α and γ states. The $D0_u^+(^3P_2)$ and $F0_u^+(^3P_0)$ states, have been correlated with the α and γ states, respectively. Wörmer et al.[6], have proposed that the β state is due to the $1_u(^3P_2)$ state and that it undergoes a heterogenous interaction with the $D0_u^+(^3P_2)$ state through which it gains 0_u^+ character and hence the increased transition intensity from the B state. The effects of the homogenous $F'0_u^+(^1D_2)$ - $F0_u^+(^3P_0)$ interaction observed in the present work tend to support this analysis. Consequently, a reassignment of the lowest vibrational levels of the $D0_u^+(^3P_2)$ state has been carried out. Therefore v′ = 1-5 of the previously assigned α state become v′ = 1-5 of

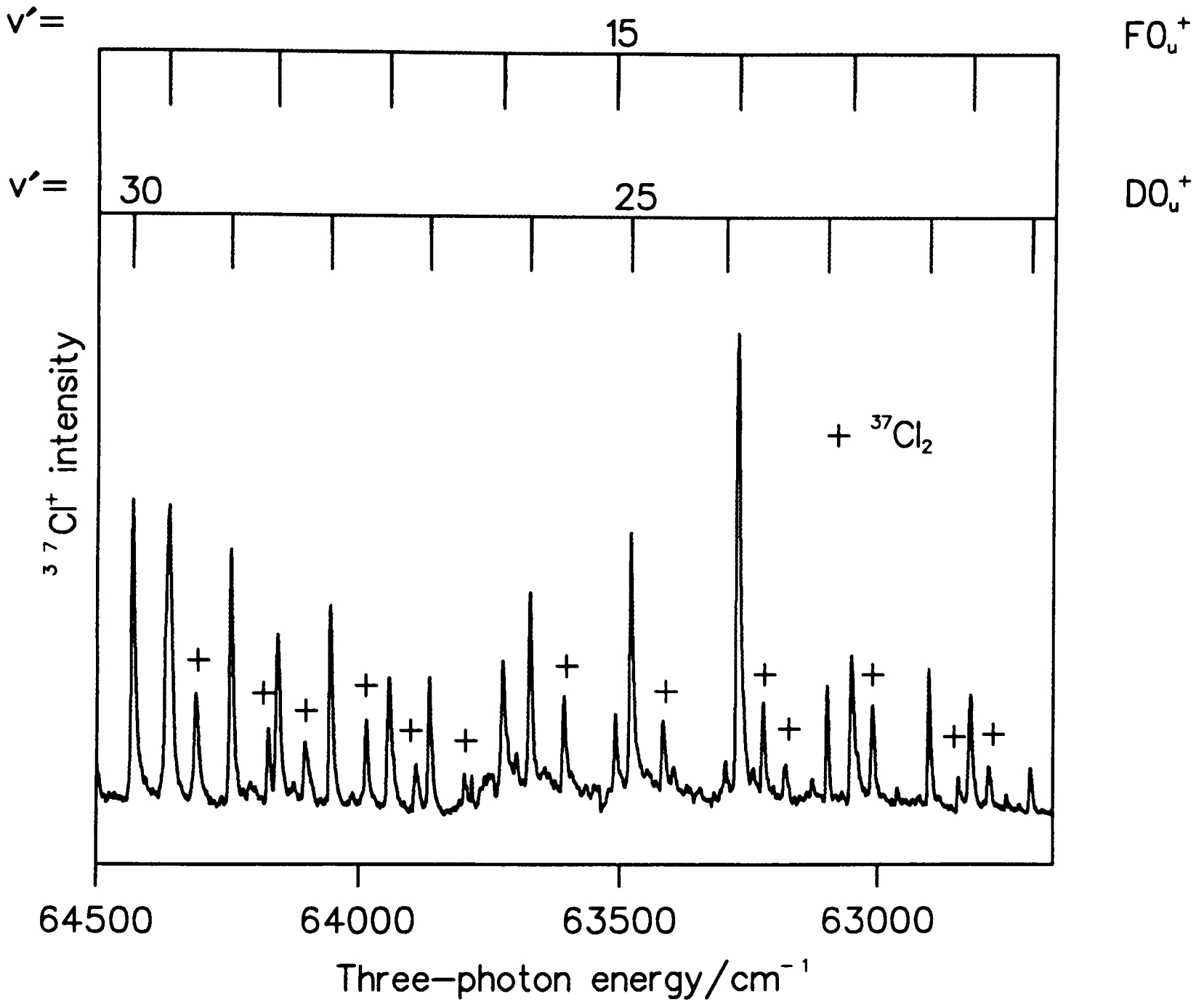

Figure 4–5: One-colour (1+2) excitation spectrum of $^{35}Cl^{37}Cl$ between 62800 - 64500 cm^{-1}, the $^{37}Cl_2$ isotopmer is indicated by the crosses.

the $D0_u^+(^3P_2)$ state and v′ = 6-8 of β state become v′ = 6-8 of the $D0_u^+(^3P_2)$ state. Similarly, the remaining four levels become v′ = 3-6 of the $1_u(^3P_2)$ state. This re-assignment agrees with the subsequent reassignments made by Ishiwata et al.[8], who used (1+2) double resonance *via* bound levels of the $B0_u^+$ state. From the rotationally resolved data they were able to determine that the $1_u(^3P_2)$ state is heterogenously coupled with both the $2_u(^1D_2)$ and $D0_u^+(^3P_2)$ states.

The vibrational fitting procedure described earlier is used to obtain the set of coefficients which can best reproduce an extensive series of observed vibrational levels which are subject to local interstate interactions. Although the standard deviation is quite large, the underlying potential energy curve can be constructed from these 'de-perturbed' vibrational levels. As a result, it was not considered necessary to use the refined vibrational levels given in ref [8] as these were not significantly different from those given earlier [2]. The data given previously for the low vibrational levels of the $D0_u^+(^3P_2)$ state were combined with those observed for the higher vibrational levels of both $^{35}Cl_2$ and $^{35}Cl\ ^{37}Cl$ in the present work. The term values G^i were fitted to a Dunham expansion of the form.

$$G^i(v') = \sum_n Y_{n,0}[\rho_i(v' + 1/2)]^n \tag{4.1}$$

Where $Y_{n,0}$ is a Dunham parameter, v' is the vibrational quantum number, and ρ_i is the ratio $[\mu(^{35}Cl_2)/\mu_i]^{1/2}$, where μ_i is the reduced mass of a particular isotopomer of Cl_2. The calculated values are compared with those observed in Tables (4.1) and (4.2), the coefficients of the expansion are presented in Table (4.5). Levels with values of 10 cm^{-1} or greater were removed from the Dunham expansion.

The same method was applied to derive constants for the $F0_u^+(^3P_0)$ state incorporating v′ = 0-7 from previous work and these are shown in Table (4.5). The differences between observed and calculated values shown in Tables (4.3) and (4.4),

Dunham coeff	**D 0_u^+/cm^{-1}**	α^a/ cm^{-1}	**F 0_u^+/cm^{-1}**	γ^b/cm^{-1}
$Y_{0,0}$	58489.655	58486.08	59925.26	59930.17
$Y_{1,0}$	235.696	235.72	285.325	285.9419
$Y_{2,0}$	-3.91659	-2.543	-3.13532	-3.20578
$Y_{3,0}$	$3.5793633\text{x}10^{-1}$		$8.89079\text{x}10^{-2}$	$9.14335\text{x}10^{-2}$
$Y_{4,0}$	$-2.015293\text{x}10^{-2}$		$-2.221513\text{x}10^{-3}$	$-2.25786\text{x}10^{-3}$
$Y_{5,0}$	$6.6922251\text{x}10^{-4}$		$2.91482\text{x}10^{-5}$	$2.933251\text{x}10^{-5}$
$Y_{6,0}$	$-1.359104775\text{x}10^{-5}$		$-1.486574\text{x}10^{-7}$	$-1.48717\text{x}10^{-7}$
$Y_{7,0}$	$1.65620113\text{x}10^{-7}$			
$Y_{8,0}$	$-1.11026659\text{x}10^{-9}$			
$Y_{9,0}$	$3.142881\text{x}10^{-12}$			

Table 4–5: Vibrational Dunham coefficients for the $D0_u^+(^3P_2)$ and $F0_u^+(^3P_0)$ ion-pair states of $^{35}Cl_2$.

(a) from Reference (8).

(b) from Reference (12).

are as expected much larger above v′ = 20 (i.e., up to ± 30 cm^{-1}), illustrating the major perturbing effect of the F′$0_u^+(^1D_2)$ state. Observed - calculated values of greater than 10 cm^{-1} were again removed from the fit.

The band positions for the F′$0_u^+(^1D_2)$ state are shown in Table (4.6). The levels above v′ = 21 are taken from one-photon absorption data [4], while the remaining levels are perturbed ones, observed in this work. The vibrational numbering follows that of Wörmer et al.[6].

4.3.4 Generation of Potential Energy Curves

The $X0_g^+$, $B0_u^+$ and $C1_u$ States

The $X0_g^+$ ground state and the bound part of the $B0_u^+$ state were generated from RKR turning points reported by Coxon et al.[14]. The repulsive wall of the $B0_u^+$ state was estimated from the absorption data obtained by Maric et al.[9] (see Figure (4.1), and Table (4.7) for the splined knot points). The purely repulsive 1_u state in this work is calculated using an exponential expression of the form [15]

$$V(R) = V_e + Ce^{-\gamma(R-r_e)} \tag{4.2}$$

The potential parameters are as follows

C/cm^{-1}	γ/nm^{-1}	r_e/nm	$V_e/\ cm^{-1}$
10450	45.0	0.1987	20276.6

derived from a comparison of simulated and experimentally observed continuum resonance Raman spectra [15].

v′	$\bar{\nu}_{obs}/cm^{-1}$ $^{35}Cl_2$	$\bar{\nu}_{obs}/cm^{-1}$ $^{35}Cl^{37}Cl$	v′	$\bar{\nu}_{obs}/cm^{-1}$ $^{35}Cl_2$	$\bar{\nu}_{obs}/cm^{-1}$ $^{35}Cl^{37}Cl$
0			19	69386	
1			20		
2			21	69799a	
3			22	69990a&70039a	
4		65762	23	70248a	
5					
6	66321		24	70474a	
7			25	70676a	
8		66785	26	70898a	
9			27	71120a	
10	67295	67256	28	71332a	
11	67514		29	71519&71569a	
12			30	71750a	
13					
14	68234		31	71942&71984a	
15	68436	68363	32	72163a	
16	68655		33	72370a	
17					
18	69132a	69065			

Table 4–6: Observed transition energies of the $F'0_u^+(^1D_2)$ ion-pair state of $^{35}Cl_2$ and $^{35}Cl^{37}Cl$.

(a) from Reference (4).

R/Å	$\bar{\nu}/cm^{-1}$
1.65	38191.0
1.67	33450.6
1.69	29548.1
1.71	26346.2
1.73	23707.5
1.76	20505.7
1.79	17893.8
1.81	16391.3
1.84	14380.9
1.87	12548.2
1.89	11417.2
1.91	10369.6
1.95	8557.7
1.99	7061.7
2.03	5667.7
2.07	4338.4
2.108	3340.1

Table 4–7: Knot points used to generate the repulsive wall of the $B0_u^+$ state.

The $F'0_u^+(^1D_2)$, $D0_u^+(^3P_2)$ and $F0_u^+(^3P_0)$ Ion-Pair States

The $F'0_u^+(^1D_2)$ ion-pair state potential displays a double minimum, where a barrier divides the section with the Rydberg character from that with ion-pair character. Those constants obtained by Wörmer et al.[6], were fitted into a modified Morse curve program, to generate the double well potential shown in Figure (4.1).

The potential energy curves for the $D0_u^+(^3P_2)$ and $F0_u^+(^3P_0)$ ion-pair states were constructed as follows. The outer branches were assumed to be of the form

$$V(R) = D_e - C_1/R - C_4/R^4 - C_6/R^6 \tag{4.3}$$

over the range 12 > R/Å > 6. In eq 1, C_1 is the Coulomb term, $e^2/4\pi\epsilon_0$ (= 1.16645 x 10^5 cm^{-1}), C_4 is the polarization coefficient $1/2(\alpha_{Cl+} + \alpha_{Cl-})\ e^2/(4\pi\epsilon_0)^2$ (= 1.044 x 10^5 cm^{-1}), and C_6 represents the effect of the dispersion forces (C_6 = 1.0 x 10^6 cm^{-1}). The precision of the coefficients is sufficient to generate a potential accurate to ± 1 cm^{-1} at R = 6 Å. There are small differences in the C_4 and C_6 coefficients for the J = 2 and J = 0 states of Cl^+, and for the former there is also a small C_3 coefficient. These were ignored because our aim was to locate the approximate crossing positions of the inner walls of the two lowest 0_u^+ ion-pair states with the inner wall of the double-minimum, $^1\Sigma_u^+/4p$, (ion-pair/Rydberg) state. Trial spline functions for the inner walls of the two potentials were then defined by 10 knot points positioned to join the splined portion smoothly onto the RKR turning points of the potential minima, which span the range 2.6 < R/Å < 3.3. A similar number of knot points was used to join the outer branch of the RKR potential to the asymptotic form in eq (4.1). See Tables (4.8) and (4.9) for knot points used to generate the $D0_u^+(^3P_2)$ and $F0_u^+(^3P_0)$ states respectively. It immediately became apparent that the Y_{11} value for the $F0_u^+(^3P_0)$ state was anomalous (Y_{11} = 0.0017), no doubt as result of perturbations, and the RKR curve derived from it could not be joined smoothly onto the required asymptotic form (4.1). We therefore took the value of Y_{11} found by Ishiwata et al.[2], for the

R/Å	$\bar{\nu}/cm^{-1}$	R/Å	$\bar{\nu}/cm^{-1}$	R/Å	$\bar{\nu}/cm^{-1}$
2.060	88489.6	2.860	58521.1	6.000	76271.2
2.080	85449.0	2.900	58585.7	6.500	77796.9
2.100	82888.4	2.940	58677.5	7.000	79098.5
2.130	79705.2	2.980	58791.0	8.000	81204.0
2.150	77861.0	3.020	58922.0	9.000	82835.6
2.170	76163.3	3.060	59065.3	10.000	84138.0
2.190	74632.5	3.100	59217.7	11.000	85202.2
2.210	73286.2	3.150	59429.5	12.000	86088.2
2.230	72095.0	3.200	59650.3		
2.260	70504.5	3.250	59872.7		
2.300	68623.2	3.301	60184.6		
2.340	66900.3	3.401	60727.4		
2.380	65307.1	3.501	61389.7		
2.420	63838.7	3.601	62107.7		
2.460	62489.3	3.701	62840.3		
2.500	61312.2	3.801	63567.7		
2.540	60391.5	3.901	64280.0		
2.580	59773.9	4.001	64995.5		
2.620	59305.8	4.201	66507.2		
2.660	58943.5	4.401	68000.5		
2.700	58712.5	4.601	69332.7		
2.740	58571.8	4.801	70566.0		
2.780	58503.4	5.001	71710.0		
2.810	58489.655	5.251	73025.8		
2.820	58490.9	5.501	74200.7		

Table 4–8: Knot points used to generate the $D0_u^+(^3P_2)$ ion-pair state potential curve.

R/Å	$\bar{\nu}/cm^{-1}$	R/Å	$\bar{\nu}/cm^{-1}$
2.215	89925.2	3.251	61035.0
2.235	87038.4	3.301	61329.1
2.255	84630.3	3.361	61733.1
2.277	82437.4	3.421	62140.1
2.297	80770.0	3.479	62555.1
2.317	79329.2	3.539	62991.4
2.357	76802.6	3.645	63775.7
2.397	74386.5	3.791	64873.0
2.457	71209.8	4.001	66451.4
2.497	69407.0	4.251	68267.5
2.557	67040.8	4.501	69982.5
2.601	65471.3	4.751	71562.3
2.651	63827.3	5.001	72949.8
2.701	62431.0	5.501	75367.5
2.751	61270.9	6.000	77263.1
2.801	60533.1	7.000	80090.4
2.851	60118.1	8.000	82196.0
2.901	59955.8	9.000	83827.6
2.937	59925.26	10.000	85130.0
2.951	59928.7	11.000	86194.2
3.001	59998.3	12.000	87080.2
3.051	60135.2		
3.101	60318.2		
3.151	60535.3		
3.201	60777.0		

Table 4–9: Knot points used to generate the $F0_u^+(^3P_0)$ ion-pair state potential curve.

$D0_u^+(^3P_2)$ state for both the α and γ states. By adjusting principally those knot points on the inner walls of the two potentials, complete splined potentials were obtained that were both smooth and correctly reproduced the observed spacing and the absolute position of the unperturbed vibrational levels to within $\pm$ 20 cm^{-1} in the region 58000 - 72000 cm^{-1}, together with those at the bottom of the potential well. This is sufficient to determine the width of the potential in the region where the outer wall is dominated by the Coulomb term and hence to locate the absolute position of the inner wall precisely enough for the crossings identified by perturbations to be assigned to the states concerned.

4.4 Discussion

In the 62000 - 72000 cm^{-1} energy range covered in this work two ungerade ion-pair states were seen directly, and one ion-pair state was seen through interactions with the $F0_u^+(^3P_0)$ ion-pair state. In a three-photon transition, the allowed transitions are, $\Delta\Omega$ = 0, 1, 2, and 3. Since there are no ion-pair states with Ω = 3, this leaves six ungerade ion-pair states correlating with $Cl^+(^3P_J) + Cl^-$ and three with $Cl^+(^1D_2) + Cl^-$, which in principle are accessable from the ground state. In previous work, single-photon transitions to the $F'0_u^+(^1D_2)$ ion-pair state was observed strongly [16][17], whereas the $D0_u^+(^3P_2)$ and the $F0_u^+(^3P_0)$ ion-pair states were only seen through interactions with the $F'0_u^+(^1D_2)$ [17].

Two factors can be concluded from those observations on Cl_2. Firstly, after the weak 'spin-forbidden' B $\leftarrow$ X transition at the first photon level, the singlet/triplet character is largely preserved. This indicates that the valence and ion-pair states can be described as essentially pure singlet or triplet structures over the range of separations probed by our experiments. The second factor is that at larger separations, beyond the region of vertical transitions from the ground state, parallel transitions dominate over perpendicular ones, if the transition becomes forbidden

in the separated atom limit.

The first resonant step $B0_u^+ \leftarrow X$ dominates the three-photon spectroscopy reported here. The configuration of the $B0_u^+$ state is $\sigma_g^2\ \pi_u^4\ \pi_g^3\ \sigma_u^1$ (denoted 2431), and thereafter remaining in the triplet manifold and using only parallel transitions, real or virtual, for the next two photons can only result in the (1342) $^3\Pi\ 0_u^+$ configuration. However, since we access both the first and second 0_u^+ ion-pair states from the B state, the (1342) configuration must remain mixed with the (2332) configuration over the range of R between 2 and 3 Å probed by our experiments.

Extending the analysis to the singlet manifold, the pump step in a three-photon process is $C1_u \leftarrow X$. The only parallel two-photon transition from (2431) $C1_u$ is to (1342) $1_u(^1D_2)$, a higher energy ion-pair state than the low-lying (1441) $F'0_u^+(^1D_2)$ state (judged from the σ_u orbital occupancy), so a vertical transition to this state occurs outside our three-photon energy range. Similarly, a nonvertical transition would probably require two probe photons of higher energy than those used in the current experiments in order to satisfy the red extremum requirement. For instance, in a two-colour experiment, the $G'1_g(^1D_2)$ ion-pair state was accessed in a (1+1) two-photon excitation, using a probe photon of 212 nm, which lies near the red extremum of the $G' \rightarrow C$ system [18]. Were perpendicular transitions to be important at the probe state, the (1441) $F'0_u^+(^1D_2)$ configuration could be reached *via* $1441 \leftarrow 2341 \leftarrow 2431$, but this is not observed. As with the other halogens, this configuration is unique among the ion-pair ones in being accessible in a one-photon transition from the ground state that is both parallel and spin conserving.

Another point to consider is the relative strength of the $D0_u^+(^3P_2)/\ F'0_u^+(^1D_2)$ and $F0_u^+(^3P_0)/F'0_u^+(^1D_2)$ interactions. Both triplet states cross the single states on their inner walls, where the singlet molecular orbital configuration is tending to become the most appropriate description of the states. The $D0_u^+(^3P_2)$, $F0_u^+(^3P_0)$, and $F'0_u^+(^1D_2)$ states have 2332, 1342, and 1441 configurations, respec-

tively. Therefore, the $D0_u^+(^3P_2)$ and $F'0_u^+(^1D_2)$ states can only be interconverted to a two-electron shift, but this can not mix singlet and triplet states. In contrast a simple one-electron shift mediated by the spin-orbit operator can couple the $F0_u^+(^3P_0)$ and $F'0_u^+(^1D_2)$ states, and this most probably accounts for the relative strengths of the interactions. By the same consideration the two triplet states should also interact strongly. However, only a weak interaction is observed at low v′ because the states do not cross each other, and are only nested closely, resulting in little vibrational overlap.

4.5 Conclusion

In this chapter, the repulsive part of the $B0_u^+$ intermedaite state, is used to access the 0_u^+ components of three ungerade ion-pair states in Cl_2. In a (1+2) three photon excitation the $D0_u^+(^3P_2)$ and $F0_u^+(^3P_0)$ ion-pair states from the first two tiers are easily accessed via the $B0_u^+$ intermediate state. Transition to the third tier the $F'0_u^+(^1D_2)$ ion-pair state is only observed due to borrowing of intensity, following vibronic coupling with the $F0_u^+(^3P_0)$ ion-pair state. We have not been able to observed the lowest triplet 1_u ion-pair states in a (1+2) excitation via the $C1_u$ valence state, although the intermediate state is efficiently pumped.

4.6 References

(1) T. Ishiwata, J. Si, and K. Obi, J. Chem. Phys., 96 (1992) 5678, and references cited therein.

(2) T. Ishiwata, I. Fujiwara, T. Shinzawa, and I. Tanaka, J. Chem. Phys., 79 (1983) 4779.

(3) S. Peyerimhoff, and R. Buenker, J. Chem. Phys., 57 (1981) 279.

(4) A.E. Douglas, Can. J. Phys., 59 (1981) 835.

(5) T. Moeller, B. Jordan, P. Gürtler, G. Zimmerer, D. Haaks, J. Le Calve and M.-C. Castex, Chem. Phys., 76 (1983) 295.

(6) J. Wörmer, T. Möller, J. Stapelfeldt, G. Zimmerer, D. Haaks, S. Kampf, J. Le Calve and M.-C. Castex, Z.Phys. D., At., Mol. Clusters, 7 (1988) 383.

(7) K. Yamanouchi, T. Tsuchizawa, J. Miyawaki, S. Tsuchiya, Chem. Phys. Lett, 156 (1989) 301.

(8) T. Ishiwata, T. Shinzawa, J. Si, K. Obi, and I. Tanaka, J. Mol. Spect, 166 (1994) 321.

(9) D. Maric, J.P. Burrows, R. Miller, G.K. Moortgat, J. Photochem. Photobiol. A: Chem., 70 (1993) 205.

(10) T. Ishiwata, A. Ishiguro, and K. Obi, J. Mol. Spectr., 147 (1991) 300.

(11) T. Shinzawa, A. Tokunaga, T. Ishiwata, and I. Tanaka, J. Chem .Phys., 83 (1985) 5407.

(12) T. Ishiwata, T. Kusayanagi, and I. Tanaka, J. Mol. Spect., 173 (1995) 552.

(13) M.S.N. Al-Kahali, R.J. Donovan, K.P. Lawley, T. Ridley, and A.J. Yarwood, J. Phys. Chem., 99 (1995) 3978.

(14) J.A. Coxon, J. Mol. Spect., 82 (1980) 264.

(15) J. Strempel and W. Kiefer, J. Chem. Phys., 95 (1991) 2391.

(16) L.C. Lee, M. Suto, K.Y. Tang, J. Chem. Phys., 84 (1986) 5277.

(17) T. Tsuchizawa, K. Yamanouchi, and S. Tsuchiya, J. Chem. Phys., 93 (1990) 111.

(18) M.S.N. Al-Kahali, R.J. Donovan, K.P. Lawley, Z. Min and T. Ridley, Accepted in Chem. Phys. Letts., 1995.

Chapter 5

Sequential (1+1) Excitation, *Via* Repulsive Intermediate States, of the $\beta 1_g$ Ion-pair State and the $[^2\Pi_{1/2}]_c$ 4s; 1_g Rydberg State of Cl_2 in One- and Two-colour Experiments

5.1 Introduction

The *gerade* ion-pair states of Cl_2 correlating to the $Cl^+(^3P_{2,1,0})+Cl^-(^1S_0)$ ionic asymptotes, were studied extensively by Ishiwata et al.[1-6]. Using the OODR technique, a bound intermediate state was used to access the ion-pair states. The $\beta 1_g$ ion-pair state was accessed in the excitation sequence $\beta 1_g \leftarrow A1_u \leftarrow X0_g^+$. Vibrational levels from $v' = 0$ to $v' = 20$, were observed [3].

In a one-colour (2+1) REMPI excitation study Li et al.[8], have accessed vibrational levels $v' = 0$-15 of the $[^2\Pi_{1/2}]_c$ 4s; 1g Rydberg state of Cl_2. This long progression is unexpected since, in a vertical transition, Franck-Condon factors limit the number of vibrational levels to be accessed; usually up to $v' = 4$ of an unperturbed Rydberg state can be seen. They concluded that the reason for the observation of this long progression was due to the excitation going *via* the $C1_u$ repulsive state. They also observed up to thirty vibrational levels of the $\beta 1_g$ ion-pair state.

In the last two chapters the use of the repulsive wall of the intermediate state to access ion-pair states was demonstrated. In this chapter the use of a two-colour experiment to access the $\beta 1_g$ ion-pair state is cited. The main emphasis however, is again on the use of one-colour experiments to access the $[^2\Pi_{1/2}]_c$ 4s; 1g Rydberg state, and $\beta 1_g$ ion-pair state, *via* the $C1_u$ repulsive state. Figure (5.1) describes the excitation schemes for both one- and two-colour experiments.

5.2 Experimental

In the two-colour experiment, two laser beams were generated by a Lambda Physik EMG 201 MSC excimer laser pumping two Lambda Physik dye lasers, an FL3002E (pump) and an FL2002E (probe) as shown in Figure (5.2). The spectra were recorded by scanning the pump laser, with a fixed probe laser wavelength. Probe

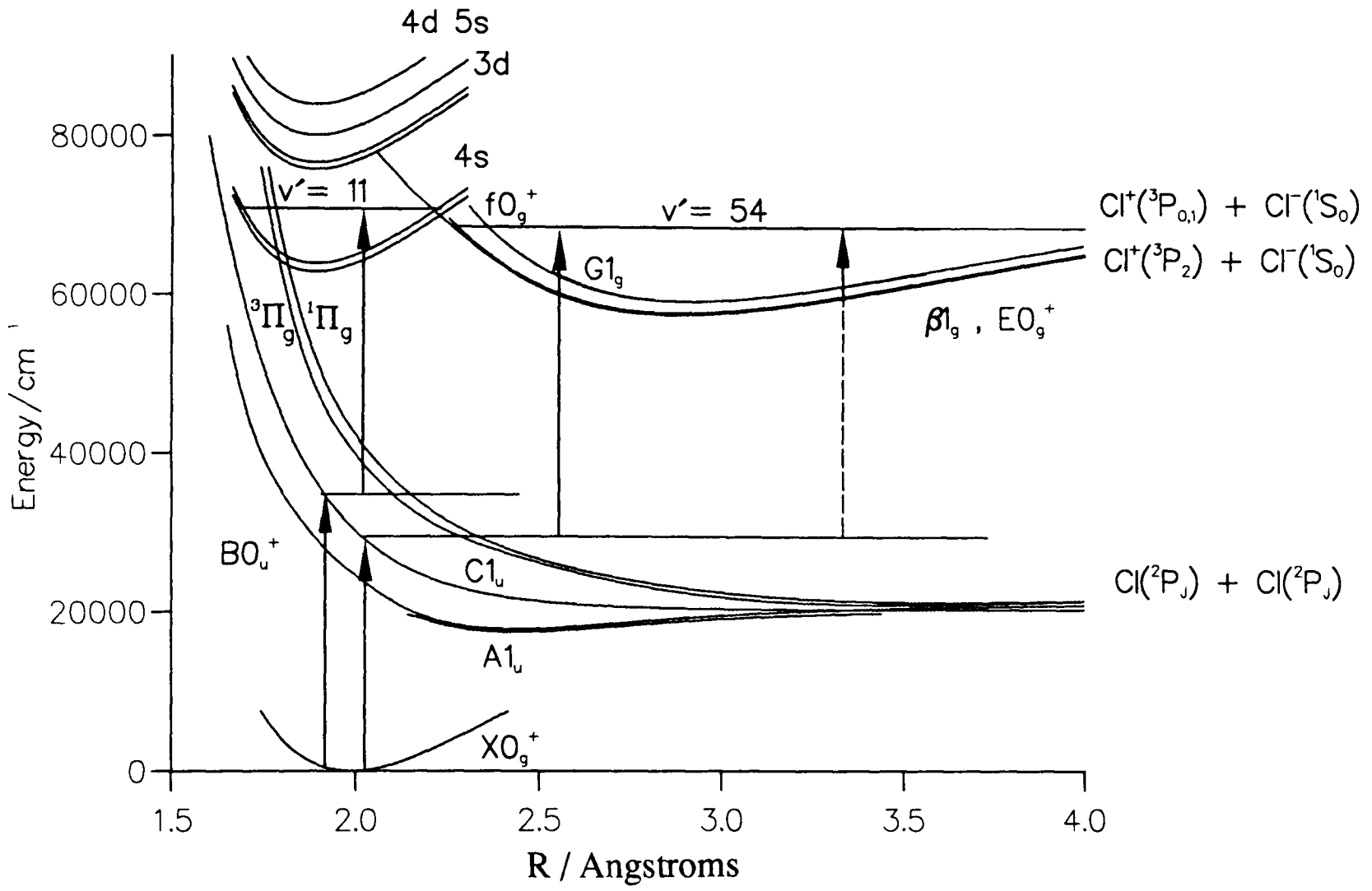

Figure 5–1: Excitation schemes for both one- and two-colour experiments, and the relevant potential enegy curves of Cl_2 discussed in this chapter.

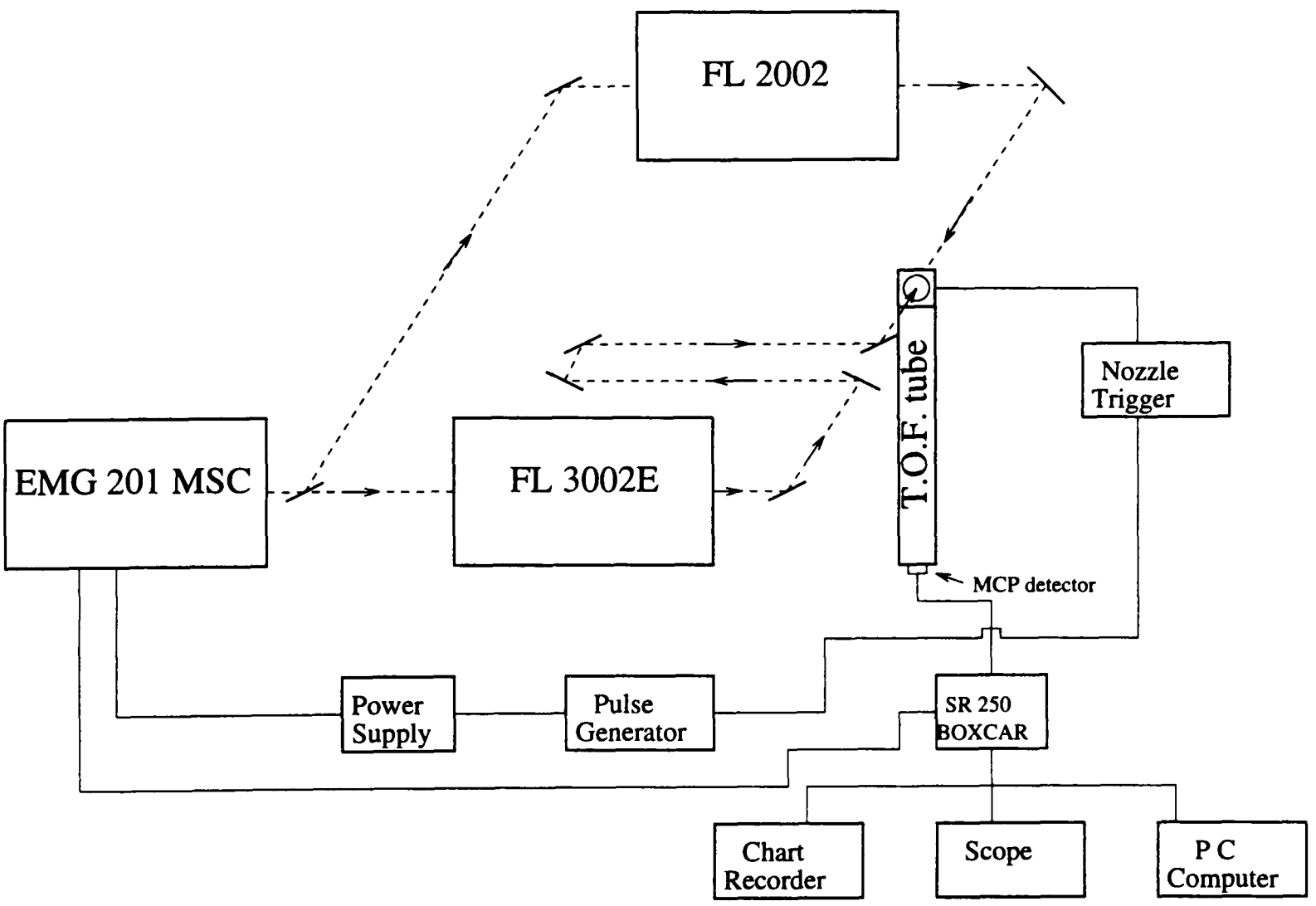

Figure 5–2: Schematic diagram of the experimental apparatus used in the two-colour experiments discussed in this chapter.

photons, between 225 nm and 250 nm, were produced by frequency doubling the output of the dyes Coumarin 2, Coumarin 47 and Coumarin 102 ($\sim$ 1mJ/pulse). The fundamentals of the dyes Coumarin 120, Stilbene 3, Furan 2, PBBO, QUI, DMQ and PTP were used in the pump laser ($\sim$ 10-15mJ/pulse). In order to produce photons which are polarised parallel ($\parallel$) or perpendicular ($\perp$) to each other, the pump beam was passed through a linear polariser (Lambda Physik FL 50) and then through a double Fresnel rhomb. The two laser beams were focused by 5 cm focal length lenses into the molecular beam. In order to minimise one-colour ion signals, the lenses were defocused slightly. The molecular beam was produced by pulsing a mixture of 5 % Cl_2 in He through a nozzle (General Valve) with a 250 μm diameter aperture, into the ionisation chamber of a linear time-of-flight mass spectrometer. The molecular beam was crossed at 90^0 by the two counterpropagating laser beams. The ions therefore were collected at 90^0 to both the molecular beam and the two laser beams. For two-colour experiments, the calibration was achieved in two stages. Firstly, the probe wavelength, before frequency doubling, was chosen to excite an optogalvanic line of neon. Secondly, the scanned pump wavelength was then also calibrated by neon optagalvanic lines.

In one-colour experiments, the frequency doubled outputs of the dyes Rhodamine B, Coumarin 153 and Coumarin 307, were used for excitation. The laser beam was fully focused. Above 500 nm the dye laser fundamental wavelengths were calibrated with an I_2 B $\leftarrow$ X fluorescence excitation spectrum.

5.3 Results

5.3.1 The $\beta 1_g$ Ion-pair State

The one-colour (2+1) REMPI spectrum in Figure (5.3) was recorded on the $^{35}Cl^+$ mass channel, covering an energy region between 71000 cm^{-1} and 78000 cm^{-1} which corresponds to one-photon wavelengths of 281.7 and 256.4 nm. The observed vibrational spacings indicate that the observed spectrum can be assigned to an

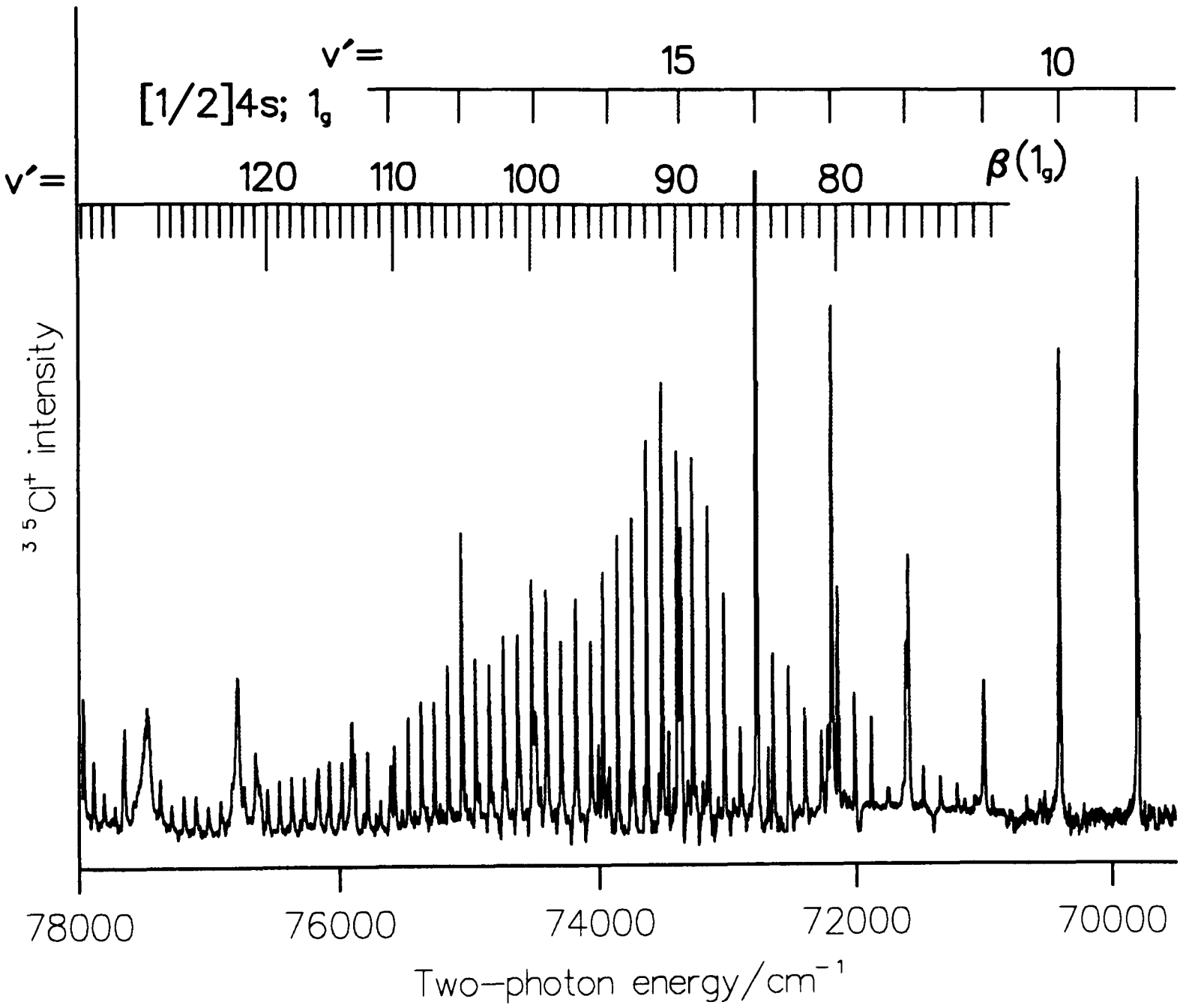

Figure 5–3: The One-colour (2+1) REMPI excitation spectrum of $^{35}Cl_2$ between 69500 cm^{-1} and 78000 cm^{-1}. Showing the $\beta 1_g$ ion-pair state progression and the $[^2\Pi_{1/2}]_c$ 4s; 1_g Rydberg state.

ion-pair state from the first cluster. This ion-pair progression was seen before in a similar experiment and assigned to the $\beta 1_g$ ion-pair state [8].

In the two-colour experiments, the energy region covered is between 61000 cm^{-1} and 69400 cm^{-1}. The probe wavelength was fixed at 250 nm, and the pump wavelength was scanned from 340 nm to 480 nm. The resultant two-colour spectra contain vibrational bands of the $E0_g^+$, $\beta 1_g$, $f0_g^+$ and $G1_g$ ion-pair states. The $\beta 1_g$ state progression at higher energies is shown in Figure (5.4) together with the other ion-pair states. The two-colour experiments confirm that the ion-pair progression obtained in the one-colour experiment, belongs to the $\beta 1_g$ ion-pair state.

The observed vibrational levels obtained using two-colour experiments overlap both previous vibrational data obtained by Ishiwata et al.[3], and the data obtained in one-colour experiments. Therefore, they were assigned accordingly as v'= 21 - 64 of the $\beta 1_g$ ion-pair state, see Table (5.1). Hence, not only the symmetry but also the numbering of the vibrational levels are established. The vibrational levels observed by Li et al.[8] can now be assigned as v'= 65 - 94 of the $\beta 1_g$ state. Using one-colour experiments the analysis was extended up to v'= 166. Above v' = 120, the vibrational levels are perturbed, whereas below v' = 120, the levels are essentially unperturbed within the limits of the accuracy of the measurment ($\pm$ 2 cm^{-1}). The term values of the vibrational levels below v' = 120 were fitted into a Dunham expansion as described in chapter four. Vibrational levels with large errors and levels above v' = 120 were excluded from the fit, see Tables (5.1)(5.2). The Dunham constants obtained are listed in Table (5.3).

5.3.2 The $[^2\Pi_{1/2}]_c$ 4s; 1g Rydberg State

The extended vibrational progression in the $[^2\Pi_{1/2}]_c$ 4s; 1_g Rydberg state is shown in Figure (5.3). Previously, vibrational levels up to v' = 15 were reported by

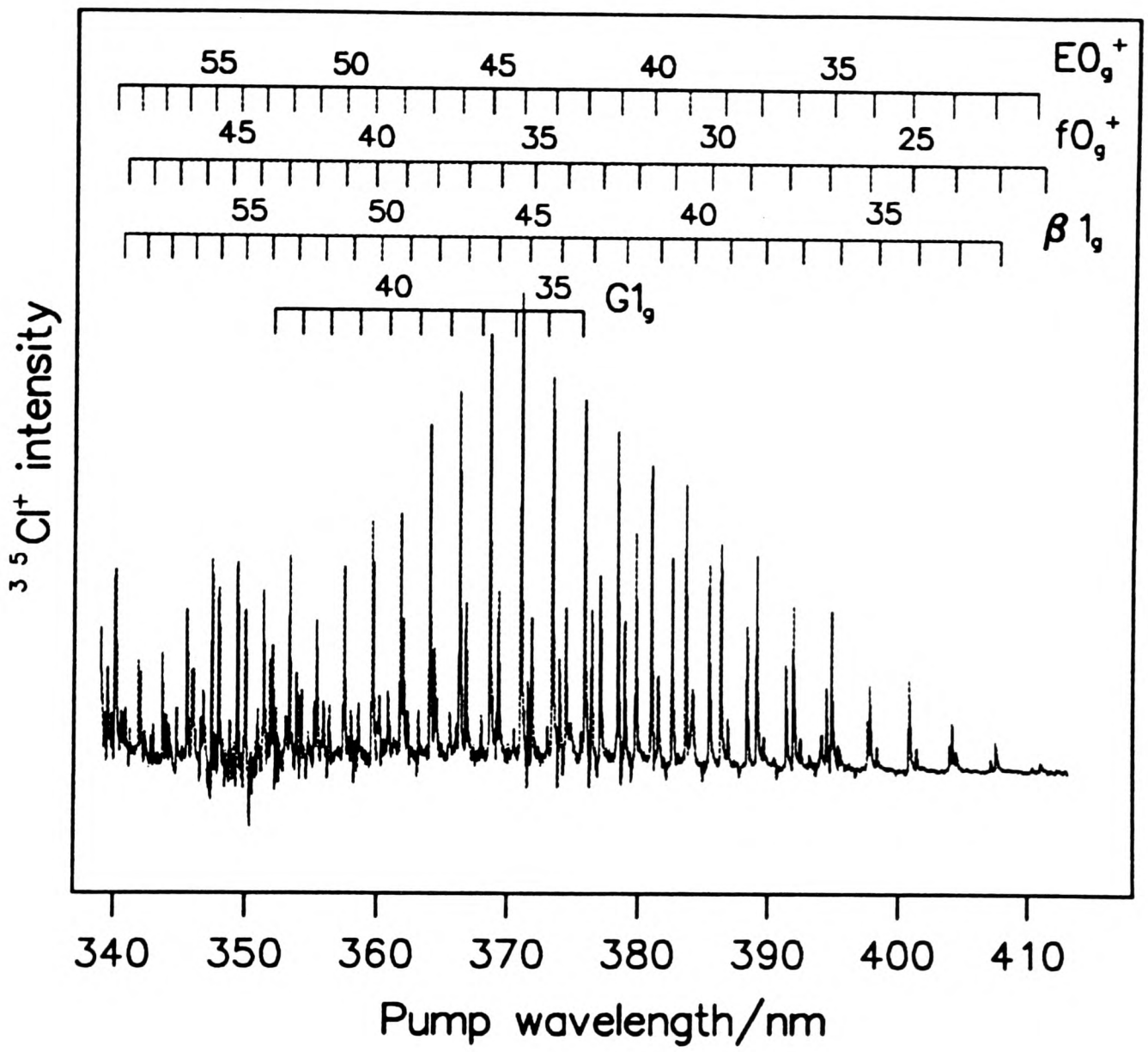

Figure 5–4: A two-colour (1+1) excitation spectrum of the $E0_g^+$, $\beta 1_g$, $f0_g^+$ and $G1_g$ ion-pair states in Cl_2, *via* the purely repulsive C 1_u valence state. The probe wavelength was fixed at 250 nm.

v′	$\bar{\nu}_{obs}/\mathrm{cm}^{-1}$	$\bar{\nu}_{o-c}/\mathrm{cm}^{-1}$	v′	$\bar{\nu}_{obs}/\mathrm{cm}^{-1}$	$\bar{\nu}_{o-c}/\ \mathrm{cm}^{-1}$	v′	$\bar{\nu}_{obs}/\mathrm{cm}^{-1}$	$\bar{\nu}_{o-c}/\mathrm{cm}^{-1}$
0	57689.1*	-0.1	33	64965.3 #	-0.2	62	69903.5 #	+0.6
1	57948.3*	-0.1	34	65156.2 #	-0.1	63	70058.5 #	+5.3 x
2	58196.5*	+0.0	35	65345.5 #	-0.1	64	70201.9 #	+0.5
3	58442.7*	+0.0	36	65533.5 #	-0.2	65	70349.3	+0.6
4	58686.9*	+0.0	37	-	-	66	70495.0	+0.2
5	58929.1*	+0.0	38	-	-	67	70640.1	+0.4
6	59169.4*	+0.0	39	-	-	68	70783.4	-0.1
7	59407.7*	+0.0	40	-	-	69	70926.9	+0.9
8	59644.1*	+0.1	41	66449.1 #	+0.3	70	71068.0	+0.7
9	59878.6*	+0.1	42	66627.5 #	+0.1	71	71207.7	+0.3
10	60111.1*	+0.1	43	66804.7 #	+0.2	72	71346.2	-0.2
11	60341.8*	+0.1	44	66979.9 #	-0.3	73	71485.4	+1.2
12	60570.6*	+0.1	45	67154.4 #	+0.0	74	71621.2	+0.3
13	60797.6*	+0.2	46	67327.0 #	+0.0	75	71757.0	+0.5
14	61022.7*	+0.2	47	67498.5 #	+0.2	76	71891.7	+0.8
15	61245.9*	+0.1	48	67668.1 #	+0.1	77	72026.4	+2.2
16	61467.4*	+0.2	49	67836.3 #	-0.3	78	72156.8	+0.4
17	61687.0*	+0.2	50	68003.6 #	-0.1	79	72287.3	-0.2
18	61904.9*	+0.3	51	68168.2 #	-1.1	80	72416.9	-0.6
19	62120.9*	+0.3	52	68333.5 #	-1.1	81	72546.7	+0.2
20	62335.2*	+0.3	53	68496.1 #	-0.4	82	72674.3	+0.0
21	62547.6 #	+0.1	54	68658.2 #	+0.2	83	72801.3	+0.1
22	-	-	55	-	-	84	72928.4	+1.5
23	62967.0 #	-0.3	56	-	-	85	73054.7	+3.1 x
24	63173.7 #	-0.9	57	-	-	86	73175.6	+0.3
25	63379.8 #	-0.4	58	-	-	87	73298.1	+0.1

Table 5–1: Observed vibrational levels of the $\beta 1_g$ ion-pair state ($^{35}Cl_2$ isotope).

$\bar{\nu}_{o-c}$ is the difference between observed and calculated line positions.

(*) from reference (3).

(#) observed in two-colour experiment.

(x) levels omitted from the Dunham fit.

v′	$\bar{\nu}_{obs}/\mathbf{cm}^{-1}$	$\bar{\nu}_{o-c}/\mathbf{cm}^{-1}$	v′	$\bar{\nu}_{obs}/\mathbf{cm}^{-1}$	$\bar{\nu}_{o-c}/\mathbf{cm}^{-1}$	v′	$\bar{\nu}_{obs}/\mathbf{cm}^{-1}$	$\bar{\nu}_{o-c}/\mathbf{cm}^{-1}$
88	73419.6	-0.1	114	76260.3	+3.3 x	140	78561.4	-
89	73538.5	-1.9	115	76356.5	+2.2	141	78635.7	-
90	73659.2	-0.8	116	76453.6	+1.0	142	78711.5	-
91	73779.6	+0.9	117	76545.6	-2.0	143	78794.1	-
92	73896.8	+0.4	118	76644.2	+1.3	144	78873.9	-
93	74013.3	+0.0	119	76738.4	+0.9	145	78945.3	-
94	74128.5	-0.5	120	76831.6	+0.2	146	79017.1	-
95	74244.3	+0.5	121	76924.9	-	147	79079.2	-
96	74352.4	-5.3 x	122	77015.8	-	148	79186.3	-
97	74469.9	-0.8	123	77103.6	-	149	79257.8	-
98	74581.9	-0.9	124	77198.4	-	150	79327.1	-
99	74694.1	+0.2	125	77293.0	-	151	79396.9	-
100	74803.4	-0.7	126	77382.0	-	152	79459.0	-
101	74913.6	+0.1	127	77471.7	-	153	79549.6	-
102	75022.3	+0.4	128	77562.3	-	154	79614.4	-
103	75130.8	+1.3	129	77643.7	-	155	79679.0	-
104	75237.3	+1.1	130	77736.4	-	156	79743.0	-
105	75342.6	+0.6	131	77823.0	-	157	-	-
106	75447.2	+0.2	132	-	-	158	-	-
107	75552.7	+1.6	133	77990.8	-	159	-	-
108	75656.5	+2.1	134	78076.9	-	160	79983.3	-
109	75757.9	+1.4	135	78154.6	-	161	80047.2	-
110	75858.7	+0.2	136	78238.1	-	162	80105.5	-
111	75962.9	+3.5 x	137	78318.5	-	163	80184.2	-
112	76060.5	+1.1	138	78396.7	-	164	80247.2	-
113	76159.9	+1.3	139	78480.4	-	165	80313.4	-
						166	80381.4	-

v′	$\bar{\nu}_{obs}/\mathbf{cm}^{-1}$	$\bar{\nu}_{o-c}/\mathbf{cm}^{-1}$	v′	$\bar{\nu}_{obs}/\mathbf{cm}^{-1}$	$\bar{\nu}_{o-c}$ $/\mathbf{cm}^{-1}$	v′	$\bar{\nu}_{obs}/\mathbf{cm}^{-1}$	$\bar{\nu}_{o-c}/\mathbf{cm}^{-1}$
78	72016.3	+1.0	100	74652.1	-1.1	122	-	-
79	72146.3	+0.6	101	74763.0	+0.7	123	76953.1	-
80	72274.6	-0.5	102	74870.3	-0.2	124	77045.5	-
81	-	-	103	74978.6	+0.8	125	77138.2	-
82	72530.2	-0.6	104	75084.8	+0.4	126	77229.2	-
83	72657.0	-0.1	105	75193.0	+3.1 x	127	77315.0	-
84	72782.0	-0.3	106	75295.0	-0.3	128	77407.9	-
85	72906.7	-0.2	107	75400.1	+1.5	129	77492.6	-
86	73041.3	+11.6 x	108	75502.9	+1.2	130	77580.6	-
87	73150.7	-1.2	109	75603.0	-1.0	131	77664.1	-
88	73272.1	-1.0	110	75703.3	-2.2	132	77743.2	-
89	73392.0	-1.4	111	75798.3	-7.9 x	133	77830.6	-
90	73510.5	-2.1	112	75907.0	+1.0	134	-	-
91	73628.3	-2.6 x	113	76006.6	+1.5	135	78006.1	-
92	73747.7	-0.5	114	76104.9	+1.5	136	78087.0	-
93	73864.5	-0.1	115	76198.6	-2.3			
94	73979.5	-0.5	116	76300.5	-2.8 x			
95	74094.9	+0.4	117	76391.2	-2.5			
96	74206.5	-1.6	118	-	-			
97	74319.6	-1.1	119	76581.4	-2.0			
98	74431.3	-1.1	120	76675.6	-1.6			
99	74543.0	-0.3	121	76768.8	-			

Table 5–2: Observed vibrational levels of the $\beta 1_g$ ion-pair state ($^{35}Cl^{37}Cl$ isotope).

$\bar{\nu}_{o-c}$ is the difference between the observed and calculated line positions.

(x) levels omitted from the Dunham fit.

Dunham coeff	cm^{-1}
$Y_{0,0}$	57571.73(37)
$Y_{1,0}$	252.455(88)
$Y_{2,0}$	-1.0398(66)
$Y_{3,0}/10^{-3}$	3.12(22)
$Y_{4,0}/10^{-5}$	-1.40(32)
$Y_{5,0}/10^{-8}$	8.3(23)
$Y_{6,0}/10^{-10}$	-2.22(64)

Table 5–3: Vibrational Dunham coefficients for the $\beta 1_g$ ion-pair state of $^{35}Cl_2$.

$\bar{\nu}$ (cm^{-1})	$\bar{\nu}_{Obs-Lit}$[a] (cm^{-1})	**lower state term** ($3s^2 3p^5$)	**upper state term** ($3s^2 3p^4(^3P_2)$)
100048	0.0	$^2P^0_{3/2}$	7s,$^4P^0_{3/2}$
99712	+0.7	$^2P^0_{3/2}$	4d,$^4P^0_{1/2}$
99535	+0.6	$^2P^0_{3/2}$	4d,$^2P_{3/2}$
97340	+1.0	$^2P^0_{3/2}$	4d,$^2D_{5/2}$
96946	+0.3	$^2P^0_{3/2}$	4d,$^4F_{3/2}$
96728	+1.0	$^2P^0_{3/2}$	4d,$^4F_{5/2}$
98391	+0.3	$^2P^0_{3/2}$	6s,$^2P_{1/2}$
98101	+0.7	$^2P^0_{3/2}$	6s,$^4P_{1/2}$
98045	+0.1	$^2P^0_{3/2}$	6s,$^2P_{3/2}$
97808	-0.6	$^2P^0_{3/2}$	4d,$^2F_{5/2}$
99409	+0.4	$^2P^0_{1/2}$	5d,$^4D_{1/2}$
99355	+0.3	$^2P^0_{3/2}$	5d,$^4D_{3/2}$

Table 5–4: (3+1) REMPI transition lines of atomic Cl. $\bar{\nu}_{obs-lit}$ is the difference between observed and reported line positions.

(a) Reference (11).

Li et al.[8]. In this work the same progression is extended up to v′ = 19. The lowest vibrational levels of this state are observed in the mass-resolved (2+1) REMPI spectrum, recorded between 63000 - 67000 cm^{-1} on the $^{35}Cl^+$ mass channel, and shown in Figure (5.5). In this spectrum both $^{35}Cl_2$ and $^{35}Cl^{37}Cl$ peaks are shown. With the exception of the (2,0) band at 65300 cm^{-1} which is the most intense band, where the molecular ion forms < 5 % of the total ion signal, only atomic ion signals were observed. The vibrational levels show fairly regular spacings, in contrast to the widely varying intensities of the bands. The whole vibrational numbering was established by isotopic shifts, including the origin at 64026 cm^{-1}, which agrees well with previous assignments [8][9]. Table (5.5) gives the transition values of the $^{35}Cl_2$ isotopomer, compared with previous measurements [8].

Power dependence measurements for the v′ = 1, 2, and 4 bands were recorded. All three bands intensities increase linearly with the laser power, and the spectra in Figures (5.3) and (5.5) were normalised accordingly. This behaviour suggests that at the one-photon level, a real intermediate state is accessed. The 5*s*, 6*s*, 7*s*, and 8*s* Rydberg states, which lie at higher energies (discussed in the following chapter), show a square power dependence, in striking contrast with the 4*s* Rydberg state. A square power dependency would be expected for a coherent two-photon transition *via* virtual intermediate states.

Theoretical calculations predict that the $[^2\Pi_{1/2}]_c$ 4s;1_g Rydberg state is crossed near its minimum by the dissociative $^1\Pi_{1_g}$ valence state [7]. Evidence for this crossing is shown in Figure (5.3), where the (2,0) band has a large intensity compared to the other vibrational bands, an indication of an interaction with another electronic state. This interaction is further supported by considering the bandwidth measurements of the vibronic bands. In the 4s;1_g Rydberg state, they are

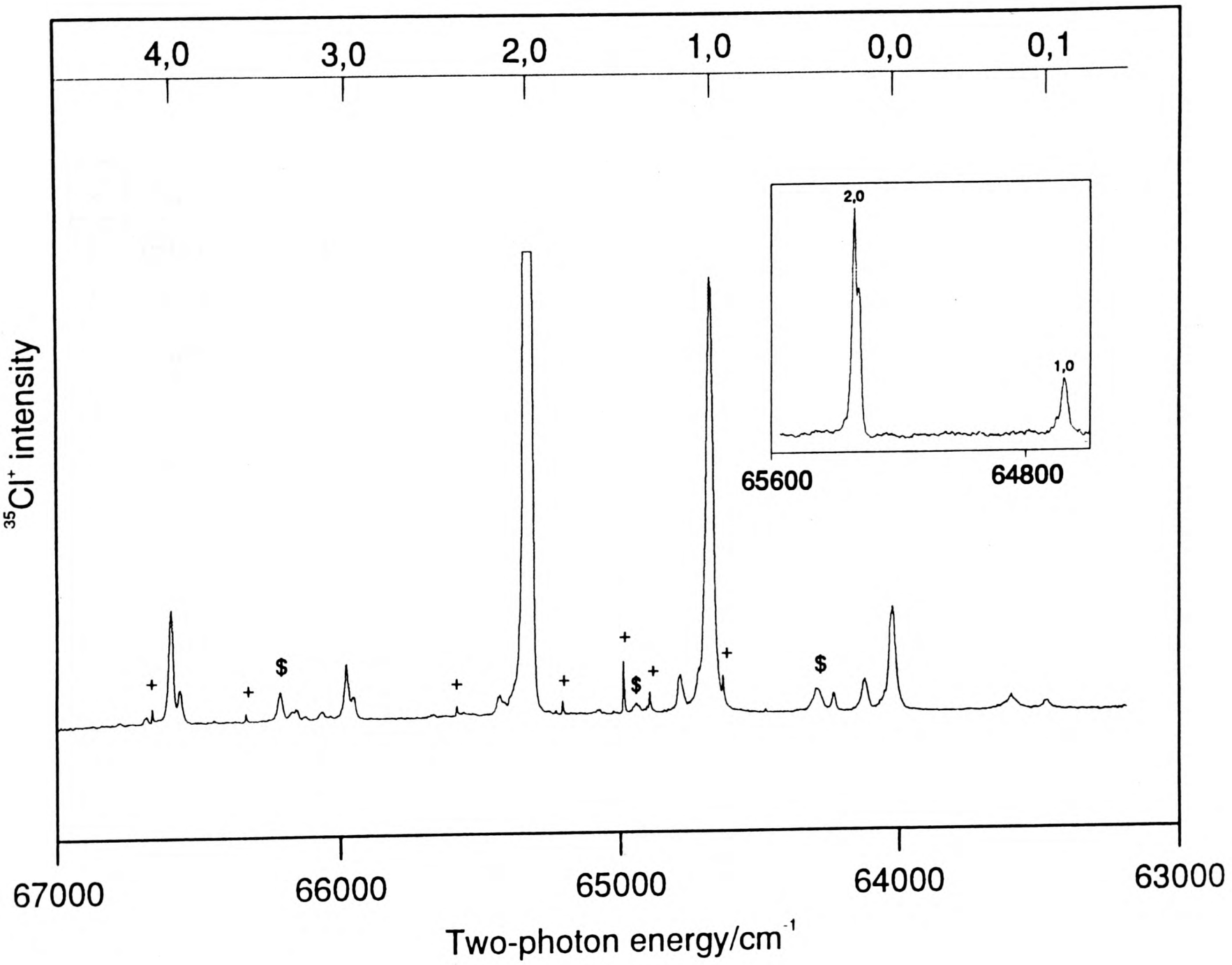

Figure 5–5: The one-colour (2+1) REMPI excitation spectrum of $^{35}Cl_2$ and $^{35}Cl^{37}Cl$ between 63000 cm^{-1} and 67000 cm^{-1}, showing the $[^2\Pi_{1/2}]_c$ 4s; 1_g Rydberg state progression. The \$'s are those of the weak $[^2\Pi_{3/2}]_c$ 4s; 1_g Rydberg state progression. The +'s are atomic lines.

v′	$\bar{\nu}_{obs}/\mathbf{cm}^{-1}$	$\bar{\nu}_{lit}/\mathbf{cm}^{-1}$	v′	$\bar{\nu}_{obs}/\mathbf{cm}^{-1}$	$\bar{\nu}_{lit}/\mathbf{cm}^{-1}$
0	64026	64027	10	70391	70392
1	64678	64681	11	70995	70998
2	65340	65332	12	71593	71600
3	65992	65986	13	72183	72187
4	66637	66640	14	72775	72771
5	-	67270	15	73353	73343
6	-	67905	16	73925	-
7	-	68534	17	74492	-
8	69165	69220	18	75063	-
9	69782	69779	19	75609	-

Table 5–5: Observed vibrational levels of the $[^2\Pi_{1/2}]_c$ 4s;1_g Rydberg state ($^{35}Cl_2$ isotope), compared with literature values from reference (8).

$\sim$ 15 cm^{-1}, while for the $5s$, $6s$, $7s$ and $8s$ Rydberg states, which lie at higher energies, under the same experimental conditions, they are only $\sim$ 3 cm^{-1}. It can be deduced from such observations, that the lifetime of the $[^2\Pi_{1/2}]_c$ 4s; 1_g Rydberg state bands in this energy region are shortened due to predissociation from the interaction with a repulsive state. It is concluded that the $[^2\Pi_{1/2}]_c$ 4s; 1_g Rydberg state is crossed on its inner wall by the $^1\Pi_{1_g}$ repulsive valence state, which intersects it between v′ = 1 and v′ = 2. The large intensities of the v′ = 1 and v′ = 2 bands are due to the increase in the efficiency of the ionisation step. Because of the predissociation of the v′ = 1 and v′ = 2 Rydberg levels, Cl atoms are formed, which then are ionised more efficiently than ionisation of the Rydberg state itself, resulting in an increase in the ion signal.

In this work the weak $^3\Pi_g$ Rydberg state reported by Li et al.[8], was not observed. However, the weak bands to the blue of each of the $[^2\Pi_{1/2}]_c$ 4s;1_g Rydberg state bands are all consistent, to within $\pm$ 2 cm^{-1}, as being hot bands of that progression. we have confirmed this by isotopic shifts (this work).

There are three unidentified bands, which can not be assigned to either the prominent progression from the $[^2\Pi_{1/2}]_c$ 4s;1_g Rydberg state or the hot bands of that progression. Two of the bands at 64290 cm^{-1} and 66233 cm^{-1} were observed previously. They were assigned from isotopic shifts and photoelectron data [8] [9], as the (2,0) and (5,0) bands of a progression based on the $[^2\Pi_{3/2}]_g$ ionic core. In this work, a third weak band assigned as the (3,0) band of this weak progression, is observed at 64942 cm^{-1}. Extrapolation of the three values predicts a (0,0) band at 62970 cm^{-1}. In the following chapter, the $5s$, $6s$, $7s$ and $8s$ Rydberg states, based on the $[^2\Pi_{3/2}]_g$ ionic core are split into two spin-orbit components the 2_g and 1_g. When the spin-orbit and ionic core splittings are considered, this weak progression is predicted to be that of the $[^2\Pi_{3/2}]_c$ 4s; 1_g Rydberg state. It is believed that the (2,0) and (3,0) bands gain their intensities by interacting with the $^3\Pi_{1_g}$ repulsive valence state, as predicted by theoretical calculations [7].

A number of atomic ions were observed and their transitions are listed in Table (5.4), and labelled in Figure (5.5). They all show good agreement with previous assignments [11].

5.4 Generation of Potential Energy Curves

5.4.1 The $\beta 1_g$ Ion-pair State

The potential energy curve for the $\beta 1_g$ state was built up as follows. The outer branch is described by a truncated Rittner potential, as discussed in chapter four, over the range 12 > R/Å > 6. A trial spline function for the inner wall of the potential is then defined by knot points positioned to join the splined portion, smoothly onto the RKR turning points of the potential minimum. Which covers the range 2.45 < R/Å < 3.65 [3]. The same number of knot points is used to join the outer branch of the RKR potential to the asymptotic form of the Rittner potential. The knot points were then adjusted until the potential reproduces the observed spacings and absolute positions of the vibrational levels to within ± 3 cm^{-1}. Table (5.6) gives the knot points of the $\beta 1_g$ state.

5.4.2 The Rydberg States

All of the Rydberg state potential curves in Figure (5.1) were produced using the spectroscopic constants for the ground state of the ion [12]. Koenders et al.[9], obtained a simulation for the band head contours of the (2,0) and (5,0) bands of the $[^2\Pi_{1/2}]_c$ 4s; 1_g Rydberg state. However, the (2,0) band is perturbed, as is shown in this work. For instance, the R_e value obtained, is $\sim$ 1.84 Å which is very small compared to the ground state of the ion $\sim$ 1.89 Å and that of the molecular ground state, $\sim$ 1.99 Å. Because of this perturbation the ground state constants of the ion were used to generate all the Rydberg potentials in this work.

R/Å	$\bar{\nu}/cm^{-1}$	**R/Å**	$\bar{\nu}/cm^{-1}$
2.00	81356.9	3.40	60296.5
2.10	75697.8	3.50	61104.9
2.20	71228.6	3.60	61933.2
2.30	67181.2	3.70	62773.3
2.40	63746.7	3.80	63618.0
2.50	61044.0	3.90	64451.4
2.60	59249.1	4.00	65264.5
2.70	58183.3	4.50	68942.2
2.80	57674.0	5.00	71908.7
2.876	57572.6	5.50	74317.0
2.90	57582.3	6.00	76268.9
3.00	57798.1	6.50	77794.5
3.10	58235.5	7.00	79096.2
3.20	58829.0	7.50	80220.4
3.30	59528.5	8.00	81201.8

Table 5–6: Knot points used to generate the $\beta 1_g$ ion-pair state.

5.4.3 The $X0_g^+$, $B0_u^+$, $C1_u$, $^3\Pi_{1_g}$ and $^1\Pi_{1_g}$ States

The $X0_g^+$ ground state and the bound part of the $B0_u^+$ state were generated from the RKR turning points obtained by Coxon et al.[13]. The repulsive wall of the $B0_u^+$ state is described by splined knot points, listed in chapter four. The purely repulsive $C1_u$ state curve was obtained from Raman experimental data [14].

The repulsive $^3\Pi_{1_g}$ and $^1\Pi_{1_g}$ valence state potentials were generated from splined knot points, listed in Table (5.8) placed so that they cross the $4s$ Rydberg states in positions which are estimated from experimental results obtained in this work. The positions of the $^{1,3}\Pi_{1_g}$ repulsive states and those of the $4s$ Rydberg states, agree reasonably well with the theoretical calculations [7].

5.5 Discussion

5.5.1 Bond Stretching in (2+1) REMPI Spectrum

From Figure (5.3) it can be seen that the intensities of the bands of the $\beta 1_g$ system increase gradually in intensity from 71000 cm^{-1} to 73500 cm^{-1}, and then decrease to 78000 cm^{-1}. If the two-photon transition to the $\beta 1_g$ state was vertical the intensities of the bands should increase steadily with the increase in the Franck-Condon factors as higher v′ levels are accessed. Over this range the $\langle\ X\ |\ \beta\ \rangle$ Franck-Condon factor increases by a factor of $\sim$ 6000. However, the power normalised spectrum in Figure (5.3), shows a very different intensity pattern. Figure (5.3) shows that the lowest two-photon transition from the $X0_u^+$ ground state to the $\beta 1_g$ state is (71,0) at 70929 cm^{-1}, corresponding to a one-photon wavelength of 282 nm. The inner turning point of the $\beta 1_g$ state for this transition is 2.20 Å whereas the outer turning point of the $X0_u^+$ ground state is 2.05 Å. Such an increase in R, in one-photon transitions, is expected to be very weak. Typically, in normal circumstances, the vertical $\beta 1_g \leftarrow X0_u^+$ transition, is estimated to start around 74000 cm^{-1}. As a consequence, the role of the repulsive $C1_u$ state at

$^1\Pi_{1_g}$		$^3\Pi_{1_g}$	
R/Å	$\bar{\nu}/cm^{-1}$	**R/Å**	$\bar{\nu}/cm^{-1}$
1.74	76000.0	1.71	76000.0
1.82	58370.9	1.80	56615.5
1.90	47248.2	1.90	44555.2
2.00	39785.7	2.00	37979.3
2.10	34796.4	2.10	33182.8
2.20	31394.6	2.20	30034.6
2.30	29149.1	2.30	28000.0
2.40	27566.4	2.40	26548.2
2.50	26304.1	2.50	25472.4
2.60	25275.8	2.60	24646.3
2.70	24420.5	2.70	23954.2
2.80	23688.4	2.80	23355.1
2.90	23064.5	2.90	22841.8
3.00	22539.9	3.00	22407.1
3.20	21753.5	3.20	21745.0
3.40	21258.9	3.40	21311.6
3.60	20985.9	3.60	21049.7
3.80	20864.2	3.80	20902.3
4.00	20823.5	4.00	20812.1
4.50	20678.3	4.50	20595.3
5.00	20388.4	5.00	20389.1
6.00	20277.7	6.00	20277.7

Table 5–7: Knot points used to generate the $^3\Pi_{1_g}$ and $^1\Pi_{1_g}$ repulsive valence states.

the one-photon level must be examined.

The envelope of the $\beta 1_g$ state bands in Figure (5.3), can be explained as due to two factors. Firstly, the long wavelength limit (λ_{max}) of the envelope, is determined by the red extremum of the $\beta 1_g \rightarrow C1_u$ emission system. A simulation of this system (from v' = 70) is shown in Figure (5.6). From this simulation it can be seen that the limit of λ_{max} lies around 280 nm. Secondly, the short wavelength limit (λ_{min}) is due to the end of the $C1_u \leftarrow X0_u^+$ absorption, which occurs around 260 nm [10]. Therefore the range 280 - 260 nm covered gives a two-photon energy range of 71429 - 76923 cm^{-1} which matches the range covered by the envelope of the $\beta 1_g$ state vibrational bands seen in Figure (5.3). The same bond stretching phenomenon was observed in the one-colour E $\leftarrow$ B $\leftarrow$ X two-photon excitation of I_2, as discussed in chapter three.

Similar considerations can be applied to the extended $[^2\Pi_{1/2}]_c$ 4s; 1_g Rydberg progression. A Mulliken difference potential between the 4*s* Rydberg and $C1_u$ states, is obtained but shows no maximum because of the forms of the two states (see Figure (5.7)). Simulations of this emission system from various levels of the $[^2\Pi_{1/2}]_c$ 4*s* Rydberg state, showed that photons, between 313 - 255 nm, can excite the reverse transition. The C $\leftarrow$ X absorption limit of 260 nm still applies here. The range of vibrational levels observed for the $[^2\Pi_{1/2}]_c$ 4s; 1_g Rydberg state (ie v' = 0 - 19) agrees well with this prediction. The reason why the vibrational bands of this Rydberg state have strong intensities, compared with the other 4*s* sub-states, is due to two factors. Firstly, because it is a singlet state, like the $X0_g^+$ and the $C1_u$ states, the transition is spin allowed. Secondly, the second step, is a parallel, $1_u \rightarrow 1_g$ ($\sigma_u \rightarrow$ ns) transition, which is favoured.

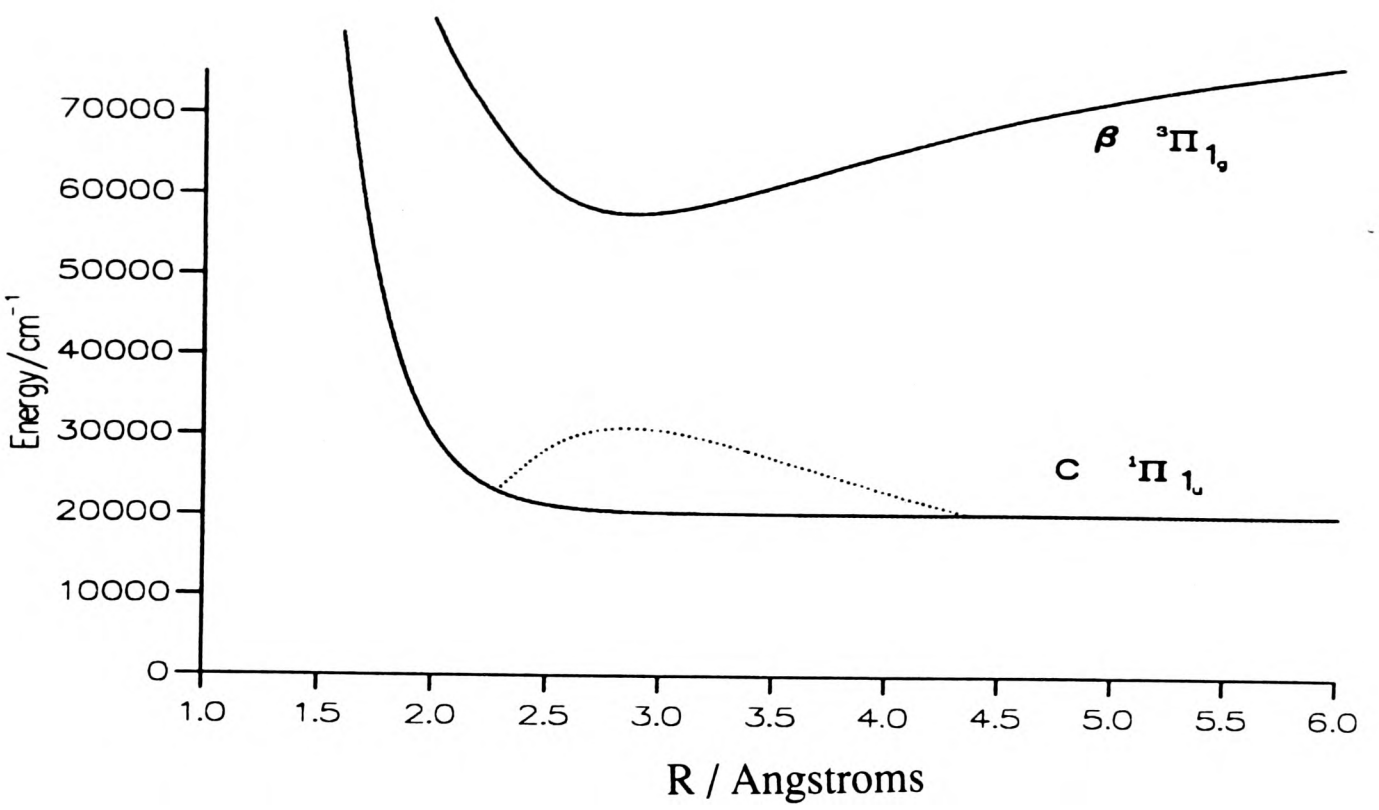

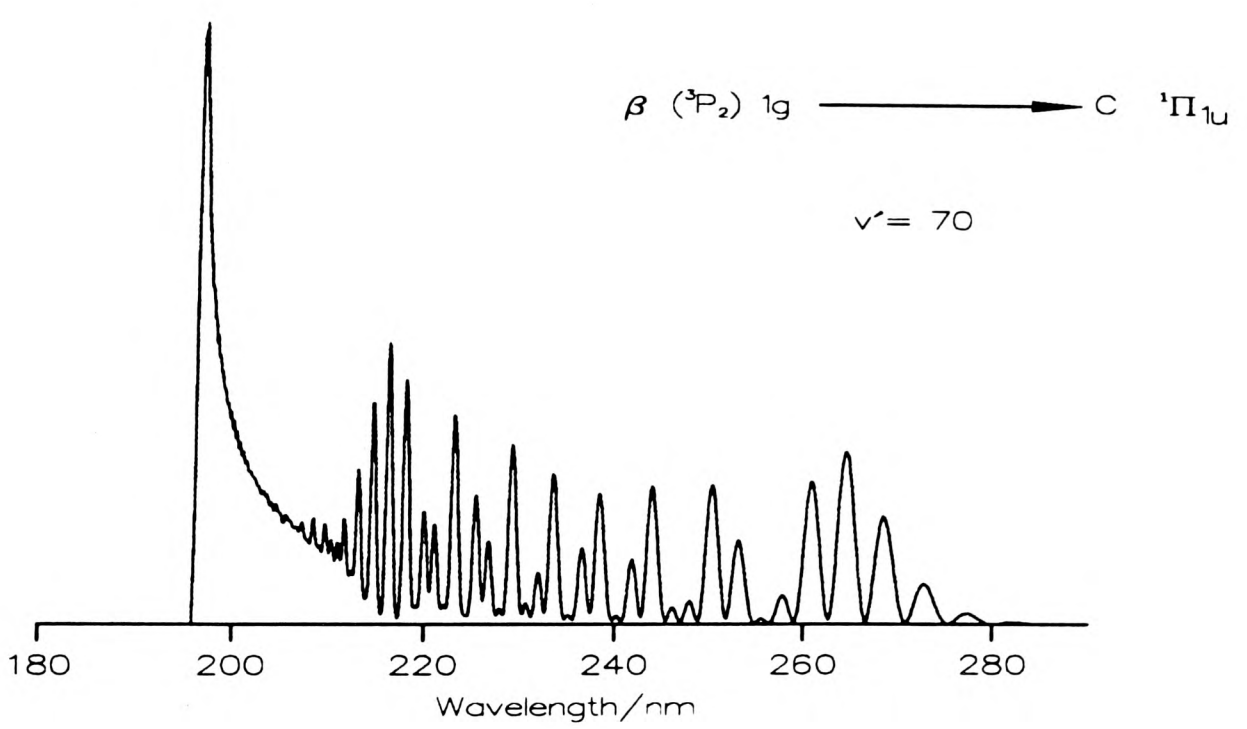

Figure 5–6: Mulliken difference potential produced between the $\beta 1_g$ state and the $C1_u$ repulsive state, and the $\beta \rightarrow$ C emission simulation, from v′ = 70 of the β state.

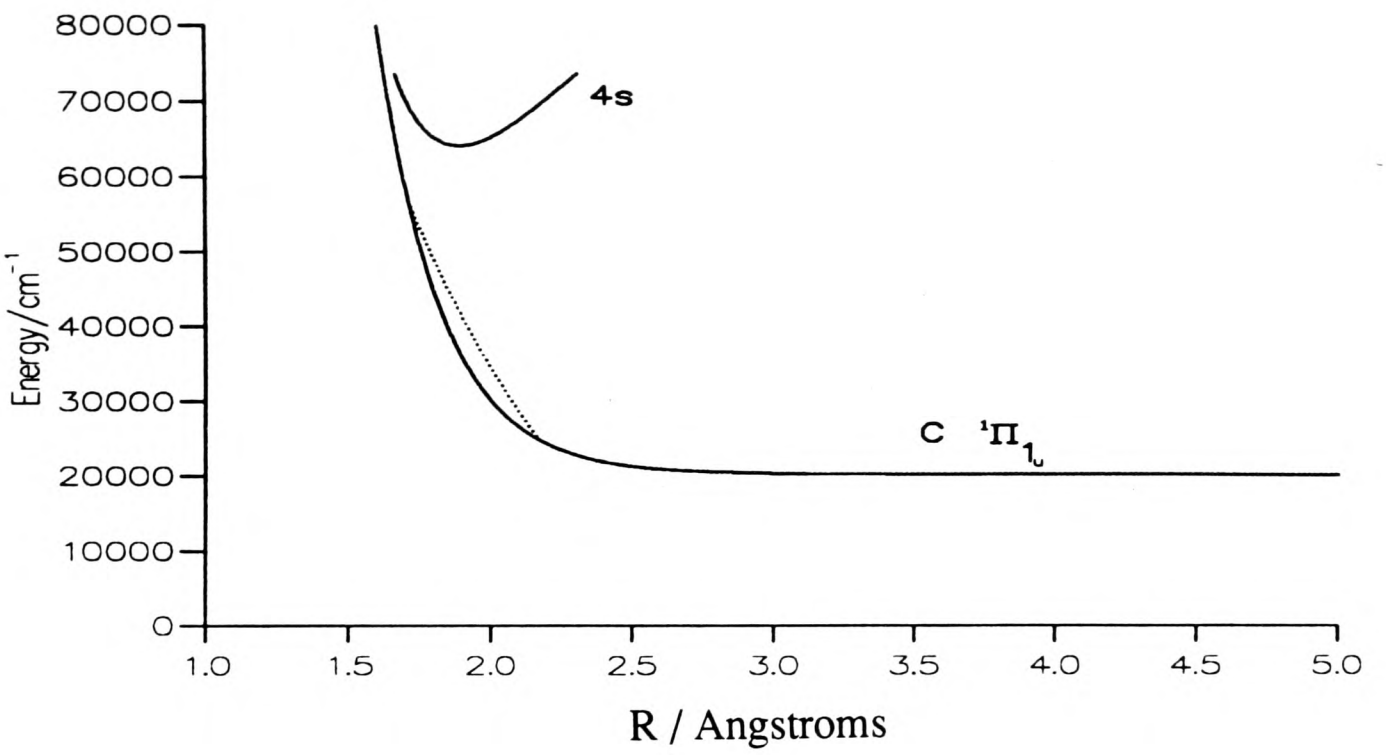

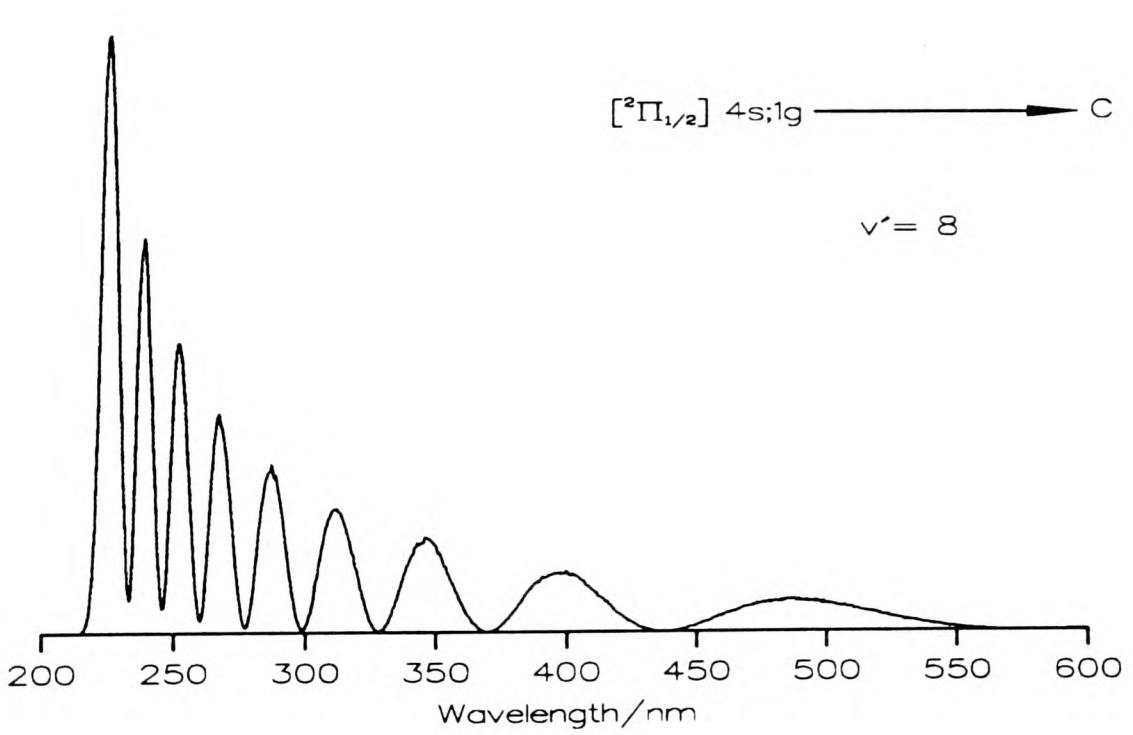

Figure 5–7: Mulliken difference potential between the $4s$ Rydberg state and the Cl_u repulsive state, and the $4s \rightarrow$ C emission simulation, from $v' = 8$ of the 4s Rydberg state.

5.6 Conclusion

In chapter three it was shown that the use of one-colour experiments to access the vibrational levels of an ion-pair state, *via* a repulsive intermediate state, is limited to a narrow spectral region. To access lower and higher vibrational levels, the laser wavelengths must be scanned independently. In this chapter the feasibility of two-colour experiments has been demonstrated. The low vibrational levels of the $\beta 1_g$ ion-pair were accessed via the purely repulsive $C1_u$ state. The probe laser wavelength was fixed to lie near the red extremum region of the $\beta 1_g \rightarrow C1_u$ emission system, and the pump laser wavelength was scanned: the combined energy of the pump and probe beams thus gave access to the lower vibrational levels of the $\beta 1_g$ state.

Extended vibrational progressions for both the $\beta 1_g$ ion-pair state and the $[^2\Pi_{1/2}]_c$ 4s; 1_g Rydberg state were also observed, using one-colour excitation. The vibrational envelopes have been explained in terms of the restrictions imposed by the $C1_u \leftarrow X0_g^+$ absorption limit, and the red extremum of the $\beta 1_g \rightarrow C1_u$ emission system.

5.7 References

(1) T. Ishiwata, T. Shinzawa, T. Kusayanagi and I. Tanaka, J. Chem. Phys. 82 (1985) 1788.

(2) T. Shinzawa, A. Tokunaga, T. Ishiwata and I. Tanaka, J. Chem. Phys. 83 (1985) 5407.

(3) T. Ishiwata, A. Ishiguro and K. Obi, J. Mol. Spectrosc. 147 (1991) 321.

(4) J-H. Si, T. Ishiwata and K.Obi, J. Mol. Spectrosc. 147 (1991) 334.

(5) T. Ishiwata, Y. Kasaki and K. Obi, J. Chem. Phys. 95 (1991) 60.

(6) T. Ishiwata, J-H. Si and K. Obi, J. Chem. Phys. 96 (1992) 5678.

(7) S. D. Pererimhoff and R. J. Buenker, Chem. Phys. 57 (1981) 279.

(8) L. Li, R.J. Lipert, H. Park, W.A. Chupka and S.D. Colson, J. Chem. Phys. 88 (1988) 4608.

(9) B.G. Koenders, S.M. Koeckhoven, G.J. Kuik, K.E. Drabe and C.A. De Lange, J. Chem. Phys. 91 (1989) 6042.

(10) D. Maric, J. P. Burrows, R. Miller and G. K. Moortgat, J. Photochem. Photobiol. A : Chem. 70 (1993) 205.

(11) A.M. Cantu, W. H. Parkinson, T. Grisendi and G. Tagliaferri, Physica, Scripta 31 (1985) 579.

(12) H. van Lonkhuyzen and C.A. de Lange, Chem.Phys., 89 (1984) 313.

(13) J.A. Coxon, J. Mol. Spectrosc. 82 (1980) 264.

(14) J. Strempel and W. Kiefer, J. Chem. Phys. 95 (1991) 2391.

Chapter 6

Mass-Resolved (2+1) Resonance Enhanced Multiphoton Ionisation (REMPI) of The Low-Lying Gerade Rydberg States of Cl_2

6.1 Introduction

An extensive number of investigations on the *ungerade* Rydberg states of Cl_2 have been carried out, mainly because for one-photon absorption from the ground state, *ungerade* states are allowed, whereas *gerade* states are forbidden. In an early study by Douglas et al.[1], the absorption spectrum of Cl_2 was photographed over the range 1330 - 1450 Å. A number of violet shaded bands were observed. Möller et al. [2], have carried out an investigation on the same $4p$ Rydberg states, using fluorescence and absorption experiments. Koenders et al.[3], have excited several $4p$ Rydberg states based on the $[^2\Pi_{3/2}]_g$ and $[^2\Pi_{1/2}]_g$ ionic cores, using a (3+1) REMPI PES.

In threshold electron impact excitation of Cl_2 (2 - 14 eV) Jureta et al.[4] have observed, among the optically allowed states, some optically forbidden states, particularly the *gerade* $4s$ $^{1,3}\Pi_g$ Rydberg states. Later Spence et al.[5], using electron energy loss spectroscopy, identified the band origins of the *gerade* $4s$ Rydberg states seen by Juerta et al, as hot bands. Stubbs et al.[6], using the latter technique have seen a number of Rydberg progressions, with a better resolution $\sim$ 18 meV (FWHM), including the symmetry forbidden $4s$ $^1\Pi_g$ and $5s$ $^1\Pi_g$ Rydberg states.

More recently Koenders et al.[7], and Li et al.[8], have investigated the $4s$ $^1\Pi_g$ Rydberg state. The first using photoelectron spectroscopy with multiphoton excitation (REMPI-PES) to study ionisation and dissociation of Cl_2 *via* the $4s$ $^1\Pi_g$ Rydberg state. The latter, using mass-resolved REMPI techniques, where they have observed v′ = 0 - 15 of the $[^2\Pi_{1/2}]_c$ 4s;1_g Rydberg state, and v′ = 65-94 vibrational levels of the $\beta 1_g$ ion-pair state. In the previous chapter the $[^2\Pi_{1/2}]_c$ 4s;1_g Rydberg state was re-examined and the progression was extended to v′ = 19. Also, the $\beta 1_g$ ion-pair state progression was extended up to v′ = 166.

The complete (2+1) REMPI spectra of Br_2 and I_2 up to the ionisation limit were reported by Donovan et al.[9][10]. In this chapter the progressions of twenty two Rydberg states of Cl_2 will be discussed, most of which were seen for the first time. Mass resolution, power dependence, bandwidth, and linear and circular polarisation measurements were obtained, to assist in the assignments of the spectra. In addition, the extended $\beta 1_g$ ion-pair state progression and its interaction with the $3d$ Rydberg states will be discussed. Interaction with higher Rydberg states will also be discussed.

6.2 Experimental

The experimental setup is described in detail in chapter two. Here the frequency doubled output of the Coumarin dyes 307, 102, 47, and 120 covered the wavelength range 263 - 222.5 nm, corresponding to two-photon energies of 76000 - 90000 cm^{-1}. The spectra were recorded by collecting the $^{35}Cl_2^+$, $^{35}Cl^{37}Cl^+$, $^{35}Cl^+$ and $^{37}Cl^+$ ion signals. All the spectra were normalised to the square of the laser power for a two-photon transition.

6.3 Results

Figures (6.1) and (6.2), show the mass-resolved (2+1) REMPI spectra between 79500 - 89900 cm^{-1}. Both spectra were recorded by collecting the $^{35}Cl_2^+$ ion signal which is the most intense peak in the mass spectrum over this energy region. By comparison it comprises less than 5 % of the total ion signal below 75000 cm^{-1}. All bands above 80000 cm^{-1} show squared power dependence, as anticipated for a coherent two-photon absorption *via* virtual intermediate states. This is confirmed by the one-photon absorption of Cl_2 reported by Maric et al.[11] which shows that at this one-photon wavelength no intermediate state is accessable. Therefore the spectra in Figure (6.1) and (6.2), were normalised to the square of the laser power. In the previous chapter the $[^2\Pi_{1/2}]_c$ $4s;1_g$ Rydberg progression showed a linear

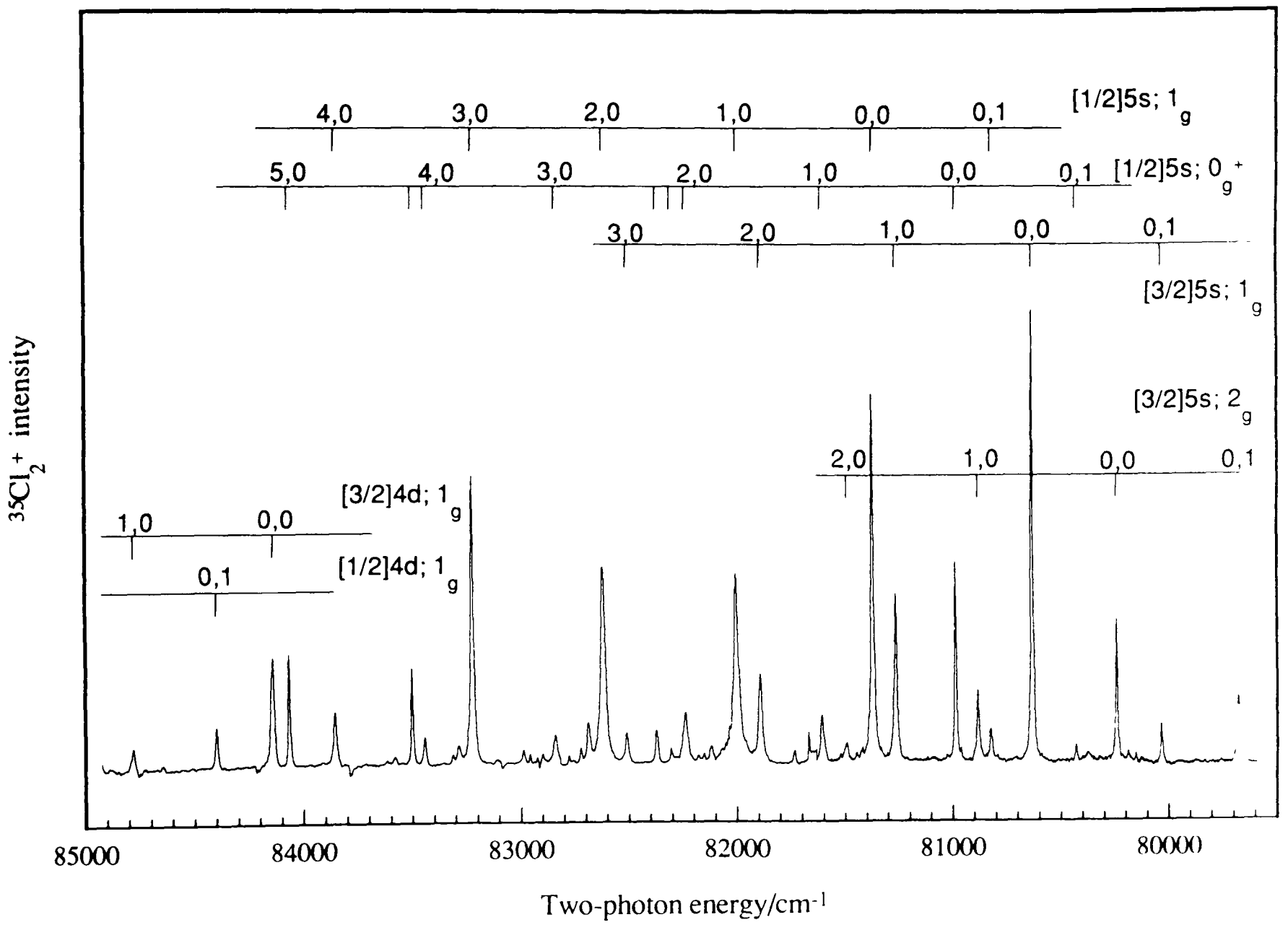

Figure 6–1: The (2+1) REMPI spectrum of $^{35}Cl_2$, recorded by collecting the $^{35}Cl_2^+$ ion signal, between 79600 cm^{-1} and 84800 cm^{-1}.

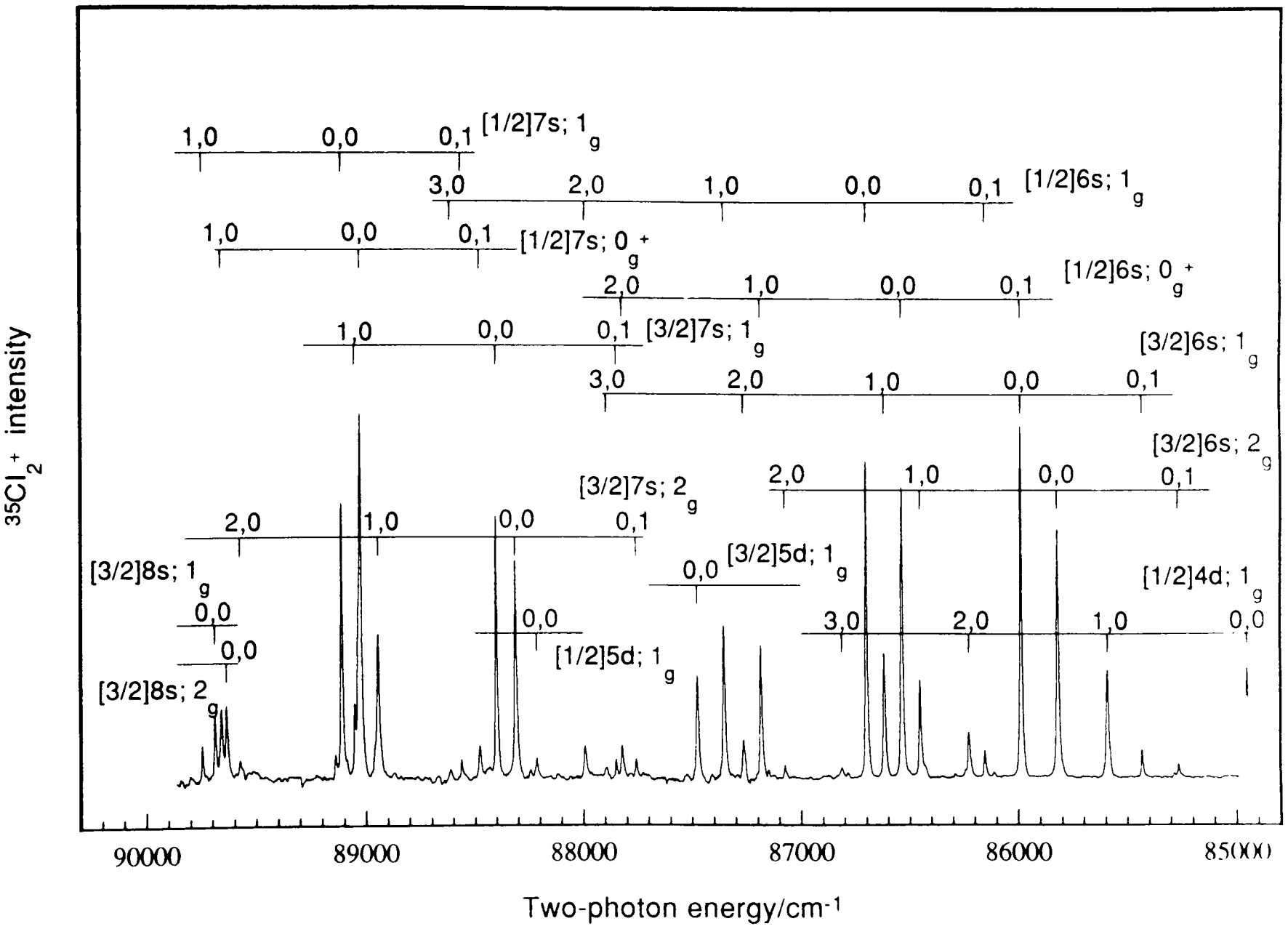

Figure 6–2: The (2+1) REMPI spectrum of $^{35}Cl_2$, recorded by collecting the $^{35}Cl_2^+$ ion signal, between 84800 cm^{-1} and 90000 cm^{-1}.

power dependence which indicates that a real intermediate state was accessed at the first photon level.

The spectra in Figure (6.1) and (6.2) show a number of Rydberg progressions whose band positions are listed in Tables (6.1) and (6.2). The vibrational spacings of a Rydberg state should be similar to that of the ionic core state to which the Rydberg series converge i.e. $\sim$ 645 cm^{-1} for the X $^2\Pi_g$ ion. The lowest energy band observed in each progression is assigned as the electronic origin. Isotopic shifts confirmed these assignments.

The assignment of a Rydberg state is based on the effective quantum number (n-δ) calculated from equation (1.2) in chapter one. These values, calculated using the IPs of the $[^2\Pi_{3/2}]_g$ and $[^2\Pi_{1/2}]_g$ ionic cores [12] of 92616 cm^{-1} and 93366 cm^{-1}, respectively, are presented in Table (6.3). It was reported previously for Br_2 and I_2, that the quantum defect (δ) of an electron in a particular Rydberg orbital is essentially the same irrespective of whether the ionic core is molecular or atomic [9][10]. Hence the assignments are made from comparison of the (n - δ) values obtained in the present studies with those of atomic chlorine [13]. Since the lowest Rydberg states must have a *gerade* core, resulting from the promotion of an electron from a *gerade* (anti-bonding) π orbital to a Rydberg orbital, the latter must be *s* or *d* to maintain the overall *gerade* symmetry of the state, only *gerade* states being accessable in a two-photon transition from the ground state.

The coupling of the spin of the Rydberg electron with the core angular momentum, gives rise to $[^2\Pi_{3/2}]_c$ ns;2_g, $[^2\Pi_{3/2}]_c$ ns;1_g, $[^2\Pi_{1/2}]_c$ ns;1_g, and $[^2\Pi_{1/2}]_c$ ns;0_g^+ sub-states. The splitting of the *gerade* core states of Cl_2^+ $[(\sigma_g)^2(\pi_u)^4(\pi_g)^3]$ $^2H_{3/2g}$ and $^2\Pi_{1/2g}$ has been recorded recently by threshold photoelectron spectroscopy,

$\Omega_c$nl(Ω)\(v',v'')	(0,1)	(0,0)	(1,0)	(2,0)	(3,0)	(4,0)	(5,0)
$^2\Pi_{3/2}$ 4s;†	-	-	-	64290*	64942*	-	66233*
$^2\Pi_{1/2}$ 4s;(1_g)†	63469*	64026*	64678*	65340*	65992*	66637*	67277*
$^2\Pi_{3/2}$ 3d;(1_g)	-	75922	76627	-	-	78570*	79180*
$^2\Pi_{1/2}$ 3d;(1_g)	-	76781	77474	78201	78839	79483	-
$^2\Pi_{3/2}$ 5s;(2_g)	79687	80228	80860	81484	-	-	-
$^2\Pi_{3/2}$ 5s;(1_g)	80044	80610	81248	81875	82497*	-	-
$^2\Pi_{1/2}$ 5s;(0_g^+)	-	80966	81600	82220	82840	83448	84058
$^2\Pi_{1/2}$ 5s;(1_g)	-	81358	81980	82608	83232	83850	84483*
$^2\Pi_{3/2}$ 4d;(1_g)	-	84133	84772	-	-	-	-
$^2\Pi_{1/2}$ 4d;(1_g)	-	84949	85590	86228	86832	-	-
$^2\Pi_{3/2}$ 6s;(2_g)	85263	85817	86454	87085	-	-	-
$^2\Pi_{3/2}$ 6s;(1_g)	85431	85986	86623	87254	87888	-	-
$^2\Pi_{1/2}$ 6s;(0_g^+)	-	86540	87177	87814	-	-	-
$^2\Pi_{1/2}$ 6s;(1_g)	86151	86706	87342	87974	-	-	-
$^2\Pi_{3/2}$ 5d;(1_g)	-	87464	88096*	-	-	-	-
$^2\Pi_{1/2}$ 5d;(1_g)	-	88200	88833*	-	-	-	-
$^2\Pi_{3/2}$ 7s;(2_g)	87749	88298	88934	89570	-	-	-
$^2\Pi_{3/2}$ 7s;(1_g)	87840	88387	89025	-	-	-	-
$^2\Pi_{1/2}$ 7s;(0_g^+)	88463	89016	89654	-	-	-	-
$^2\Pi_{1/2}$ 7s;(1_g)	88548	89099	89740	-	-	-	-
$^2\Pi_{3/2}$ 8s;(2_g)	89070	89630	-	-	-	-	-
$^2\Pi_{3/2}$ 8s;(1_g)	89128	89682	-	-	-	-	-

Table 6–1: Band positions of the gerade Rydberg states of $^{35}Cl_2$ isotopomer.

† from chapter five.

(*) seen only *via* the atomic $^{35}Cl^+$ ion signal.

$\Omega_c$nl(Ω)\(v′,v″)	(0,1)	(0,0)	(1,0)	(2,0)	(3,0)	(4,0)
$^2\Pi_{1/2}$ 4s;(1_g)†	63476*	64022.8*	64669*	65321*	65965*	66599.7*
$^2\Pi_{3/2}$ 3d;(1_g)	-	75918.5	-	-	-	-
$^2\Pi_{1/2}$ 3d;(1_g)	-	76784.7	77467.7	-	-	-
$^2\Pi_{3/2}$ 5s;(2_g)	79680	80228.4	80850	81467.5	-	-
$^2\Pi_{3/2}$ 5s;(1_g)	80051.5	80609.8	81238	81858.9	-	-
$^2\Pi_{1/2}$ 5s;(0_g^+)	-	80965	81593	82202	82819	83412
$^2\Pi_{1/2}$ 5s;(1_g)	-	81357	81971	82589	83207	83815
$^2\Pi_{3/2}$ 4d;(1_g)	-	84131.8	84766	-	-	-
$^2\Pi_{1/2}$ 4d;(1_g)	-	84947.3	85584.8	86207	86796	87460.9
$^2\Pi_{3/2}$ 6s;(2_g)	85269	85816	86445	87067	-	-
$^2\Pi_{3/2}$ 6s;(1_g)	85437.6	85984.9	86613	87237	-	-
$^2\Pi_{1/2}$ 6s;(0_g^+)	-	86538.9	87167.5	87795.7	-	-
$^2\Pi_{1/2}$ 6s;(1_g)	86157.8	86706.7	87332	87965	-	-
$^2\Pi_{3/2}$ 7s;(2_g)	87755.9	88296.8	88926.5	89548.8	-	-
$^2\Pi_{3/2}$ 7s;(1_g)	87847.6	88384.3	-	-	-	-
$^2\Pi_{1/2}$ 7s;(0_g^+)	88469	89015.3	89643	-	-	-
$^2\Pi_{1/2}$ 7s;(1_g)	88556	89098.9	89731.8	-	-	-
$^2\Pi_{3/2}$ 8s;(2_g)	-	89628	-	-	-	-
$^2\Pi_{3/2}$ 8s;(1_g)	89135	89682	-	-	-	-

Table 6–2: Band positions of the gerade Rydberg states of $^{35}Cl^{37}Cl$ isotopomer.

† from chapter five.

$\bar{\nu}/(cm^{-1})$	n-δ [3/2]core	Assignment nl(Ω)	n- δ [1/2]core	Assignment nl(Ω)
62970*	1.92	4s		
64026*			1.93	4s(1_g)
75922	2.56	3d(1_g)		
76784			2.57	3d(1_g)
80228	2.98	5s(2_g)		
80610	3.02	5s(1_g)		
80966			2.97	5s(0_g^+)
81358			3.02	5s(1_g)
84133	3.59	4d(1_g)		
84949			3.61	4d(1_g)
85817	4.02	6s(2_g)		
85986	4.07	6s(1_g)		
86540			4.01	6s(0_g^+)
86708			4.06	6s(1_g)
87464	4.62	5d(1_g)		
88200			4.61	5d(1_g)
88298	5.04	7s(2_g)		
88387	5.09	7s(1_g)		
89016			5.02	7s(0_g^+)
89099			5.07	7s(1_g)
89630	6.06	8s(2_g)		
89682	6.11	8s(1_g)		

Table 6–3: Assignments of the origins of the *gerade* Rydberg states of $^{35}Cl_2$. (*) from chapter five.

and found to be $\sim$ 750 cm^{-1} [12]. Core assignments were made on this reported splitting. In previous studies on Br_2 and I_2, the 1_g states, when $n \geq 5$ were three times more intense than 2_g or 0_g^+ states, also they occur at higher energies. In this work Cl_2 shows a similar pattern. The assignments were made on these considerations and are given in Table (6.3).

6.3.1 The *ns* Rydberg States

The *ns* Rydberg states show regular vibrational spacings smoothly decreasing as v′ increases with ω_e values for all the states of 635 $\pm$5 cm^{-1}. The accuracy of the measurements was $\pm$ 2 cm^{-1}. The ionic core splittings, between the $[^2\Pi_{3/2}]_c$ns; 1_g and $[^2\Pi_{1/2}]_c$ns; 1_g states, decrease from 748 cm^{-1} to 718 cm^{-1} to 712 cm^{-1} as n increases from 5 to 7. These compare with the measured splitting of the ground state of the molecular ion of $\sim$ 750 cm^{-1} [12]. The $[3/2]_c$ns 2_g - 1_g and $[1/2]_c$ns 0_g^+ - 1_g spin-orbit splittings are the same, to within $\pm$ 5 cm^{-1}, and decrease from 387 cm^{-1} to 168 cm^{-1} to 91 cm^{-1} to 52 cm^{-1} as n increases from 5 to 8. The vibrational envelopes of most progressions agree with the Franck-Condon factors for an unperturbed Rydberg state, where the origin (0,0) band has the strongest intensity, and only transitions to v′ = 0-3 are seen. These features of the *ns* Rydberg states suggest that most of them are regular, with few perturbations apparent at the energy region covered. However, the $[^2\Pi_{1/2}]_c$ 5s states have unusual vibrational envelopes and this will be discussed in detail later.

6.3.2 The *nd* Rydberg States

The *nd* Rydberg series observed in Figure (6.1) and (6.2) are much weaker than the *ns* Rydberg series. Figure (6.3) shows the spectrum between 84900 cm^{-1} and 89200 cm^{-1} recorded on the $^{35}Cl^+$ mass channel. In this spectrum the *nd* Rydberg bands are relatively much stronger. It becomes apparent that the absolute intensities of the *nd* states are stronger in the spectrum recorded on the $^{35}Cl^+$ mass channel

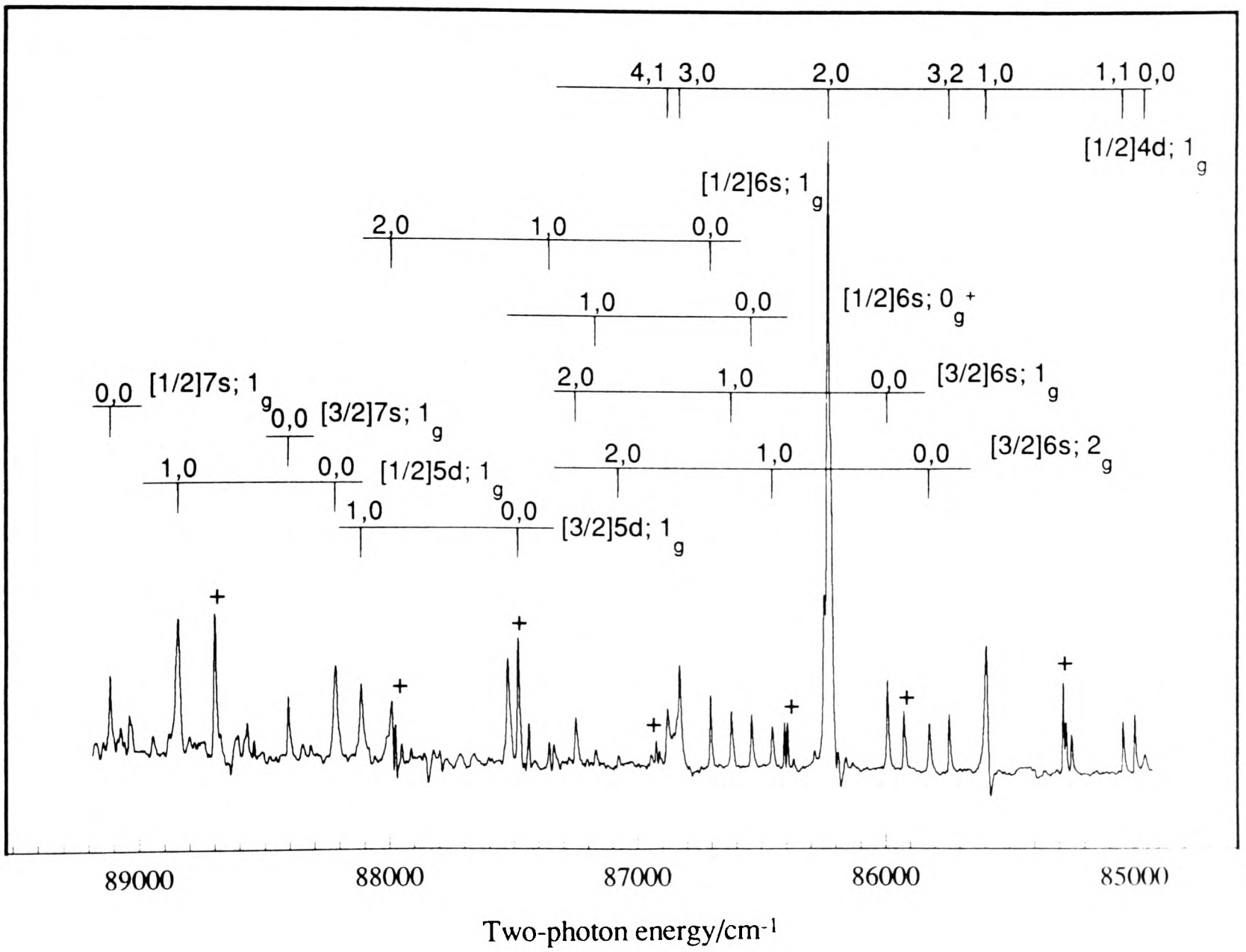

Figure 6–3: The (2+1) REMPI spectrum of $^{35}Cl_2$, recorded by collecting the $^{35}Cl^+$ ion signal, between 84800 cm^{-1} and 89300 cm^{-1}. The +'s denote bands from HCl impurity.

than those recorded on the $^{35}Cl_2^+$ mass channel, whereas the opposite is true for ns bands (see below). The (2,0) band of the $[^2\Pi_{1/2}]_c$ $4d$ progression in Figure (6.3), shows an unusually strong intensity. Both observations will be explained in the next section.

Two $3d$ states, one based on each core, have been observed and will be discussed in detail in the next section. It is assumed that these $3d$ states undergo a strong homogeneous interaction with another electronic state, most likely the $\beta 1_g$ ion-pair state, and as a consequence are expected to have 1_g symmetry. The quantum defects of the $4d$ and $5d$ states observed in Figure (6.1) and (6.2) are consistent with the states being the analogues of the observed $3d$ states. However, there is no additional information with which to confirm the 1_g assignments and these must remain provisional.

6.3.3 Rydberg/Ion-Pair State Interactions

The long $\beta 1_g$ ion-pair state progression discussed in the previous chapter, which covered an energy region between 71000 cm^{-1} and 77000 cm^{-1} shows no significant shifts in band positions even when bands are coincident with a $[^2\Pi_{1/2}]_c 4s$; 1_g Rydberg state band. Hence no obvious interaction is occuring.

In Figure (6.4), the (2+1) REMPI spectrum of $^{35}Cl_2$ between 76000 cm^{-1} and 80000 cm^{-1} shows strong interactions. In this energy region the $3d$ Rydberg states are crossed by the $\beta 1_g$ and the other ^3P ion-pair states, near to their electronic origins. In previous studies on I_2 and ICl, such crossings between the inner walls of the ion-pair states and the Rydberg states, lead to an enhancement of the intensities of the ion-pair bands, and the ion-pair and Rydberg band positions are shifted [14][15]. Similar effects are seen in this work. The $\beta 1_g$ ion-pair state bands above $v' = 135$, have their intensity enhanced, especially $v' = 138$, 151, and 162 bands, due to this interaction. Lying next to each of these bands, is another

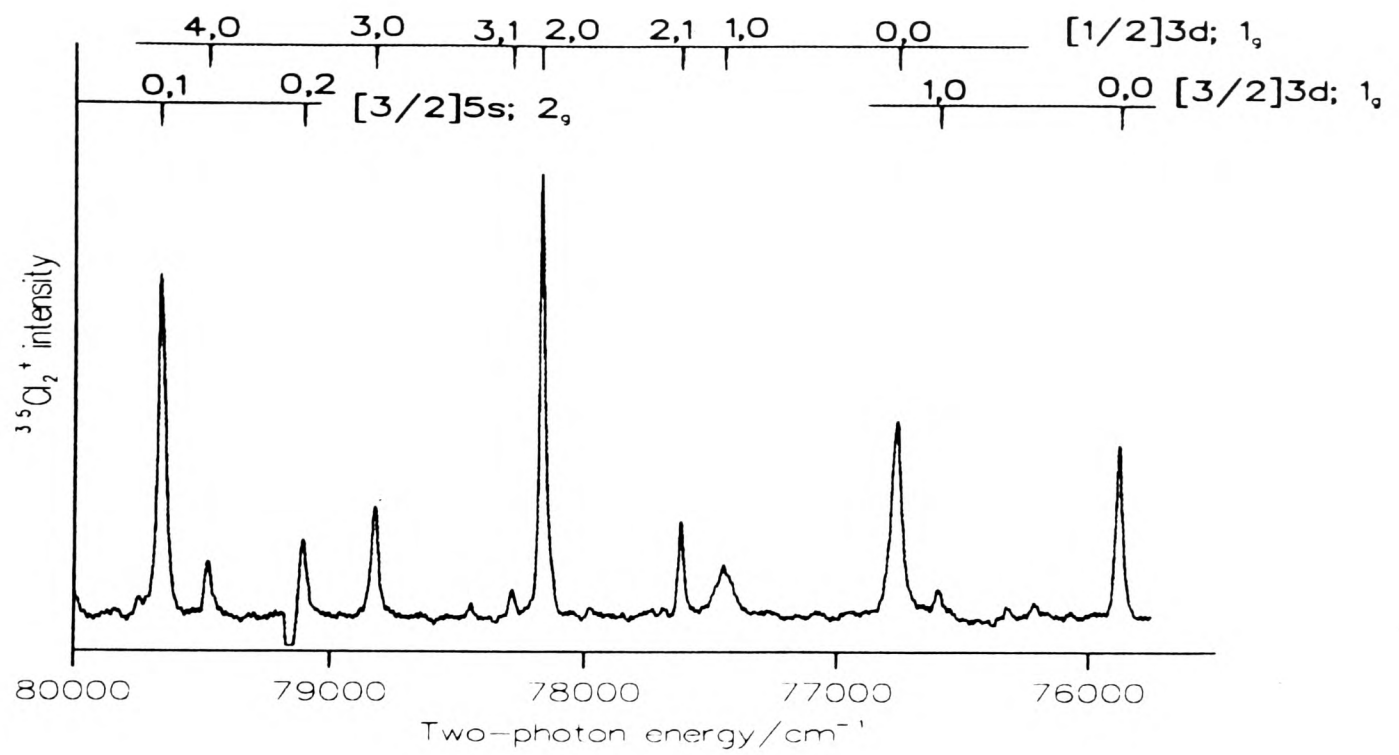

Figure 6–4: The (2+1) REMPI spectrum of $^{35}Cl_2$, between 75800 cm^{-1} and 80000 cm^{-1}. The upper and the lower traces were recorded by collecting the $^{35}Cl_2^+$ ion signal and $^{35}Cl^+$ ion signal, respectively. The arrows in the lower trace indicate regions of strong interaction.

strong band, and these were assigned as $3d$ Rydberg bands. Since the interaction is so strong, it must be homogeneous, therefore both interacting states must have 1_g symmetry. In the following chapter the homogeneous interaction between a Rydberg state and an ion-pair state in I_2 will be discussed. It will be shown that ionisation of all of the vibronic bands of I_2, produces I^+, while I_2^+ is only seen from vibronic bands which have a large Rydberg component.

The (2+1) REMPI spectrum of $^{35}Cl_2$, recorded on the $^{35}Cl_2^+$ mass channel is shown in the upper trace of Figure (6.4). Two Rydberg progressions can be assigned, with their electronic origins at 75922 cm^{-1} and 76781 cm^{-1}; isotopic shifts have confirmed these assignements. The two origins have a splitting of $\sim$ 800 cm^{-1}, which is close to that of the $[^2\Pi_{3/2}]_g$ and $[^2\Pi_{1/2}]_g$ ionic cores. The quantum defects calculated for these two origins is 0.44, which assign them as $3d$ Rydberg states. The $[^2\Pi_{3/2}]_g$ and $[^2\Pi_{1/2}]_g$ progressions extend up to (1,0) and (4,0) bands respectively. The lower trace of Figure (6.4) shows the spectrum in this energy region recorded on the $^{35}Cl^+$ mass channel. From Figure (6.4) it can be seen that all of the $3d$ Rydberg bands in the upper trace are also seen in the lower one. The $[^2\Pi_{1/2}]_c$ 3d;1_g (2,0), (3,0) and (4,0) bands coincide with an enhancement in the intensities of the nearest ion-pair state bands. The Rydberg band and the ion-pair band to which it is coupled most strongly are denoted by arrows in the lower trace of Figure (6.4). However, it is obvious that all bands lying nearby are coupled to some extent, so they can only be described as the bands which have the largest Rydberg component. The ion-pair state band intensities are enhanced in three other regions of the spectrum in the lower trace of Figure (6.4). These regions coincide with the predicted positions of the (4,0), (5,0) and (6,0) transitions of the $[^2\Pi_{3/2}]_c$ 3d;1_g state progression, from an extrapolation of the (0,0) and (1,0) bands. It is not clear why the $^{35}Cl_2^+$ ions were not seen from the coupled vibronic bands in this progression. Table (6.4) gives the positions and assignments of the bands observed in Figure (6.4). It is apparent from the spacings between the adjacent bands, how insertion of a Rydberg level into the ion-pair manifold compresses the spacings of the levels on either side of it.

v'*	Band positions cm^{-1}	v'*	Band positions cm^{-1}	v'*	Band positions cm^{-1}
110	75580	128	77283	146	78738
111	75684	129	77365	147	78800
112	75782	$1,0[1/2]_c$	77474	$3,0[1/2]_c$	78839
113	75881	$2,1[1/2]_c$	77648	148	78907
$0,0[3/2]_c$	75922	133	77712	149	78979
114	75981	134	77798	150	79048
115	76078	135	77875	151	79118
116	76175	136	77959	$5,0[3/2]_c$	79180
117	76267	137	78039	152	79219
118	76365	138	78118	153	79270
119	76459	139	78154	154	79335
120	76553	$2,0[1/2]_c$	78201	155	79400
$1,0[3/2]_c$	76627	$3,1[1/2]_c$	78280	156	79464
121	76646	140	78300	$4,0[[1/2]_c$	79483
122	76737	141	78357	160	79704
$0,0[1/2]_c$	76781	142	78432	161	79768
123	76825	143	78515	162	79826
124	76919	$4,0[3/2]_c$	78570	$6,0[3/2]_c$	79868
125	77014	144	78595	163	79905
126	77103	$5,0[3/2]_c$	78628	164	79968
127	77193	145	78666	165	80034
				166	80102

Table 6–4: Vibrational assignments and observed bands positions of $^{35}Cl_2$,between 75000 cm^{-1} and 80100 cm^{-1}.

(*) v' of the $\beta 1_g$ state unless stated otherwise.

The general overall excitation scheme for regions of Rydberg/ion-pair interaction can be considered in three stages. The two-photon oscillator strength is usually carried by the Rydberg state, both states can have favourable Franck-Condon factors and, efficient ionisation occurs from the ion-pair state. Ionisation of ion-pair states is believed to originate from their outer wall, to go *via* unbound states and to generate mainly atomic ions.

An expansion of the energy region covered in this work, showing the relevant potential curves of the lowest *gerade* ion-pair and Rydberg states is illustrated in Figure (6.5). It can be seen that the $\beta 1_g$ ion-pair state crosses the singlet $[^2\Pi_{1/2}]_c$ 4s;1_g Rydberg state at 70500 cm^{-1}, corresponding to $v'_{Ryd} = 11$ and $v'_{i.p} = 67$. The vibrational spacings in both states are fairly regular in this energy region which indicates that no significant interaction has occured, as expected because of the nature of the two states involved (i.e singlet and triplet). Nevertheless considering that the $[^2\Pi_{3/2}]_c$4s; 1_g Rydberg state and the $\beta 1_g$ ion-pair state have the same multiplicity, both being triplet states, an interaction between these two states is expected. However, no shifts in the vibrational levels of the ion-pair state were observed. The reason why the interaction between these two states is weak, is probably due to the $\beta 1_g$ ion-pair state having the predominantly 2242 configuration, which can not be related to the $[243]_c$ *ns* Rydberg state by a two-electron shift. In contrast, the two triplet $3d$ states are crossed by the $\beta 1_g$ ion-pair state near to $v' = 4$ of the Rydberg states, this leads to strong interactions between them, as shown in the lower trace of Figure (6.4). It is not understood why these crossings give rise to strong interactions when the $[^2\Pi_{3/2}]_c$4s; $1_g/\beta 1_g$ crossing does not, but it seems that the general trend in halogens and interhalogens is for the strongest ion-pair/Rydberg interactions to involve the lowest *nd* Rydberg states in each molecule.

When the inner wall of the $\beta 1_g$ ion-pair potential is extrapolated to higher energies, it crosses the $4d$ Rydberg state potentials around $v' = 2$. The strong intensity of the (2,0) band of the $[^2\Pi_{1/2}]_c$ 4d; 1_g state in Figure (6.3) recorded on

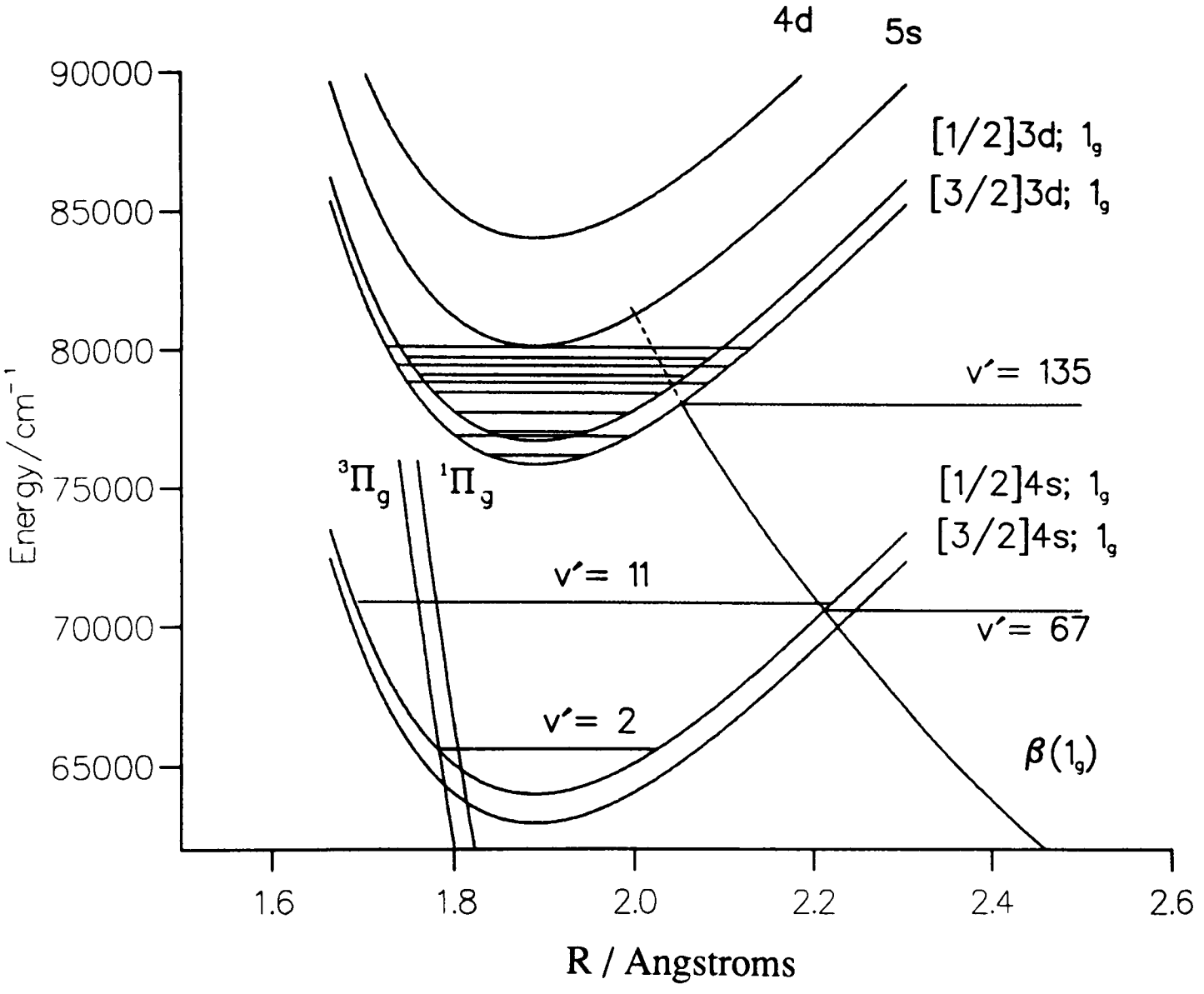

Figure 6–5: The potential energy curves of the relevant states, showing the regions where they cross.

the $^{35}Cl^+$ mass channel, indicates an interaction with the $\beta 1_g$ ion-pair state. Although the vibrational bands of the $[^2\Pi_{3/2}]_c$ 4d; 1_g state, show no enhancement in intensity in the $^{35}Cl_2^+$ spectrum (Figures (6.1) and (6.2)), they appear much stronger in the $^{35}Cl^+$ mass spectrum. The (1,0) bands in both $5d$ Rydberg states show similar picture, where they are only seen in the $^{35}Cl^+$ spectrum (Figure (6.3)).

Another example of Rydberg/ion-pair vibronic coupling was seen from the $[^2\Pi_{1/2}]_c$ 5s state progressions. The (2,0) and (3,0) vibrational bands of the 1_g state and (5,0) band of the 0_g^+ state progressions have strong intensities in the $^{35}Cl_2^+$ spectrum (Figure (6.1)) and they show stronger intensities than their respective band origins in the $^{35}Cl^+$ mass spectrum. The extrapolated β 1_g ion-pair state in Figure (6.5), shows that it crosses the 1_g Rydberg state, probably causing perturbations in the (2,0) and (3,0) bands. Since the potential energy curves of the $E0_g^+(^3P_2)$ and $f0_g^+$ $(^3P_0)$ ion-pair states have not been established in this energy region, it is not known which of these states is responsible for the coupling with the 0_g^+ Rydberg state.

As shown in Figure (6.5), the $^3\Pi_{1_g}$ repulsive valence state should cross the inner wall of the $3d$ Rydberg states around $v' = 4$. It is possible that avoided crossings are formed between the states involved, resulting in a steepening of the Rydberg potentials. The spacings of the vibrational levels supported by these potentials will then be greater than those of an unperturbed state and this is confirmed by the (1,0) - (0,0) separations of the $3d$ states of $\sim$ 700 cm^{-1}, c.f. 635 cm^{-1} for a typical unperturbed Rydberg state.

Peyerimhoff and Buenker [16], predicted significant interactions between the triplet $4s$ Rydberg states and the $^3\Pi_g$ ion-pair states. The $D'2_g$ ion-pair state which has a 1432 configuration should couple strongly with the $[243]nl$ Rydberg states. Hence, a possible alternative assignment for the interaction observed around 79000 cm^{-1}, is that all of the bands between 77500 cm^{-1} and 80000 cm^{-1} (Figure (6.4)) have 2_g symmetry. The original assingment of those bands as having 1_g symmetry

is based on a consideration of the positions of the ion-pair bands being a continuation of the $\beta 1_g$ ion-pair state progression observed below 77500 cm^{-1}. While the spacings in the $D'2_g$ are not determined in this energy region they are expected to be not much different from those of the $\beta 1_g$ state. Therefore the 2_g symmetry assignment is possible. In I_2 [14] a strong coupling between the $[^2\Pi_{3/2}]_c$ 5d;2_g Rydberg state and the $D'2_g$ $^3P_2$ ion-pair state has been observed.

It should be emphasised that the assignment of the 4d and 5d Rydberg states, having 1_g symmetry was made on the assumptions that they have the same Ω value as that of $3d$ states. It becomes clear that if the $3d$ states were actually of 2_g symmetry, then the $4d$ and $5d$ states assignment must be reconsidered.

6.3.4 Polarisation Effects

Some interesting changes to the spectrum of I_2 were observed when it was recorded with circularly polarised (CP) rather than linearly polarised (LP) light. The intensities of the 1_g bands, with the exception of those where n had its lowest value, decreased to almost zero when recorded with CP light. These observations do not agree with the line strengths derived by Bray and Hochstrasser [17] for coherent two-photon absorptions where all branches of an $0_g \rightarrow 1_g$ transitions recorded with CP should be greater by a factor of 1.5 than those recorded with LP. Initially it was believed that the 1_g states undergo an interaction with a repulsive state with the resultant formation of atomic iodine and that the loss of intensity was a consequence of the inefficient ionisation of the atoms by CP light. More recently the same polarisation effects have been seen in the Rydberg states of the I_2-Ar van der Waals complex [18]. However, in the spectra of the complex the polarisation effects were also observed when the I_2-Ar^+ species was collected. These results eliminated the original explanation involving the formation of atoms.

A comparison of the spectra of $^{35}Cl_2$ in the region of the $5s$ Rydberg states, recorded with LP and CP light, is shown in Figure (6.6). Again the intensities of the 1_g bands decrease by a large amount in the CP spectrum whereas those of the 2_g and 0_g bands increase by a small factor. The higher *ns* states exhibit the same behaviour. As was observed in I_2, polarisation has no appreciable effect on the lowest *ns* and *nd* states. At this stage no explanation for this unusual effect which is common to both I_2 and Cl_2, can be offered.

6.4 Conclusion

In this chapter the lower gerade Rydberg states of Cl_2 were investigated. In general the spectra show a close resemblance with those of the other halogens. Each $[^2\Pi_{\omega_c}]_g$ *ns* cluster is observed to have four Ω components, i.e. 2_g, $2x(1_g)$, and 0_g^+. The observed *nd* series are generally weaker and only two components were observed. The *ns* series show regular vibrational spacings, whereas the *nd* series are perturbed. This behaviour is consistent with the other halogens. It is concluded that the *nd* series interact strongly with one or more ion-pair states and probably also with the repulsive valence states.

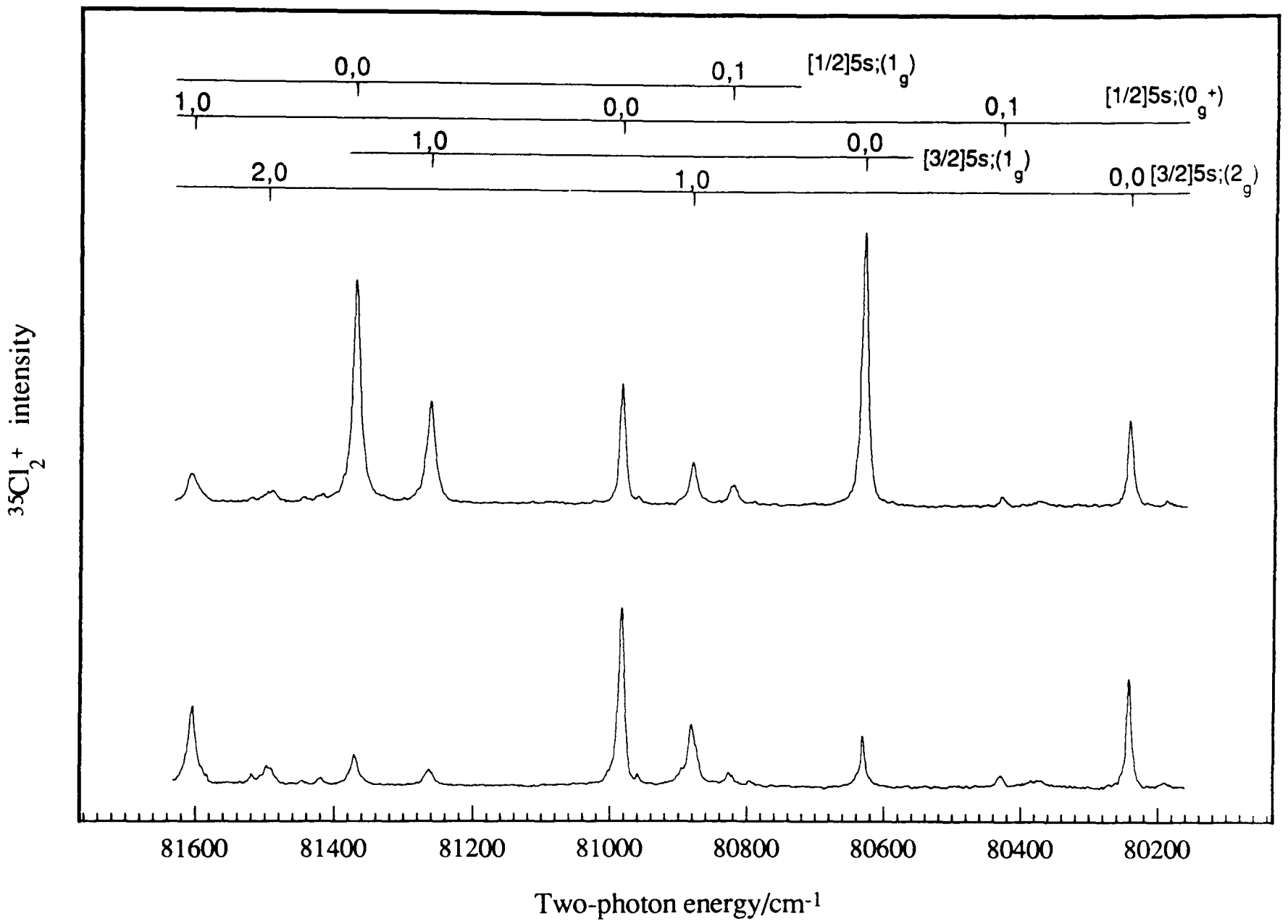

Figure 6–6: A spectrum showing the effect of linear (upper trace) and circular (lower trace) polarisation on the $5s$ Rydberg transitions. The 1_g components are diminished in circular polarisation.

6.5 References

(1) A.E. Douglas, Can.J.Phys., 59 (1981) 835.

(2) T. Möller, B. Jordan, P. Gurther, G. Zimmerer, D. Haaks, J. Le Calve, and M. Castex, Chem.Phys., 76 (1983) 295.

(3) B.G. Koenders, D.M. Wieringa, G.J. Kuik, Karel E. Drabe and C.A. De Lange, Chem. Phys., 129 (1989) 41.

(4) J. Jureta, S. Cvejanovic, M. Kurepa, and D. Cvejanovic, Z. Phys. A. 304 (1982) 134.

(5) D.Spence, R.H. Huebner, H. Tanaka, M.A. Dillon and R.G. Wang, J. Chem. Phys., 80 (1984) 2989.

(6) R.J. Stubbs, T.A. York and J. Comer, J. Phys. B. 18 (1985) 3229.

(7) B.G. Koenders, S.M. Koechhoven, G.J. Kuik, K.E. Drabe and C.A. De Lange, J. Chem. Phys., 91 (1989) 6042.

(8) L. Li, R.J. Lipert, H. Park, W.A. Chupka and S.D. Colson, J. Chem. Phys., 88 (1988) 4608.

(9) T. Ridley, K.P. Lawley and R.J. Donovan, Chem. Phys., 148 (1990) 315.

(10) R.J. Donovan, R.V. Flood, K.P. Lawley, A.J. Yencha and T. Ridley, Chem. Phys., 164 (1992) 439.

(11) D. Maric, J.P. Burrows, R. Miller and G.K. Moortgat, J. Photochem. Photobiol. A:Chem., 70 (1993) 205.

(12) A.J. Yencha, A. Hopkirk, A. Hiraya, R.J. Donovan, J.G. Goode, R.R.J. Maier,G.C. King and A. Kvaran, J. Phys. Chem., 99 (1995) 7231.

(13) A.M. Cantu, W.H. Parkinson, T. Grisendi and G. Tagliaferri, Physica Scripta, 31 (1985) 579.

(14) K.P. Lawley, T. Ridley, Z. Min, P.J. Wilson, M.S.N. Al-Kahali and R.J. Donovan, Chem. Phys., 197 (1995) 37.

(15) R.D. Donovan, J.G. Goode, K.P. Lawley, T. Ridley and A.J. Yencha, J. Phys.Chem., 98 (1994) 2236.

(16) S.D. Pererimhoff and R.J. Buenker, Chem. Phys., 57 (1981) 279.

(17) R.G. Bray and R.M. Hochstrasser, Mol. Phys., 31 (1976) 1199.

(18) M.C.R. Cockett, J.G. Goode, R.R.J. Maier, K.P. Lawley and R.J. Donovan, J. Chem. Phys., 101 (1994) 126.

Chapter 7

Vibronic Coupling Between The $[^2\Pi_{3/2}]_c$ 7s; 1_g Rydberg State and the $\beta 1_g$ Ion-pair State Observed by (2+1) Resonance Enhanced Multiphoton Ionisation Spectroscopy

7.1 Introduction

The crossings of the inner walls of the ion-pair states with Rydberg states of the same symmetry can lead to the formation of avoided crossings between the states involved, resulting in extensive vibronic coupling and borrowing of intensity. The first v′ level to show strong coupling indicates the position where the two states cross. In general the Rydberg state is strongly accessed from the ground state and the ion-pair vibronic levels appear as satellites around each Rydberg v′ level from which they have borrowed intensity. The mass-resolved jet-cooled resonance enhanced multiphoton ionisation techniques can throw light on the vibronic coupling between the Rydberg and ion-pair states.

In chapter five an example of these interactions, namely that between the $\beta 1_g$ and 3d Rydberg states in Cl_2 was illustrated. It was difficult to study this region in Cl_2 because the spectra were congested. In this chapter the vibronic coupling between the $[^2\Pi_{3/2}]_c$ 7s; 1_g Rydberg state and the $\beta 1_g$ ion-pair state from the first cluster was studied between 62500 - 64500 cm^{-1}. In this case the interaction occurs in a non-congested region and will act as a model of a homogeneous coupling.

7.2 Experimental

The experimental setup is described in detail in chapter two. Here the rotationally and vibrationally cooled I_2 was generated by flowing 500 Torr of helium over I_2 at room temperature and passing the mixture through a pulsed nozzle. The frequency doubled output of the Rhodamine 101 dye covered the region 316 - 310 nm (two-photon energy 63250 - 64400 cm^{-1}). The dye fundamental was calibrated using the I_2 B $\leftarrow$ X fluorescence excitation spectrum. The spectra were normalised to the square of the laser power.

Ω_c nl; $\Omega_g \backslash (v',v'')$	**(0,0)**	**(1,0)**	**(2,0)**	**(3,0)**	**(4,0)**
$^2\Pi_{3/2}$ 7s; 2_g	62639	62872	63104	63335	63565
$^2\Pi_{3/2}$ 7s; 1_g	63332	63576	63806	64037	64269

Table 7–1: Band positions of the $^2\Pi_{3/2}$ 7s; 2_g and 1_g Rydberg states of I_2 observed in the 62500 - 64500 cm^{-1} energy region.

7.3 Results

The Rydberg states of I_2 up to the ionisation limit were reported previously by Donovan et al.[1], using (2+1) REMPI at room temperature in the 48000 - 85000 cm^{-1} energy region. The ns Rydberg states with n up to 11 and 8, based on the $[^2\Pi_{3/2}]_g$ and $[^2\Pi_{1/2}]_g$ ionic cores, respectively, were observed. Three 5d Rydberg states based on each core were also observed. The (2+1) REMPI spectrum of jet-cooled I_2 between 62500 - 64500 cm^{-1}, is shown in Figure (7.1), the upper trace was recorded on the I_2^+ mass channel, and the lower trace was recorded on the I^+ mass channel. The progressions in Figure (7.1) were assigned as the two overlapping $[^2\Pi_{3/2}]_c$ 7s; 2_g and $[^2\Pi_{3/2}]_c$ 7s; 1_g Rydberg states, with origins at 62639 cm^{-1} and 63332 cm^{-1} and ω_e values of 241±2 cm^{-1} and 238±2 cm^{-1} respectively. The band origin of the $[^2\Pi_{3/2}]_c$ 7s; 1_g Rydberg state overlaps exactly the $v' = 3$ of the $[^2\Pi_{3/2}]_c$ 7s; 2_g Rydberg state. The band positions of both Rydberg states are shown in Table (7.1). An expanded spectrum of the $[^2\Pi_{3/2}]_c$ 7s; 1_g Rydberg state from $v' = 0$-3, recorded on the I^+ mass channel is shown in Figure (7.2).

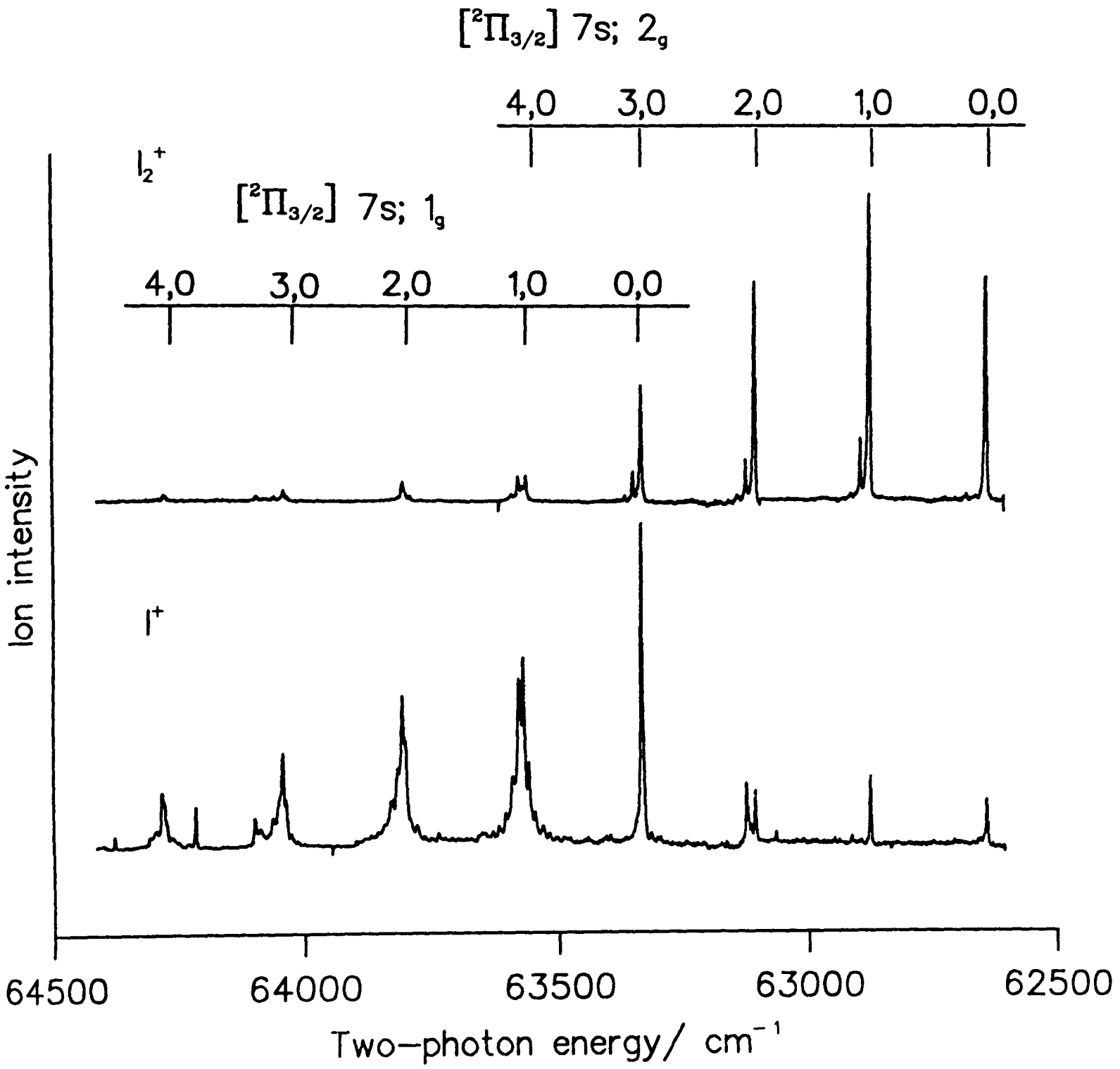

Figure 7–1: The (2+1) REMPI spectrum of I_2 in the 62500 - 64500 cm^{-1} energy region. The lower trace is recorded on the I^+ mass channel, and the the upper trace is recorded on the I_2^+ mass channel. Only Rydberg levels are seen in the I_2^+ spectrum. The I^+ spectrum shows both ion-pair and Rydberg vibrational levels.

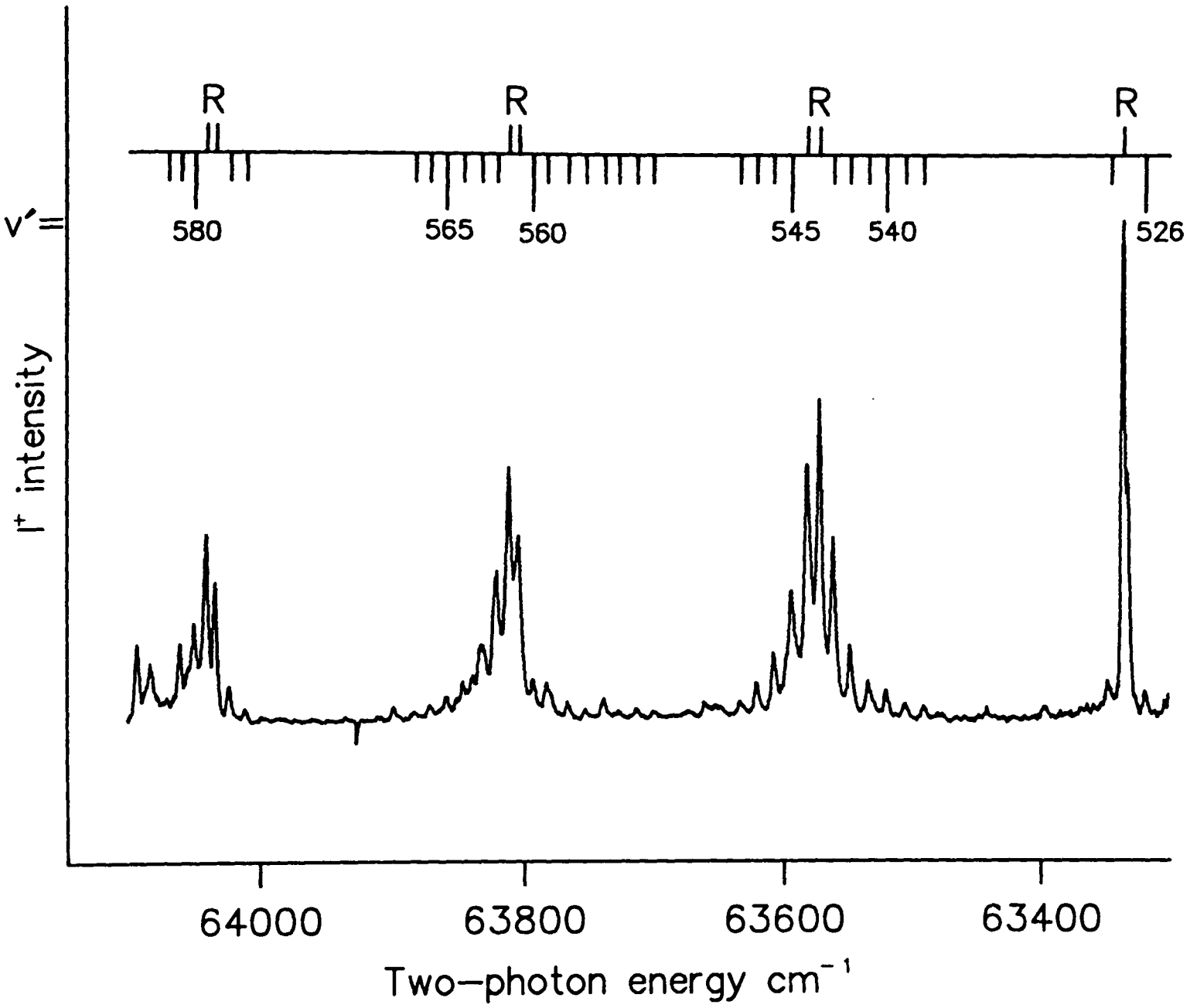

Figure 7–2: An expanded section of the spectrum recorded on the I^+ mass channel, showing the ion-pair levels of the $\beta 1_g$ state which appear as satellites around $v' \geq 1$ of the $[^2\Pi_{3/2}]_g$ 7s; 1_g Rydberg state. The vibrational numbering of the $\beta 1_g$ ion-pair state was taken from reference [2].

7.4 Discussion

Figure (7.1) shows the progressions of the $[^2\Pi_{3/2}]_c$ 7s; 2_g and 1_g Rydberg states. The former appears stronger in the I_2^+ channel, with regular spacings and sharp band contours: the weaker features appearing to the blue side of each of the vibrational bands are sequence bands. The Rydberg levels of the $[^2\Pi_{3/2}]_c$ 7s; 1_g state recorded at room temperature [1] did not show any ion-pair structure in the vicinity of each Rydberg level. The jet-cooled spectrum of I_2 in Figure (7.2), recorded on the I^+ mass channel shows a series of closely spaced ion-pair vibrational bands associated with each Rydberg band, in contrast with the room temperature spectrum where only a single broad peak was seen for each Rydberg band [1]. These closely spaced bands are due to vibronic coupling between the $[^2\Pi_{3/2}]_c$ 7s; 1_g Rydberg state and an ion-pair state and the ion-pair bands gain their intensity from these interactions. The measured average vibrational spacings of $\sim$ 14 cm^{-1} assign the ion-pair state as belonging to the first cluster of states that dissociate to $I^+(^3P_2) + I^-(^1S_0)$. The strong interaction between the states further indicates that it is homogenous in nature and labels the ion-pair state as having 1_g symmetry. As a result, it was assigned as the β state since this is the only ion-pair state from the first cluster with a 1_g symmetry. The spacings of the vibrational levels of the $\beta 1_g$ ion-pair state are shifted slightly when a Rydberg level coincides with them. The observed band positions are listed in Table (7.2). The interaction is weak at $v' = 0$, and is stronger at $v' = 1$ and above. This suggests that the crossing of the $\beta 1_g$ ion-pair state and the $[^2\Pi_{3/2}]_c$ 7s; 1_g Rydberg state potentials occurs around $v' = 1$. The $[^2\Pi_{3/2}]_c$ 7s; 1_g Rydberg state potential curve and that of the $\beta 1_g$ ion -pair state are shown in Figure (7.3). The knot points for the $\beta 1_g$ ion-pair state and the spectroscopic constants for the $[^2\Pi_{3/2}]_c$ 7s; 1_g Rydberg state are taken from Reference [2].

Another feature in which the ion signals of the two $[^2\Pi_{3/2}]_c$ 7s; 2_g and $[^2\Pi_{3/2}]_c$ 7s; 1_g

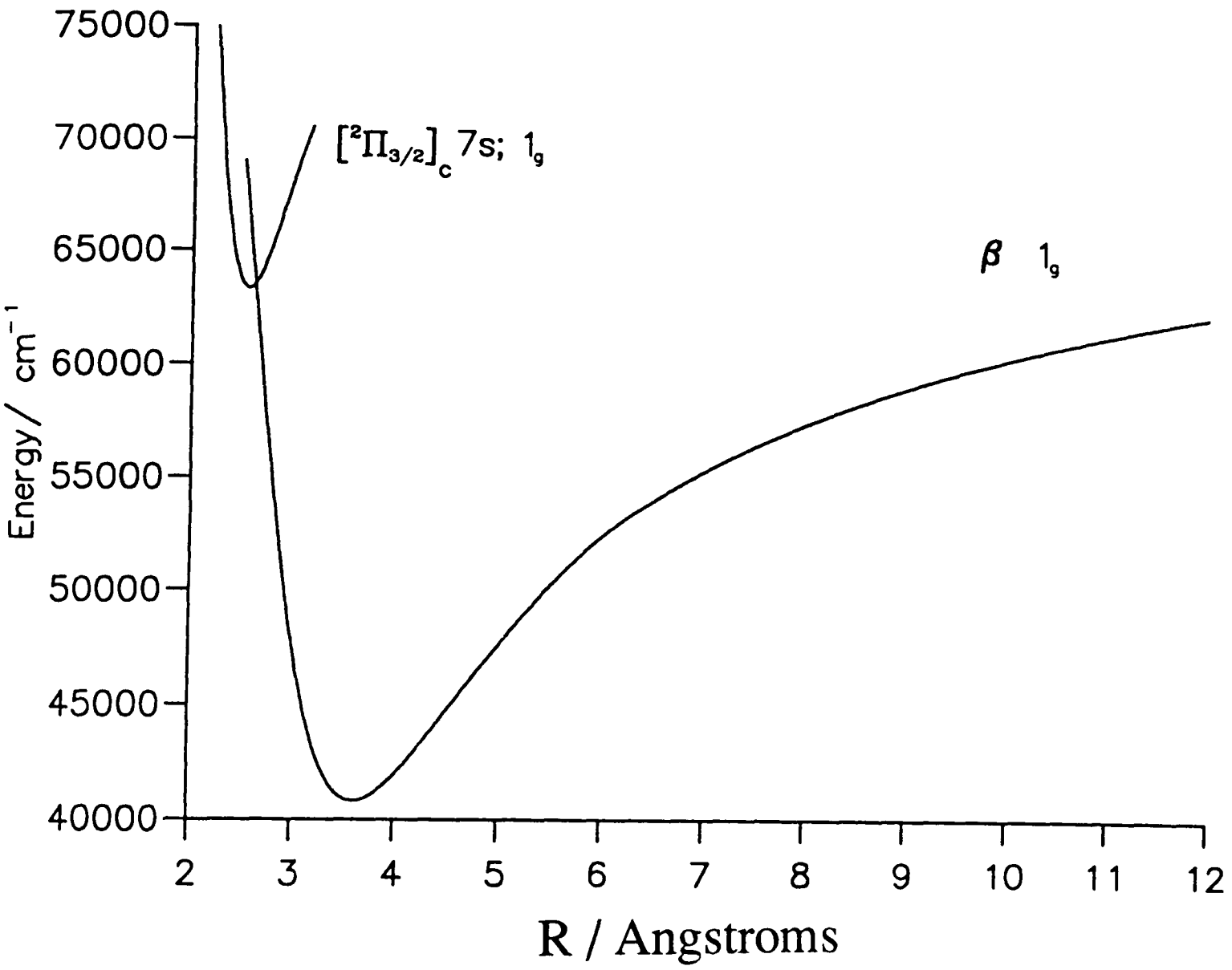

Figure 7–3: Potential energy curves of the $\beta 1_g$ ion-pair state and the $[^2\Pi_{3/2}]_g$ 7s; 1_g Rydberg state, showing the region where they cross.

v′	$\bar{\nu}_{obs}$ (cm^{-1})	$\Delta\bar{\nu}$ (cm^{-1})	v′	$\bar{\nu}_{obs}$ (cm^{-1})	$\Delta\bar{\nu}$ (cm^{-1})	v′	$\bar{\nu}_{obs}$ (cm^{-1})	$\Delta\bar{\nu}$ (cm^{-1})
523	63273.3				14.0	561	63803.2	
		13.3	547	63619.2		*(2,0)*	*63806.0 7s;1_g*	17.7
524	63286.6				12.7	562	63820.9	
		16.3	548	63631.9				10.5
525	63302.9				13.4	563	63831.4	
		13.8	549	63645.3				13.8
526	68316.7				13.4	564	63845.2	
			550	63658.7				14.7
536	63461.5				13.7	565	63859.9	
		15.4	551	63672.4				10.3
537	63476.9				13.3	566	63870.2	
		12.2	552	63685.7				12.6
538	63489.1				14.1	567	63882.8	
		13.4	553	63699.8				
539	63502.5				13.7	575	63985.9	
		14.9	554	63713.5				12.5
540	63517.4				13.0	576	63998.4	
		14.8	555	63726.5				11.8
541	63532.2				11.1	577	64010.2	
		15.5	556	63737.6				12.7
542	63547.7				14.5	578	64022.9	
		12.6	557	63752.1				10.6
543	63560.3				13.6	579	64033.5	
		14.1	558	63765.7		*(3,0)*	*64037.0 7s;1_g*	13.7
544	63574.4				14.9	580	64047.2	
(1,0)	*63576.0 7s;1_g*	17.1	559	63780.6				13.6
545	63591.5				12.2	581	64060.8	
		13.6	560	63792.8				13.1
546	63605.2				10.4	582	64073.9	

Table 7–2: Band positions of the $\beta 1_g$ ion-pair state and the 7s; 1_g Rydberg state observed in the 62500 - 64500 cm^{-1} energy region.

progressions differ remarkably is that the latter is almost completely composed of I^+, with only ~1 % of the molecular I_2^+ ion, whereas the former, under the same experimental conditions, gives 80 % I_2^+. It is an unexpected feature that the Ω = 1 Rydberg state gave very weak I_2^+ signal on ionisation, even the origin band which has little ion-pair structure and thus has predominantly Rydberg character. An explanation of these observations, lies in the different ionisation pathways from the ion-pair and Rydberg states. These observations suggest that ionisation from the ion-pair state gives predominantly atomic ions and is more efficient than ionisation of a Rydberg state, which gives a mixture of atomic and molecular ions. The reason why the whole 7s; 1_g REMPI spectrum is not stronger than the purely 7s; 2_g progression might be that all the vibrational levels of the 7s; 1_g Rydberg state are strongly predissociated.

The vibrational numbering of the $\beta 1_g$ ion-pair state levels observed was determined subsequently by the simulation of the vibronic coupling between the $\beta 1_g$ ion-pair state and the 7s; 1_g Rydberg state [2].

Linear and circular polarisation spectra were obtained for this energy region, and are shown in Figure (7.4). As can be seen, vibrational levels of the 1_g Rydberg state were diminished in intensity when circular polarisation is used. It was reported previously [1] that the intensities of all the 1_g bands above 62000 cm^{-1} were reduced to nearly zero when excited with circularly polarised light. The explanation given was that the 1_g Rydberg states are predissociated by a repulsive valence state to give atomic iodine which is then ionised. It is well known that coherent nonresonant ionisation of atoms is inhibited with circularly polarised light [3][4]. Recently Cockett et al [5], in a (2+1) mass-resolved REMPI excitation of I_2-Ar, reported that the spectrum of the I_2-Ar complex recorded on the (I_2^+-Ar) mass channel with circular polarisation showed the same loss in intensity for the 1_g state. The fact that the complex spectra show exactly the same behaviour with circularly polarised light as the uncomplexed I_2 suggests that the mechanism which accounts for this behaviour is the same in each case. As a result the explanation proposed for this phenomenon in I_2 is in doubt. Bray and Hochstrasser [6] have

predicted that in a two-photon transition, an increase in intensity by a factor of 1.5 is expected with circularly polarised light for all rotational branches with $\Delta\Omega$ = 0, $\pm$1, and $\pm$2, except for the Q branch of a $\Delta\Omega$ = 0 transition, which is J dependent and the intensity factor ranges from 0 to 0.25. This is clearly not the case here. This same phenomenon was observed in Cl_2 and mentioned in chapter five. At this stage no explanation can be given of this polarisation behaviour of the 1_g Rydberg states.

7.5 Conclusion

Previously reported (300K) Rydberg spectra did not show resolved ion-pair satellite structure in the vicinity of the Rydberg levels [1]. In this chapter it is shown that the use of mass-resolved resonance enhanced multiphoton ionisation techniques and jet cooling, in studying vibronic coupling in I_2, can yield resolved ion-pair structure. The Rydberg levels are much stronger when the recording is on the I_2^+ mass channel, whereas the ion-pair levels are stronger on the I^+ mass channel. Therefore, it is possible to distinguish between the Rydberg and the ion-pair levels, and a better interpretation of the spectra becomes possible.

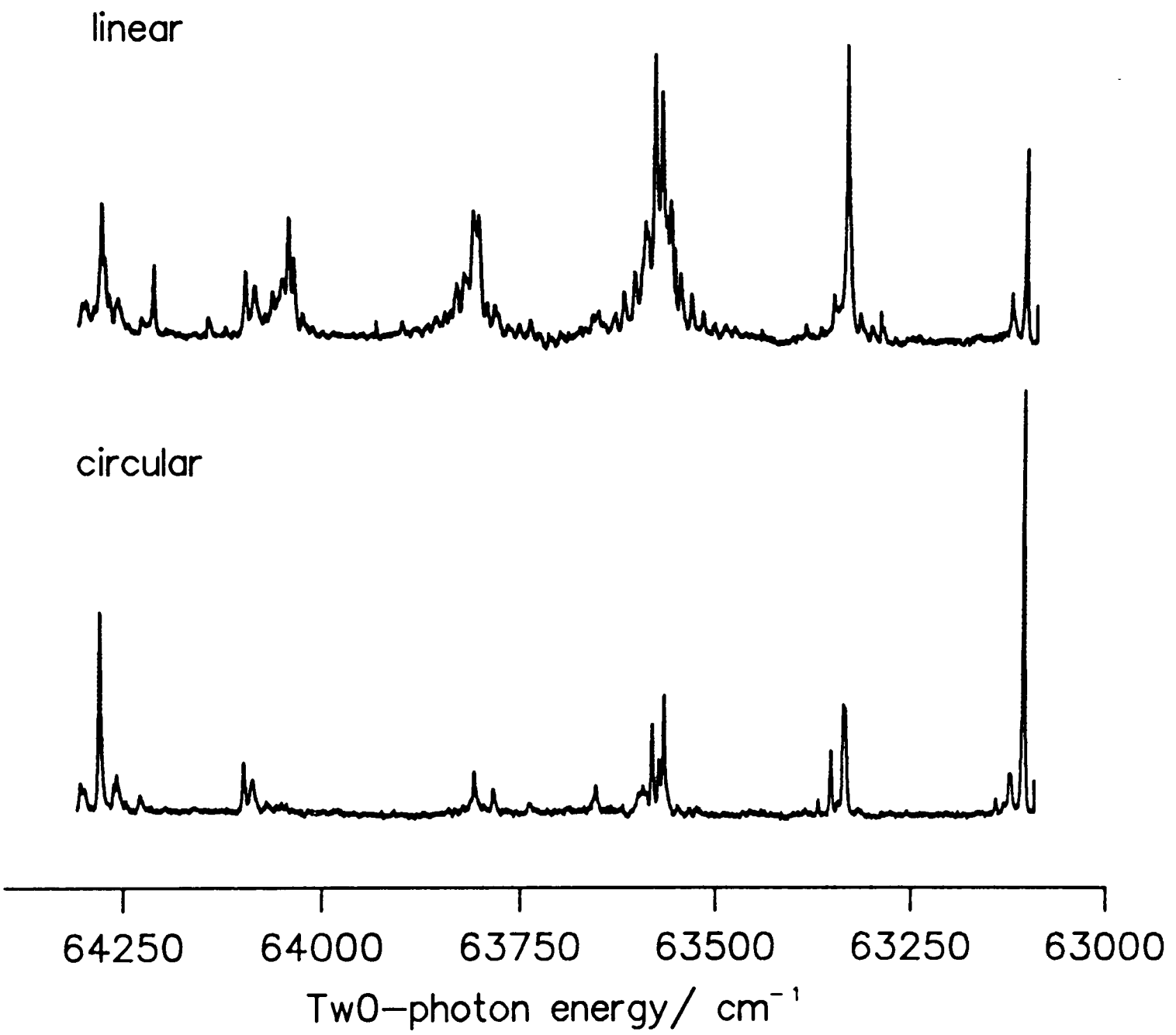

Figure 7–4: (2+1) REMPI spectrum of I_2, showing the effects of linear and circular polarised light on the 1_g component of the $[^2\Pi_{3/2}]_g$ 7s Rydberg state. The 1_g Rydberg state levels drop to almost zero intensity in circular polarisation.

7.6 References

(1) R.J. Donovan, R.V. Flood, K.P. Lawley, A.J. Yencha and T. Ridley, Chem. Phys., 164 (1992) 439.

(2) K.P. Lawley, T. Ridley, Z. Min, P.J. Wilson, M.S.N. Al-Kahali, R.J. Donovan, Chem. Phys., 197 (1995) 37.

(3) P.H. Bucksbaum, M. Bashkansky, R.R. Freeman, T.J. McIlraith, and L.F. Di DiMauro, Phys. Rev. Lett. 56 (1986) 2590.

(4) R. Hippler, H. Schwier, H.J. Hupert, and H.O. Lutz, Z. Phys. *D*5, (1987)21.

(5) M.C.R. Cockett, J.G. Goode, R.R.J. Maier, K.P. Lawley, and R.J. Donovan, J. Chem. Phys. 101 (1994) 126.

(6) R.G. Bray and R.M. Hochstrasser, Mol. Phys., 31 (1976) 1199.

APPENDIX A

Lectures Attended

In accordance with the regulations of the University of Edinburgh, Department of Chemistry, the following courses were attended during the last three years:

1. Structure and Bonding
2. Laser 1 & 2
3. Symmetry
4. Excited States & Ions
5. Reaction Dynamics
6. Molecular Spectroscopy & Quantum Theory
7. Laser Photochemistry and Spectroscopy
8. Advanced Spectroscopic and Dynamical Techniques
9. Unix 1
10. Latex
11. Fortran

Conferences and Meetings Attended

1. Joint Meeting with Laser Ionisation Studies Group, Dec 1993
2. Ames Symposium, April 1994
3. 5th Annual Northern Universities Meeting on Chemical Physics, July 1994
4. Aspects of Spectroscopy IV (Institute of Physics Spectroscopy Group), Sept 1994
5. RSC Endowed Lecture Sympsia, March 1995
6. Molecular Rydberg States: Spectroscopy, Properties and Theory, April 1995
7. The Royal Society of Chemistry Annual Chemical Congress, April 1995

In addition, all the laser group meetings and the departmental Physical Chemistry seminars were attended. Also, the joint meetings with the spectroscopy group at Heriot-Watt University were attended.

Publications

List of publications

(1) **Sequential two-photon excitation via repulsive intermediate states,** M.S.N Al-Kahali, R.J. Donovan, K.P. Lawley, T. Ridley, Chem. Phys. Lett. 220 (1994) 225.

(2) **Three-Photon Excitation of the Lower 0_u^+ Ion-Pair States of Cl_2 via a Continuum Intermediate State,** M.S.N Al-Kahali, R.J. Donovan, K.P. Lawley, T. Ridley, and A.J. Yarwood, J. Phys. Chem. 99 (1994) 525.

(3) **Vibronic coupling between Rydberg and ion-pair states of I_2 invetigated by (2+1) resonance enhanced multiphoton ionisation spectroscopy,** K.P. Lawley, T. Ridley, Z. Min, P.J. Wilson, M.S.N. Al-Kahali, R.J. Donovan, Chem. Phys. 197 (1995) 37.

(4) **Mass-resolved multiphoton ionisation spectroscopy of jet-cooled Cl_2. I. Bound-free-bound spectroscopy,** M.S.N Al-Kahali, R.J. Donovan, K.P. Lawley, Z. Min, and T. Ridley, J. Chem. Phys. 104 (1996) 1825.

(5) **Mass-resolved multiphoton ionisation spectroscopy of jet-cooled Cl_2. II. The (2+1) REMPI spectrum between 76000 and 90000 cm^{-1},** M.S.N Al-Kahali, R.J. Donovan, K.P. Lawley, and T. Ridley, J. Chem. Phys.104 (1996) 1833.

(6) **The REMPI Spectroscopy of Cl_2; a Bound-free-bound Route to the $1_g(^1D_2)$ Ion-pair State,** M.S.N Al-Kahali, R.J. Donovan, K.P. Lawley, Z. Min, and T. Ridley, Chem. Phys. *in press.*